

CORONAVIRUS

PI3K γ inhibition circumvents inflammation and vascular leak in SARS-CoV-2 and other infections

Ryan M. Shepard^{1†}, Anghesom Ghebremedhin^{1†}, Isaraphorn Pratumchai², Sally R. Robinson^{3,4}, Courtney Betts⁵, Jingjing Hu⁶, Roman Sasik⁷, Kathleen M. Fisch^{7,8}, Jaroslav Zak², Hui Chen¹, Marc Paradise¹, Jason Rivera¹, Mohammad Amjad¹, Satoshi Uchiyama⁹, Hideya Seo⁹, Alejandro D. Campos⁶, Denise Ann Dayao³, Saul Tzipori³, Cesar Piedra-Mora¹⁰, Soumita Das⁶, Farnaz Hasteh⁶, Hana Russo⁶, Xin Sun⁹, Le Xu⁹, Laura E. Crotty Alexander¹¹, Jason M. Duran¹¹, Mazen Odish¹¹, Victor Pretorius¹², Nell C. Kirchberger⁵, Shao-ming Chin¹, Tami Von Schalscha⁶, David Cheresch⁶, John D. Morrey¹³, Rossitza Alargova¹⁴, Brenda O'Connell¹⁴, Theodore A. Martinot¹⁴, Sandip P. Patel¹⁵, Victor Nizet^{9,16}, Amanda J. Martinot^{3,4,10}, Lisa M. Coussens^{5,17}, John R. Teijaro², Judith A. Varner^{1,6*}

Copyright © 2024 The Authors, some rights reserved; exclusive licensee American Association for the Advancement of Science. No claim to original U.S. Government Works

Virulent infectious agents such as severe acute respiratory syndrome coronavirus 2 (SARS-CoV-2) and methicillin-resistant *Staphylococcus aureus* (MRSA) induce tissue damage that recruits neutrophils, monocyte, and macrophages, leading to T cell exhaustion, fibrosis, vascular leak, epithelial cell depletion, and fatal organ damage. Neutrophils, monocytes, and macrophages recruited to pathogen-infected lungs, including SARS-CoV-2-infected lungs, express phosphatidylinositol 3-kinase gamma (PI3K γ), a signaling protein that coordinates both granulocyte and monocyte trafficking to diseased tissues and immune-suppressive, profibrotic transcription in myeloid cells. PI3K γ deletion and inhibition with the clinical PI3K γ inhibitor eganelisib promoted survival in models of infectious diseases, including SARS-CoV-2 and MRSA, by suppressing inflammation, vascular leak, organ damage, and cytokine storm. These results demonstrate essential roles for PI3K γ in inflammatory lung disease and support the potential use of PI3K γ inhibitors to suppress inflammation in severe infectious diseases.

INTRODUCTION

Severe acute respiratory syndrome coronavirus 2 (SARS-CoV-2), SARS-CoV, and Middle Eastern respiratory syndrome coronavirus (MERS-CoV) are viruses that cause lethal infections associated with aberrant pulmonary and systemic inflammation, vascular leak, coagulation, and organ damage (1). These and other viral and bacterial infections induce acute respiratory distress syndrome (ARDS), a disorder characterized by breakdown of lung capillary walls and epithelial integrity, leading to leakage of interstitial fluid, plasma proteins, and leukocytes into alveoli that can cause fatal organ damage (2).

Extensive recruitment of granulocytes, monocytes, and macrophages to the lung as a consequence of infection promotes organ damage and scarring as well as cytokine storm, a lethal systemic release of proinflammatory cytokines (2). In patients who survive ARDS, extensive lung fibrosis, compromised lung capacity, and systemic inflammation impair recovery from pulmonary and systemic viral infection (2). Single-cell sequencing has shown that SARS-CoV-2 infections induce loss of alveolar type I (ATI) and II (ATII) epithelial cells, vascular damage and inflammation, activation of fibroblasts, and coinfection with pneumonia-causing viruses (3–5). In children, SARS-CoV-2 infections generate a rapid interferon (IFN) response that ameliorates disease, whereas in adults, delayed IFN responses to MERS-CoV, SARS-CoV, and SARS-CoV-2 can fail to suppress viral infections and exacerbate the damage associated with severe inflammation (6, 7).

To identify therapeutic strategies that can reduce inflammatory damage induced by lethal infectious agents such as SARS-CoV-2, we compared immune responses to infections in lung and in bronchoalveolar lavage (BAL) specimens from humans, hamsters, and mice using multiplex immunohistochemistry (mIHC), fixed-tissue RNA sequencing, and spatial transcriptomics. These strategies together identified key roles for immature inflammatory neutrophils and monocyte/macrophages in mediating acute and chronic lung tissue damage during infections.

Research in our laboratory previously identified key roles for the phosphatidylinositol 3-kinase (PI3K) isoform, PI3K γ , in myeloid cell trafficking, immune-suppressive wound healing, and profibrotic macrophage polarization in cancer and chronic inflammatory diseases (8–14). We found here that PI3K γ plays a central role in lung damage in inflammatory diseases such as coronavirus disease 2019 (COVID-19), the respiratory disease caused by

¹Moore's Cancer Center, University of California, San Diego, La Jolla, CA 92093, USA.

²Department of Immunology, Scripps Research Institute, La Jolla, CA 92037, USA.

³Department of Infectious Disease and Global Health, Cummings School of Veterinary Medicine, Tufts University, North Grafton, MA 01536, USA. ⁴New England Regional Biosafety Laboratory, Cummings School of Veterinary Medicine, Tufts University, North Grafton, MA 01536, USA. ⁵Department of Cell, Developmental, and Cancer Biology, Oregon Health & Science University, Portland, OR 97201, USA.

⁶Department of Pathology, University of California, San Diego, La Jolla, CA 92093, USA.

⁷Center for Computational Biology and Bioinformatics, University of California, San Diego, La Jolla, CA 92093, USA.

⁸Department of Obstetrics, Gynecology & Reproductive Sciences, University of California, San Diego, La Jolla, CA 92093, USA.

⁹Department of Pediatrics, University of California, San Diego, La Jolla, CA 92093, USA.

¹⁰Department of Comparative Pathobiology, Section of Pathology, Tufts University Cummings School of Veterinary Medicine, North Grafton, MA 01536, USA.

¹¹Department of Medicine, University of California, San Diego, La Jolla, CA 92093, USA.

¹²Department of Surgery, University of California, San Diego, La Jolla, CA 92093, USA.

¹³Institute for Antiviral Research, Animal, Dairy, and Veterinary Science, Utah State University, Logan, UT 84322, USA.

¹⁴Infinity Pharmaceuticals, Cambridge, MA 02138, USA.

¹⁵Department of Medicine/Medical Oncology, University of California, San Diego, La Jolla, CA 92093, USA.

¹⁶Skaggs School of Pharmacy and Pharmaceutical Sciences, University of California, San Diego, La Jolla, CA 92093, USA.

¹⁷Knight Cancer Institute, Oregon Health & Science University, Portland, OR 97201, USA.

*Corresponding author. Email: jvarner@ucsd.edu

†These authors contributed equally to this work.

SARS-CoV-2 infections. Targeted inhibition of PI3K γ prevents myeloid cell trafficking, vascular leak, and damage to lung epithelium, providing therapeutic benefit in models of severe lung and systemic infection. These findings support the clinical evaluation of PI3K γ inhibitors for the treatment of infection-associated inflammation and disease progression.

RESULTS

CD163⁺ wound-healing macrophages predominate in severe COVID-19

To identify therapeutic strategies that could suppress the lethal inflammation associated with pulmonary disorders such as COVID-19, we compared immune responses in SARS-CoV-2 and other infections in humans, hamsters, and mice using patient lung tissue and animal models of disease. Under Institutional Review Board (IRB) approvals, we compared immune cell infiltrates in formalin-fixed, paraffin-embedded (FFPE) lung tissue from recently deceased patients with COVID-19 with normal human lung tissue obtained during lung surgeries at University of California, San Diego (UCSD), and BAL specimens from hospitalized, uninfected (normal), and SARS-CoV-2-infected patients (tables S1 to S4) using mIHC, RNA sequencing of FFPE tissue, and spatial transcriptomics. All BAL specimens were collected from hospitalized, living patients (tables S1 and S2), whereas lung tissues from COVID-19 patients were obtained from rapid autopsies of patients who died from SARS-CoV-2 infections early in the pandemic before vaccines or antiviral therapies were developed (table S4). The average interval between illness onset and death was 19.9 ± 13.1 days for patients with COVID-19 in this study. Patients who were virus positive at the time of death died 5 ± 2 days after illness onset, whereas virus-negative patients died at 28.5 ± 7 days after illness onset, suggesting that most patients died as a consequence of long-term, rather than acute, damage to the lung induced by the viral infection.

Lungs from SARS-CoV-2-infected patients exhibited congested blood vessels; enlarged interstitial septa; and alveoli congested with large mononuclear cells, red blood cells, and protein deposits in contrast with open airways with thin-walled interstitial septa separating alveoli and thin capillaries in normal lung tissue (Fig. 1A and fig. S1A). Sparsely distributed alveolar CD68⁺ macrophages in normal lungs were replaced by dense accumulations of CD68⁺ monocytes and macrophages (black arrows) filling alveolar, interstitial, and perivascular spaces in COVID-19 lungs (Fig. 1B and fig. S1A). Myeloperoxidase (MPO)⁺ neutrophils also were increased in COVID-19 lung tissue (Fig. 1C). Monocyte/macrophages and neutrophils were each significantly ($P = 0.0024$ and $P = 0.0023$, respectively) increased more than 10-fold and were more broadly dispersed in diseased versus normal lungs (Fig. 1, D and E); monocyte/macrophages were more abundant than neutrophils. Lungs from patients with COVID-19 also exhibited significantly ($P = 0.0028$) increased collagen deposition, identified as blue fibrils in Mason's trichrome-stained tissue (Fig. 1, F and G). This extensive macrophage and neutrophil infiltration as well as collagen deposition suggested that the lungs of most deceased patients with COVID-19 were undergoing macrophage-driven inflammation and fibrosis.

Hematoxylin and eosin (H&E) and IHC analysis of BAL specimens of hospitalized patients ($n = 3$) who were not infected

(normal) revealed the presence of large CD68⁺ alveolar macrophages yet few MPO⁺ cells. In contrast, BAL specimens from patients with COVID-19 ($n = 7$) were characterized by loss of alveolar macrophages and variable changes in MPO⁺ granulocytes (Fig. 1, H and I). We further analyzed BAL specimens of uninfected normal ($n = 4$) and hospitalized patients with COVID-19 ($n = 5$) (tables S1 and S2) by multiplex immune profiling (15) with validated panels of myeloid lineage-identifying antibodies (table S5) followed by quantitative analyses (fig. S1, B to D; see plots with red-labeled axes). BAL specimens from patients with COVID-19 exhibited a significantly ($P = 0.0317$) increased population of myeloid cells (Fig. 1J) that lacked CCR2 or CD66b expression (here named "myeloid-other") and are consistent with prior reports of extensive immature neutrophil and monocyte infiltration in BAL of patients with COVID-19 (4, 5).

We investigated biomarkers of immune cell functional states in lung tissues from uninfected patients and patients infected with SARS-CoV-2 with validated panels of lineage-identifying antibodies (table S6). Increased CD45⁺ (green), CD11b⁺ cells (red) (Fig. 1K, left and middle), and CD163⁺CD68⁺ macrophages (purple with blue membrane; Fig. 1K, right) were observed in pseudo-colored images of lungs from patients with COVID-19. No obvious changes in lymphoid cell (CD45⁺CD3⁺ or CD45⁺CD20⁺) density were noted (Fig. 1K), but lungs from patients with COVID-19 exhibited significantly ($P = 0.0324$) decreased pan-cytokeratin-positive epithelial cells (Fig. 1L) (16). Immature monocytes and neutrophils (myeloid-other, $P = 0.0206$) as well as natural killer cells, $\gamma\delta$ T cells, plasma cells, and other cells ($P = 0.0324$) were increased in COVID-19 lungs (Fig. 1M), as previously reported (2–6, 17–19). CD68⁺ macrophages were positive for CD163 (Fig. 1N), a biomarker expressed by immune-suppressive, wound-healing-type macrophages (17, 18).

Three patients with COVID-19 who died within 7 days of hospitalization were virus-positive at the time of death (table S4). In their tissues, surfactant protein B-positive (SPB⁺) ATII cells were decreased, whereas programmed cell death protein ligand 1 (PD-L1)⁺ and Ki67⁺SPB⁺ cells were increased (fig. S2, A to C), consistent with ongoing lung tissue repair processes. Active viral infection was associated with increased immature myeloid cells (myeloid-other), CD163⁺CD68⁺ macrophages (fig. S2, D and E), as well as increased PD-L1 on dendritic cells and granulocytes (fig. S2, F and G).

Although total T cell abundance was unchanged, CD4⁺ T cells, particularly Foxp3⁺Tbet⁺CD4⁺Th2 cells, were significantly ($P = 0.0206$) increased in lungs of patients with COVID-19 (Fig. 1O). T helper 2 (T_H2) subsets have known roles in resolution of viral infection, wound-healing, and fibrosis; are often associated with CD163⁺ macrophages; and are increased in patients with COVID-19 (19). Increased expression of programmed cell death protein 1 (PD-1), but not Ki67 (Fig. 1P and fig. S2, H and I), suggests the presence of exhausted T cells in the lungs of patients with COVID-19 (20, 21). Although high PD-1 and EOMES expression together can signify T cell activation, no increases in the CD8⁺PD-1⁺EOMES⁺ cells were observed (Fig. 1Q), suggesting an absence of activated CD8⁺ T cells in COVID-19 lungs. Expression of PD-L1 and PD-1 was also noted on CD20⁺ B cells in virus-positive COVID-19 lungs (fig. S2, J and K) (21). Together, these results suggest a dysregulated immune microenvironment characterized by infiltration of immature granulocytes and monocytes, CD163⁺ wound healing-type macrophages, exhausted T cells, and fibrosis in lungs of patients with lethal COVID-19 disease.

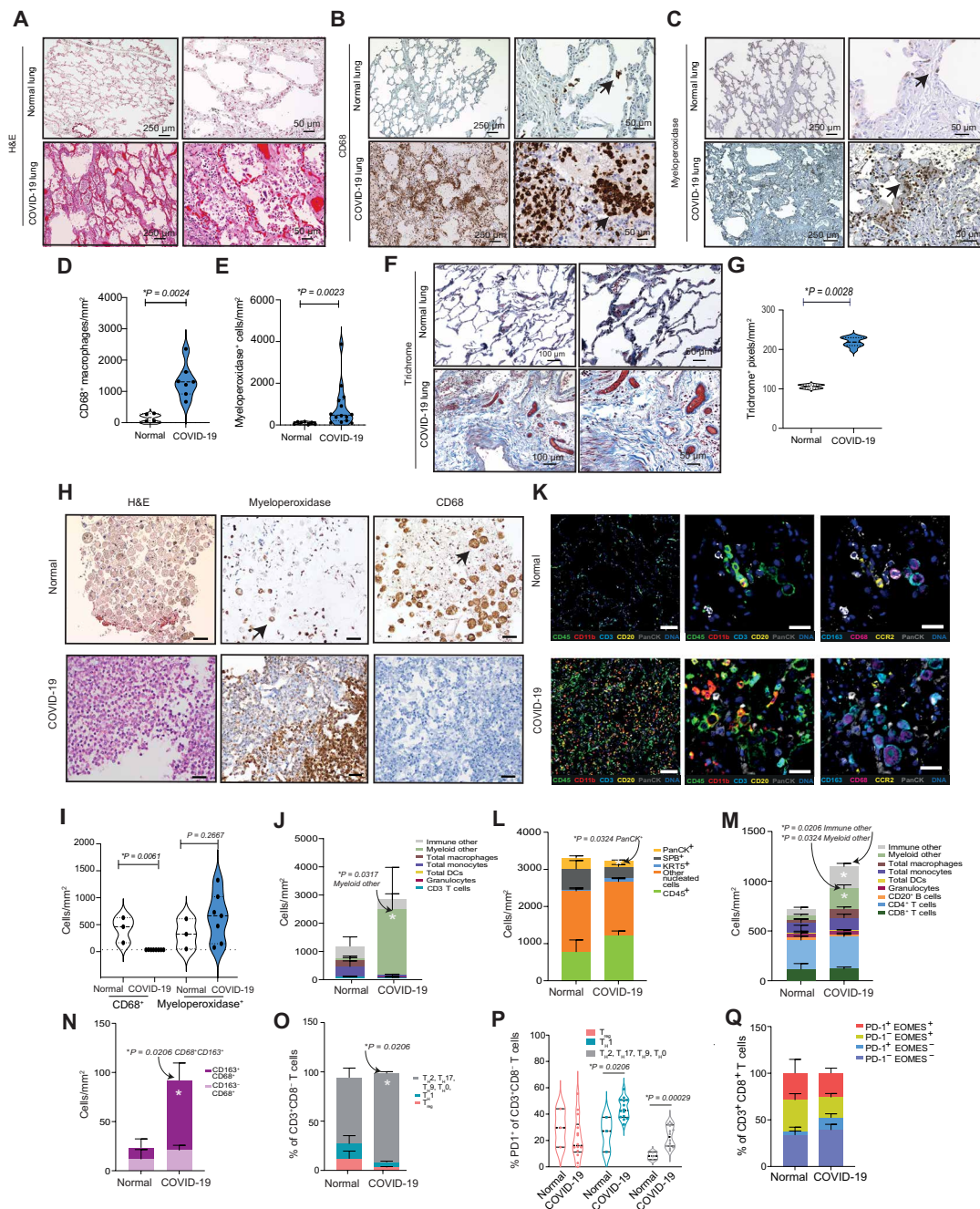


Fig. 1. CD163⁺ myeloid cells dominate the immune microenvironment of SARS-CoV-2-infected lungs. (A to C) H&E (A), anti-CD68 (B), and anti-myeloperoxidase (MPO) (C) stained images of lung tissue from patients who were uninfected (normal) or infected with SARS-CoV-2 (COVID-19); scale bar, 250 or 50 μm ; arrows indicate CD68⁺ macrophages or MPO⁺ granulocytes. (D and E) Graphs of CD68⁺ macrophages/mm² (D) and MPO⁺ granulocytes/mm² (E) in normal ($n = 5$) and COVID-19 patient lung tissues ($n = 14$). (F) Images of trichrome-stained lung tissue from normal patients and patients with COVID-19. Scale bars, 100 or 50 μm . (G) Graphs of trichrome⁺ pixels/mm² in lung tissue from normal patients ($n = 6$) and patients with COVID-19 ($n = 8$). (H) Images of H&E, anti-CD68, and anti-MPO-stained sections of cell pellets from BAL from uninfected patients and patients infected with COVID-19. Arrows indicate granulocytes and macrophages. (I) Graphs of CD68⁺ macrophages/mm² and MPO⁺ granulocytes/mm² in sections of BAL cells from normal patients ($n = 3$) and patients with COVID-19 ($n = 7$). (J) Graphs of immune cell proportions within BAL from patients with COVID-19 ($n = 5$) and uninfected normal patients ($n = 4$). (K, left) Pseudo-colored images of mlHC-stained lung tissue from patients with COVID-19 and normal uninfected patients: total immune cells (CD45, green), myeloid cells (CD11b, red), total T cells (CD3, cyan), total CD20⁺ B cells (CD20, yellow), epithelium (PanCK, white), and DNA (blue). (K, middle) Higher magnification of a subregion from the left column. (K, right) Pseudo-colored images for CD68 (magenta); CCR2 (yellow), CD163 (cyan), and PanCK (white). (L to Q) Quantification graphs of multiplex immune markers in lung tissue from patients with COVID-19 ($n = 14$) and normal ($n = 3$) patients: (L) PanCK epithelial and immune cells, (M) CD45⁺ cell subsets, (N) CD163⁺ macrophages, (O) CD3⁺ CD8⁻ cell subsets, (P) CD3⁺ CD8⁻ cells expressing PD-1, and (Q) CD3⁺ CD8⁺ cells expressing PD-1 or EOMES. For violin plots, dashed lines indicate mean and interquartile range; for stacked bar and single bar graphs, bars indicate means \pm SEM. For statistical testing, t tests (D and G) or Mann-Whitney nonparametric tests [(E), (I), (J), and (L) to (Q)] were used.

Early inflammation is followed by wound-healing signatures in COVID-19 lungs

To extend our understanding of the immune microenvironment in airways of patients with COVID-19, we performed RNA sequencing of normal and SARS-CoV-2-infected FFPE BAL and lung tissue. For bulk RNA sequencing, we used a low-input ligation-based targeted whole transcriptome expression profiling assay, TempO-Seq, to characterize gene expression signatures in FFPE tissue (22, 23). Transcriptome analysis of BAL specimens (normal, $n = 5$; COVID-19, $n = 8$) revealed that COVID-19 BAL was primarily characterized by increased expression of genes associated with immature neutrophil recruitment (*CCL3*, *CXCL1*, *CXCL2*, *CXCL8*, *S100A8*, *SELL*, and *CSF3R*), proinflammatory response pathways (*CXCL8/IL8*, *CCL3*, *CCL4*, *IL1B*, *S100A9*, *S100A8*, and *OSM*), and mRNA editing (*APOBEC3A*) but also decreased major histocompatibility complex class II (*HLA-DMB* and *HLA-DRA*) (Fig. 2, A and B). COVID-19 BAL transcriptomes exhibited similarity to inflammatory and infectious disease responses (Fig. 2C and fig. S3A). Together, these data indicate a florid myeloid immune response in COVID-19 lungs.

We performed RNA sequencing of FFPE lung tissue specimens from 5 normal and 12 SARS-CoV-2-infected lung tissues. Specimens from upper and lower lung of two patients each were also sequenced. Transcriptome analysis indicated that lungs from patients with COVID-19 exhibited more than 2500 significantly [adjusted P value (P_{adj}) < 0.05] down-regulated genes and 813 significantly ($P_{\text{adj}} < 0.05$) up-regulated genes compared with lungs from uninfected, normal patients (Fig. 2, D and E). Volcano plot (Fig. 2D) and heatmaps of differentially expressed genes, as well as gene set enrichment analysis (GSEA) (Fig. 2, E and F) demonstrate up-regulated genes associated with tissue remodeling/fibrosis (e.g., *TIMP1*, *TGFB*, *COL1A1*, *COL3A1*, *COL5A1*, *LOX*, *MMP14*, and *TGFB3*) but decreased neutrophil recruitment genes (e.g., *IL1A*, *CXCL2*, *CXCL1*, *CCL8*, and *CSF3R*) and lung epithelial function (e.g., *CFTR*, *SFTPB*, *SFTPC*, and *MUC15*) in lungs from patients with COVID-19. GSEA also indicated up-regulated genes associated with glycolysis, the unfolded protein response, epithelial to mesenchymal transition, coagulation, the G₂-M checkpoint, cellular response to stress, and neutrophil extracellular trap formation (Fig. 2F and fig. S3, B to E). Lung tissue from patients with COVID-19 was associated with down-regulated genes in proinflammatory and cholesterol homeostasis pathways, among others. BAL from patients with COVID-19 was more proinflammatory and neutrophilic than lung tissue, whereas lung tissue was characterized by more monocyte/macrophages and an overall epithelial-to-mesenchymal transition/fibrosis signature. Diseased lungs exhibited significantly increased gene expression of *CD163* ($P = 0.0006$) and *C1R* ($P = 0.0003$), indicating the presence of wound-healing, immune-suppressive-type macrophages. Significant loss of genes associated with normal airway functions, including surfactant proteins (*SFTPB*, $P = 0.0136$; *SFTPC*, $P = 0.0003$) (Fig. 2G and fig. S3F), was observed in diseased lungs, supporting prior descriptions that COVID-19 is associated with the influx of wound-healing macrophages and loss of ATII cells (2–5). These results are consistent with the presence of a neutrophil-rich lung environment in the early stages of disease that is replaced by a macrophage-rich environment and associated fibrosis and progressive COVID-19.

To correlate RNA sequencing and IHC analyses, we applied cell type deconvolution analysis to normalized expression values in BAL and lungs from normal patients and patients with COVID-19 (Fig. 2,

H and I) (24, 25). This analysis confirmed that normal BAL exhibits a high macrophage/low neutrophil signature, whereas COVID-19 BAL exhibits a high neutrophil/low macrophage signature, similar to results from our IHC studies (Fig. 2H). Cell type deconvolution of bulk RNA sequencing data revealed increased monocytes, macrophages, fibroblasts, mesothelial cells, and goblet cells and decreased ATII cells in lungs from patients with COVID-19 versus normal patients (Fig. 2I). An increase in goblet cells has been previously associated with chronic obstructive pulmonary disease, a chronic fibrotic disorder (26). These results reveal that lethal COVID-19 is characterized by ATII cell depletion and a monocyte/macrophage/fibroblast-rich, wound-healing, immune-suppressive environment, suggesting impaired lung function as previously shown (27).

We examined the impact of ongoing viral infection at the time of death on gene expression profiles. Tissues of virus-positive patients exhibited signatures of IFN- α and IFN- γ pathways, illustrated by expression of IFN-inducible genes, such as *CXCL10*, *CXCL11*, *CCL8*, and *OAS3* (fig. S4, A to C). In contrast, virus-negative COVID-19 patient tissues exhibited higher signatures of transforming growth factor- β (TGF- β) signaling and coagulation (fig. S4C). Virus-positive patients exhibited signatures of cellular stress, cytokine expression, inflammation, and loss of normal cellular physiology when compared with lungs of normal, uninfected patients (fig. S4D). Two virus-positive patients at the time of death were in treatment for multiple myeloma, a known risk factor for lethal COVID-19 due to the absence of antibody-mediated immune responses in these patients (28). Because virus-positive patients died from COVID-19 an average of 5 days after illness onset but virus-negative patients died 28.5 days after illness onset, these data support that death from COVID-19 is associated with either an early insurmountable viral infection or long-term wound-healing/fibrosis processes that damage normal lung function and architecture.

Macrophages in COVID-19 lungs express a wound-healing gene expression signature

Our studies indicate that increased macrophage content in COVID-19 lungs correlates with fibrosis and death. To explore whether lung myeloid cells promote the wound-healing, profibrotic environment in COVID-19-diseased lungs, we performed spatial profiling of lung tissue using the nanoString GeoMx ImmuneOncology plus COVID-19 platform on *CD68*⁺ macrophages, *MPO*⁺ granulocytes, and *panCK*⁺ epithelium in normal and COVID-19 lung tissue specimens. Volcano plots, heatmaps, and GSEA of differentially expressed genes within macrophages demonstrate that COVID-19 lung macrophages exhibit alternatively activated, wound-healing, immune-suppressive gene expression signatures characterized by increased expression of *CD163*, *IDO*, heat shock proteins (*HSPA1A*), complement/coagulation (*C1QA*, *C1QB*, and *C1R*), and tissue remodeling (*COL3A1*, *COL1A1*, *COL1A2*, *FNI*, and *CTSS*) pathways, with down-regulation of genes in immune response pathways (*HLA-DRB5*) (fig. S5, A to C). Macrophages in virus-positive tissues expressed IFN-associated genes, including *IRF8*, *OAS1*, *OAS2*, and *CXCL8* (fig. S5, A to C). Spatial profiling of granulocytes revealed IFN, oxidative phosphorylation, apoptosis, and complement expression signatures in patients with COVID-19 (fig. S5, D to F). Lung epithelial cells also expressed signatures of inflammation and TGF- β signaling (fig. S5, G to I). These signatures support the hypothesis that during SARS-CoV-2 infection, myeloid cells initially mount an IFN-driven antiviral response that is superseded by wound-healing

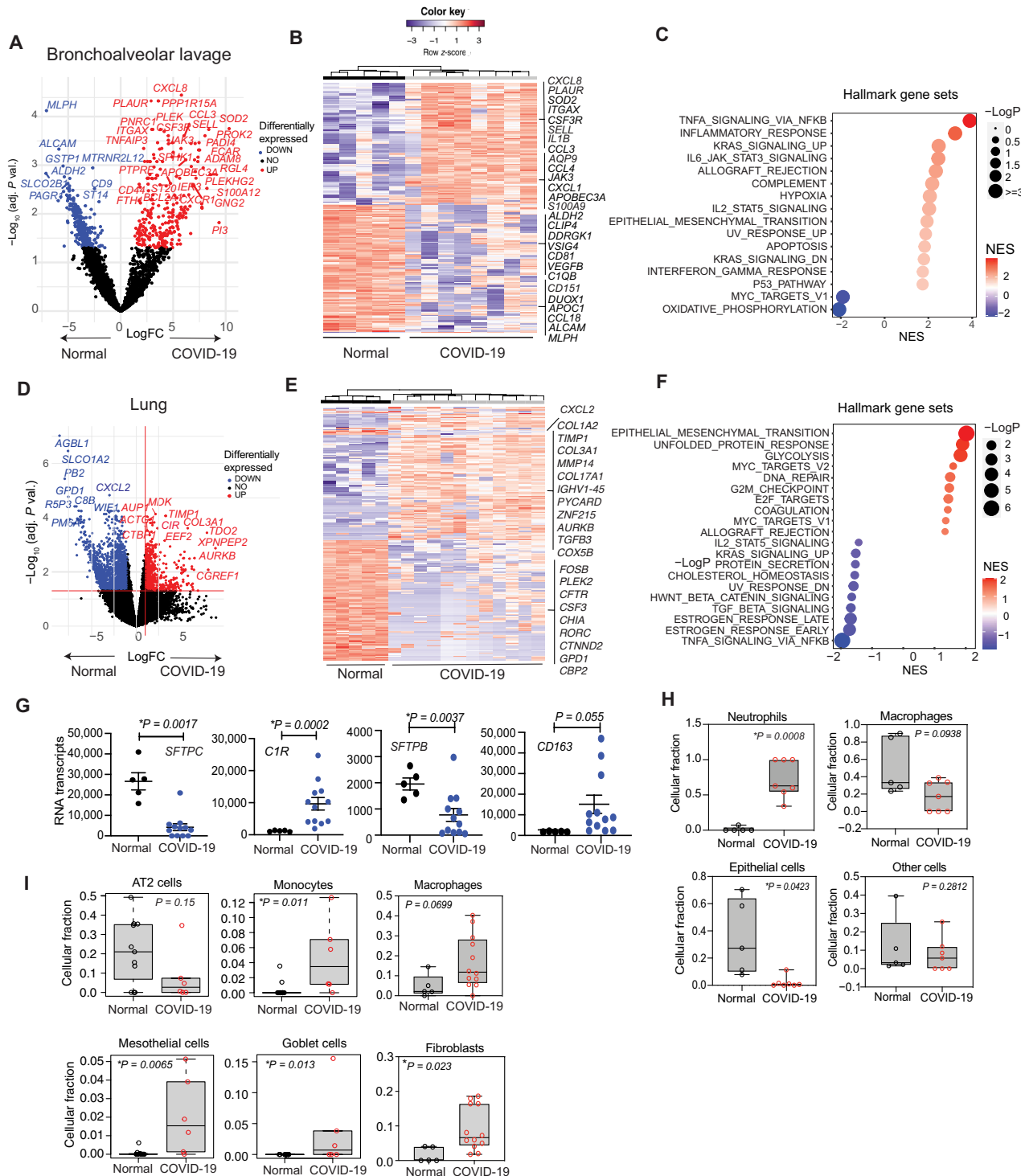


Fig. 2. Transcriptomics identify a myeloid cell-rich microenvironment in SARS-CoV-2-infected lung tissue. (A) Volcano plot of differential mRNA expression in BAL cells from uninfected “normal” patients ($n = 5$) and patients infected with COVID-19 ($n = 8$). Significant gene expression differences are identified in blue (down-regulated in COVID-19) or red (up-regulated in COVID-19). (B) Heatmap depicting differentially expressed genes in BAL cells from normal uninfected ($n = 5$) and infected patients ($n = 8$). (C) Plot of up- or down-regulated Hallmark pathways in BAL from infected ($n = 8$) versus uninfected patients ($n = 5$) graphed according to normalized expression score (NES) and $\log P_{adj}$. (D) Volcano plot of differential mRNA expression in lung tissue from normal patients ($n = 5$) and patients with COVID-19 ($n = 12$). (E) Heatmap depicting differentially expressed genes in lung tissue from normal patients ($n = 5$) and patients with COVID-19 ($n = 12$). (F) Plot of differentially expressed hallmark pathways in lung tissue from normal patients and patients with COVID-19 graphed according to NES and $\log P_{adj}$. (G) Graphs of *SFTPC*, *C1R*, *SFTPB*, and *CD163* transcripts in COVID-19 ($n = 12$) versus normal ($n = 5$) patient lung tissue (means \pm SEM), (H and I) Box plots of means \pm SEM cell type deconvolution of (H) BAL from normal patients ($n = 5$) and patients with COVID-19 ($n = 8$) and (I) lung tissue from normal patients ($n = 5$) and patients with COVID-19 ($n = 12$). P values were determined by limma-voom.

responses associated with fibrosis and death, much as has been observed after infection with SARS-CoV-1 and MERS-CoV and in animal models of betacoronavirus infections (6).

PI3K γ promotes inflammation in models of SARS-CoV-2 infection

These results suggest that strategies that inhibit myeloid cell recruitment to tissues could provide therapeutic benefit in COVID-19 and other severe infectious diseases. One potential target for therapeutic intervention of myeloid cell trafficking in inflammatory diseases is the signaling protein PI3K γ . PI3K γ promotes neutrophil and monocyte trafficking to tumors by activating integrin $\alpha 4\beta 1$ expressed on circulating myeloid cells (8); PI3K γ also promotes immune-suppressive, profibrotic transcription in macrophages (9–11). Genetic or pharmacological blockade of PI3K γ suppressed recruitment of myeloid cells to tumor tissues, repolarized macrophages and dendritic cells to promote antitumor T cell responses, and prevented fibrosis (9–11). Other studies showed that PI3K γ inhibition also blocked neutrophil recruitment and degranulation (12) and prevented vascular leak (29, 30). Inhibition of PI3K γ also suppressed fibrosis in association with pancreatic cancer and pancreatitis through the reduction of macrophage expression of profibrotic factors, including *TGF β* , *PDGFA*, *PDGFB*, *PLAU*, and extracellular matrix genes (10).

To investigate whether PI3K γ inhibition might also ameliorate lung damage associated with SARS-CoV-2 and other infections, we first evaluated PI3K γ expression in lung tissue from normal patients and patients with COVID-19. *PIK3CG* mRNA was expressed both in COVID-19 patient lung tissue and in normal lung (Fig. 3A). IHC staining for PI3K γ and CD68 in serial sections of COVID-19 tissue revealed that PI3K γ expression overlapped extensively with CD68⁺ macrophages (Fig. 3B). Fluorescent confocal microscopy of COVID-19 lungs for CD68 (green) and PI3K γ (red) expression showed considerable overlap of expression (yellow, arrows) (Fig. 3C, top). Stochastic optical reconstruction microscopy of single macrophages demonstrated that PI3K γ colocalizes extensively with CD68 in clusters at the cell membrane in COVID-19-infected lungs (Fig. 3C, bottom). Increased macrophage content and macrophage PI3K γ expression was also observed in lung tissue from patients with other inflammatory lung disorders (fig. S6, A and B). Specificity of the antibody for PI3K γ used in IHC studies was confirmed by the manufacturer's specifications and Western blotting of immortalized wild-type (WT), mock-transfected, and PI3K γ CRISPR-mediated knockout murine macrophages (fig. S6C).

We next evaluated PI3K γ expression in an animal model of SARS-CoV-2 infection (31). SARS-CoV-2 induces nonlethal respiratory disease in hamsters, with a duration of 10 to 14 days. When Syrian golden hamsters were infected intranasally with SARS-CoV-2, infiltration of MPO⁺ neutrophil and IBA1⁺ macrophages into lungs was rapidly induced. Neutrophil infiltration peaked at 4 days after infection, whereas IBA1⁺ macrophage infiltration peaked 7 days after infection (Fig. 3, D and E). SARS-CoV-2 infection of Syrian golden hamsters increased PI3K γ mRNA expression in these cells, as detected by RNAscope fluorescence microscopy (Fig. 3, D and E). Together, these data indicate that PI3K γ is expressed in COVID-19-associated myeloid cells. On the basis of its roles in myeloid cell trafficking in cancer and its tissue-specific expression patterns, it is possible that PI3K γ plays a key role in promoting COVID-19.

To investigate whether PI3K γ inhibition could serve as a therapeutic strategy for COVID-19, we tested the PI3K γ inhibitor IPI-549

(eganelisib), a highly selective PI3K γ inhibitor that is currently in development as a cancer therapeutic and has shown safety and activity in clinical trials (13, 14) in a hamster model of SARS-CoV-2 infection (Fig. 3F) (31). Hamsters were inoculated with SARS-CoV-2 and treated with a 4-day course of IPI-549 or vehicle from day 0 to day 4 (Fig. 3F). Neutrophil accumulation was substantially suppressed by IPI-549 treatment, whereas macrophage accumulation was not inhibited, possibly because macrophage accumulation peaks at day 7 after inoculation (Fig. 3, G to I); treatment did not substantially affect weight loss in this nonlethal model of SARS-CoV-2 infection (fig. S7A). These results indicate that PI3K γ inhibition can suppress neutrophil recruitment induced by SARS-CoV-2 infection and suggest that continuous treatment with IPI-549 might be warranted to further protect lungs from inflammation associated with infection.

We then tested the effect of PI3K γ inhibition in murine models of SARS-CoV-2 infection. K18-ACE2TG C57BL/6 mice (32) were infected with SARS-CoV-2 and treated 2 days later with IPI-549 or vehicle (Fig. 3J). IPI-549 treatment of SARS-CoV-2-infected hACE2-TG mice significantly delayed weight loss (Fig. 3K, $P = 0.02472$) and delayed signs of illness, including reduced activity, reduced appetite, and social withdrawal, but did not significantly affect viral load ($P = 0.0712$) or survival (Fig. 3L and fig. S7B). IPI-549 treatment significantly reduced monocyte/macrophage ($P = 0.0108$) and granulocyte ($P = 0.0172$) infiltration, as detected by IHC (Fig. 3, M to O) or by flow cytometry in lung tissue collected at 5 days postinfection (dpi) (fig. S7, C to E).

Transcriptomics reveal that PI3K γ inhibition reduces inflammation in mice infected with SARS-CoV-2

To investigate the impact of PI3K γ inhibition on SARS-CoV-2-infected mouse lungs further, we performed RNA sequencing of lungs from hACE2Tg mice infected intranasally with SARS-CoV-2 and treated 2 to 5 dpi later with vehicle or IPI-549, as shown in Fig. 3J. Differential expression analysis revealed that just 3 days of IPI-549 treatment down-regulated expression of proinflammatory cytokines and transcription factors (e.g., *Irf8*, *Irf5*, *Tlr9*, *Tnfa*, *Osm*, *S100a4*, and *Ltf*); neutrophil, monocyte, and macrophage markers (*Adgre1*, *Cd68*, *Trem2*, *Itgam*, *ApoE*, *C1qa*, and *Ly6c2*); and markers of fibrosis (*Col1a1*, *Col3a1*, *Col5a2*, *Fn1*, *Mmp2*, and *Mmp8*) (Fig. 4A). In contrast, genes associated with normal organ development (e.g., *Tgfb3*) or protection from oxidative stress (e.g., *Cbr2* and *Ahr*) were up-regulated in IPI-549-treated lungs (Fig. 4A). Signatures of macrophage activation, response to infection, inflammation, and IFN- γ signaling stimulated by SARS-CoV-2 infection were down-regulated in IPI-549-treated lungs, and signatures of epithelial and vascular development were up-regulated in IPI-549-treated lungs (Fig. 4B). To determine whether differences between experimental conditions were associated with unique cell-type signatures, we assessed the list of differentially expressed genes for enrichment for gene expression markers used to define cell types, as defined in PanglaoDB (33), a single-cell sequencing resource for gene expression data collected and integrated from multiple studies. Vehicle-treated, SARS-CoV-2-infected lungs exhibited gene expression signatures of macrophage, monocyte, and myeloid-derived suppressor cells, whereas IPI-549-treated lungs exhibited signatures of lung epithelial cells, including Clara cells, ATI and ATII cells, and ionocytes (Fig. 4C). Examples of down-regulated macrophage genes in IPI-549-treated lungs shown in the heatmap in fig. S8 and in graphs of transcripts per million for monocyte/macrophages genes include *Adgre1*, *Itgam*, *Cd68*, and

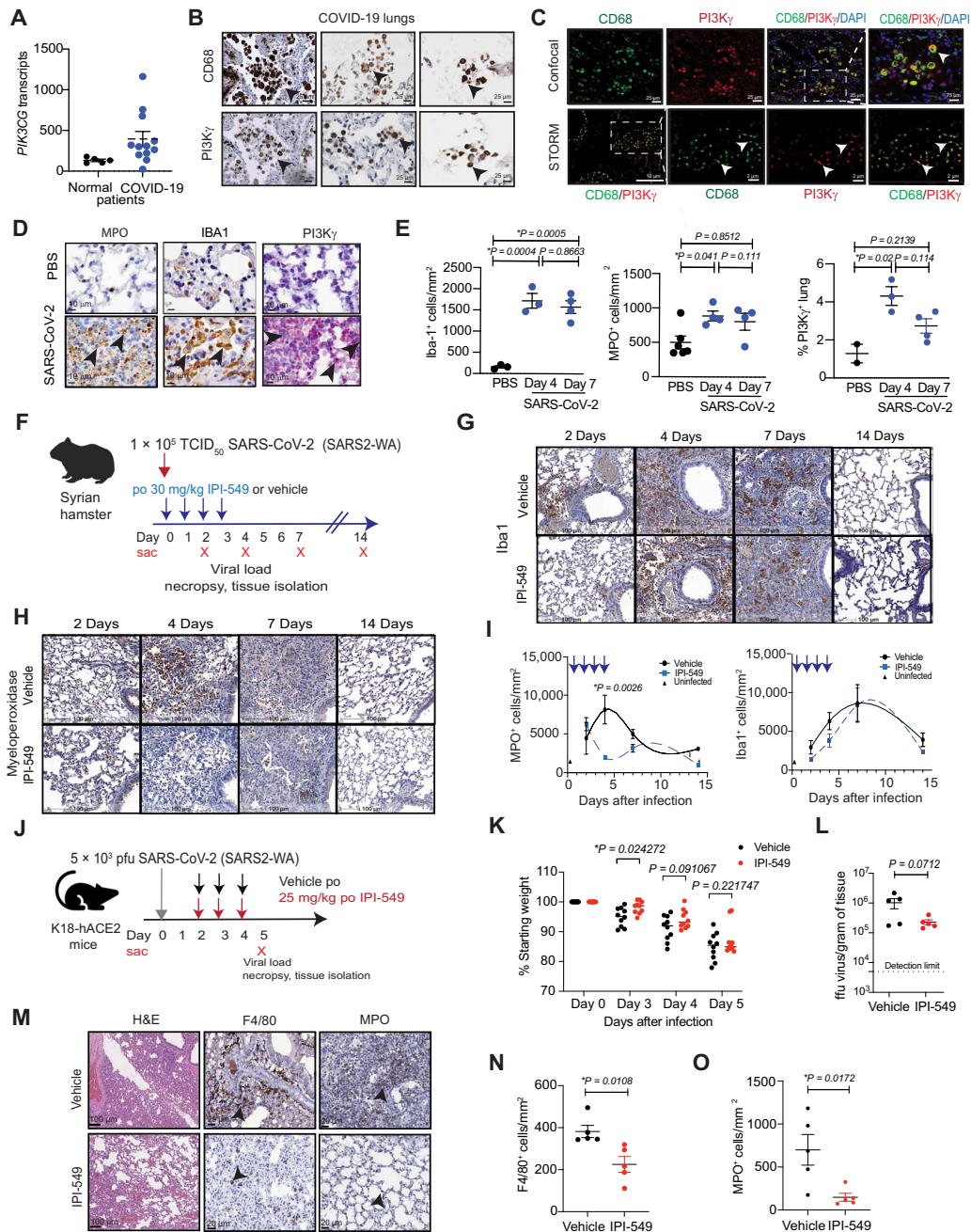


Fig. 3. PI3K γ promotes inflammation in response to SARS-CoV-2 infection. (A) Graph of *PIK3CG* gene transcripts determined by RNA sequencing of FFPE lung tissue from normal patients ($n = 5$) and patients with COVID-19 ($n = 14$). (B) Images of CD68 and PI3K γ expression in lung tissue from patients with COVID-19. Scale bar, 25 μm . Arrowheads indicate CD68 $^{+}$ and PI3K γ^{+} cells in serial 5- μm sections. (C) PI3K γ (red), CD68 (green), and DAPI (blue) confocal (top) and stochastic optical reconstruction microscopy (STORM, bottom) images of macrophages in COVID-19-infected lungs. Scale bars, 25 or 75 μm (top) and 2 or 10 μm (bottom). Insets indicate fields magnified in subsequent panels. Arrowheads identify CD68 $^{+}$ PI3K γ^{+} -stained cells. (D) Immunostaining for MPO $^{+}$ granulocytes, IBA1 $^{+}$ macrophages, and RNAScope detection of PI3K γ mRNA in lung tissue from uninfected [phosphate-buffered saline (PBS)] and SARS-CoV-2-infected Syrian golden hamsters. Scale bar, 10 μm . Arrowheads identify stained cells. (E) Graphs of means \pm SEM IBA1 $^{+}$ macrophages, MPO $^{+}$ granulocytes, and PI3K γ mRNA $^{+}$ cells in lung tissue from uninfected (PBS, $n = 2$ to 5) and SARS-CoV-2-infected (COVID, $n = 3$ or 4) hamsters. (F) Schematic of hamster infection with SARS-CoV-2 and treatment with vehicle ($n = 4$) or IPI-549 ($n = 4$). (G and H) Images of IBA1 $^{+}$ macrophages (G) and MPO $^{+}$ granulocytes (H) in lungs from (F). (I) Graphs of means \pm SEM MPO $^{+}$ neutrophils and IBA1 $^{+}$ macrophages in hamster lungs over time. Arrows indicate days of treatment. (J) Schematic of K18-ACE2 transgenic mice infected with SARS-CoV-2 and treated with vehicle or IPI-549. (K) Graph of median weight loss over time for mice infected with SARS-CoV-2 and treated with vehicle ($n = 10$) or IPI-549 ($n = 10$). (L) Graph of mean \pm SEM viral load expressed as focus-forming units (ffu)/g of lung tissue in mice ($n = 10$ per group) from (J). (M) Images of H&E, MPO $^{+}$, and F4/80 $^{+}$ staining in end point tissues from (J). Scale bar, 20 μm . Arrowheads indicate F4/80 $^{+}$ macrophages and MPO $^{+}$ granulocytes. (N and O) Graphs of means \pm SEM F4/80 $^{+}$ macrophages/mm 2 (N) and MPO $^{+}$ granulocytes/mm 2 (O) in lung tissue from mice infected with SARS-CoV-2 and treated with vehicle ($n = 5$) or IPI-549 ($n = 5$). Statistical analysis was performed by limma-vroom (A), unpaired t tests [(K), (L), (N), and (O)], or one-way ANOVA with Tukey's post hoc multiple comparisons test (E and I).

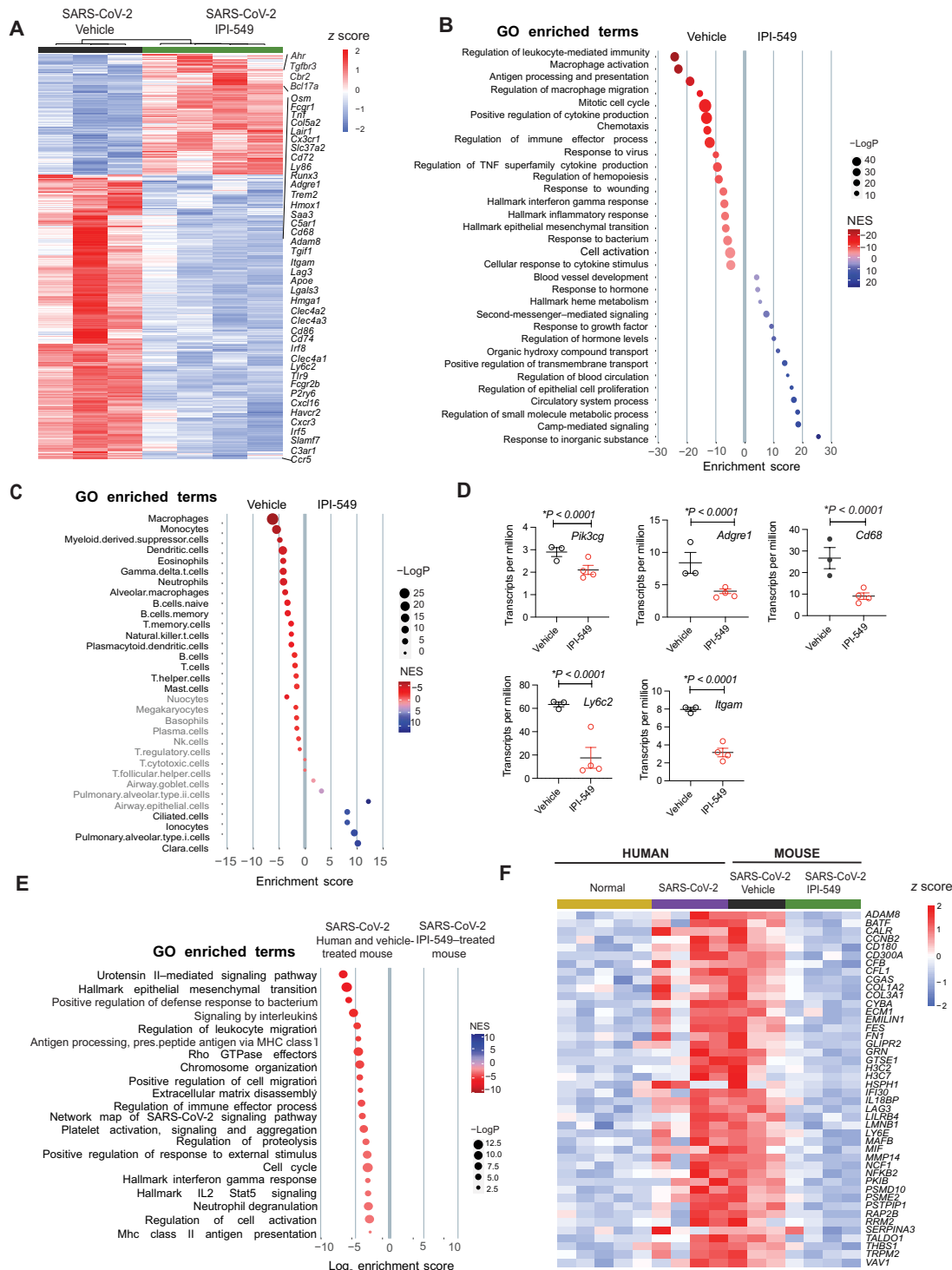


Fig. 4. PI3K γ inhibition suppresses gene expression signatures of inflammation and tissue damage during SARS-CoV-2 infection. (A and B) Heatmap (A) and gene set enrichment signatures (B) of differentially expressed genes and pathways in SARS-CoV-2-infected, vehicle-treated, or IPI-549-treated mouse lungs at day 5 after infection. Select gene names are shown. (C) Cell type enrichment signatures expressed in lungs from (A). Cell types shown in gray were not significantly changed in lungs from IPI-549-treated animals. (D) Transcripts per million of myeloid cell genes *Pik3cg*, *Adgre1*, *Cd68*, *Ly6c2*, and *Itgam* are shown for lungs from (A). (E) Gene enrichment signatures common to mouse and human SARS-CoV-2-infected lungs that were down-regulated in IPI-549-treated lungs. (F) Heatmap of differentially expressed genes that were up-regulated in SARS-CoV-2-infected, IPI-549-treated mouse lungs versus SARS-CoV-2-infected human and mouse lung tissues. Statistical analysis was performed by limma-voom.

Ly6c2 (Fig. 4D). *Pik3cg*, the gene for PI3K γ , was also down-regulated upon IPI-549 treatment, indicating a reduction in myeloid cell content. We identified 102 genes that were up-regulated in both SARS-CoV-2-infected murine and human lungs but were down-regulated in IPI-549-treated lungs (Fig. 4, E and F). These genes were associated with signatures of inflammation, neutrophil degranulation, leukocyte migration, SARS-CoV-2 signaling, extracellular matrix disassembly, and IFN- γ responses (Fig. 4E). Select genes that were up-regulated in SARS-CoV-2-infected human and mouse lungs and down-regulated in IPI-549-treated lungs, including IFN response genes (*CGAS* and *IFIT130*), fibrosis-associated genes (*COL1A2*, *COL3A1*, and *FNI*), and immune exhaustion genes (*LAG3* and *LILRB4*), are shown in Fig. 4F. Together, these data indicate that IPI-549 treatment prevents epithelial tissue damage and fibrosis.

PI3K γ inhibition reduces inflammation and tissue damage in aged mice infected with SARS-CoV-2

We next examined the effect of PI3K γ inhibition on mouse-adapted (ma)SARS-CoV-2 infection in aged mice in three separate cohorts. Ten-month-old female BALB/c mice were infected intranasally with maSARS-CoV-2 (34) and were treated with vehicle ($n = 5$) or with IPI-549 ($n = 10$) from 0 dpi until 2 dpi (cohort 1) (Fig. 5A). Tissue and blood were collected from cohort 1 mice on day 2 after infection for viral load, histological, and other assessments. Additional cohorts of mice were infected and treated with vehicle ($n = 5$) or IPI-549 ($n = 10$) from 0 to 4 dpi (cohort 2) or with IPI-549 ($n = 10$) from 2 to 4 dpi (cohort 3) or were mock-infected and treated with vehicle (sham, $n = 4$). IPI-549 significantly ($P = 0.0133$) extended survival of mice infected with SARS-CoV-2, whether treated from 0 to 4 dpi (cohort 2) or 2 to 4 dpi (cohort 3) (Fig. 5B). Tissue and blood were collected from mice that were surviving on 6 dpi from cohort 3 ($n = 2$) and sham-infected mice ($n = 4$) for viral load, histological, and other assessments. No tissue was collected from mice in cohorts 2 and 3 that died before day 6.

Although PI3K γ inhibitor treatment did not reduce weight loss induced by infection and did not affect viral load during this assay window in cohorts 1, 2, and 3 (Fig. 5, C to F), IPI-549 treatment did reduce lung inflammation in infected mice. We compared lung tissues collected at 2 dpi (cohort 1) and at 6 dpi (cohort 3 and sham infected) for immune cell and epithelial cell content. In contrast with lungs of vehicle-treated, SARS-CoV-2-infected mice, which exhibited substantial macrophage and granulocyte content, lungs of 0 to 4 dpi (cohort 1) and 2 to 4 dpi (cohort 3) IPI-549-treated mice exhibited near-normal frequencies of macrophages ($P < 0.0001$) and granulocytes ($P = 0.0155$) (Fig. 5, G to I). These results indicate that PI3K γ inhibition suppressed SARS-CoV-2-induced lung inflammation in both treatment regimens. PI3K γ blockade by IPI-549 also reduced virus-induced lung damage, because ATI loss detected by prosurfactant C staining, septal wall thickening, vascular congestion, and hemorrhage were equally suppressed in IPI-549-treated mice from cohorts 1 and 3 (Fig. 5, G and J). PI3K γ inhibition suppressed inflammatory cytokine gene and protein expression, as shown for *Tnfa* and *Cxcl10* mRNA in lung tissue and circulating CXCL10 serum proteins (fig. S9, A and B). These results indicate that inhibition of PI3K γ can suppress the damaging inflammation and cytokine surge that accompanies SARS-CoV-2 infection.

We sequenced mRNA isolated from lung tissue of cohorts 1 and 3 and sham-infected mice. Transcriptome analysis revealed that maSARS-CoV-2 infection down-regulated expression of genes

associated with normal lung epithelium and alveolar macrophage function (*Sftpc*, *Siglec1f*, *Muc2*, *Muc4*, and *Muc6*) and T cell function (*Cd3g*, *Cd8b1*, *Rag1*, and *Trdc*) and stimulated expression of genes associated with proinflammatory response pathways, including cytokine/chemokines (*Cxcl9*, *Cxcl10*, *Ccl2*, *Cxcl1*, *Cxcl2*, and *Il6*), IFN response genes (*Oasl*, *Isg15*, *Irf7*, *Ifit1*, *Ifit3*, *Gbp5*, *Gbp8*, and *Gbp9*), and immune exhaustion (*Cd274* and *Lag3*) (fig. S9C). Accordingly, maSARS-CoV-2 infection of mouse lungs was associated with up-regulation of gene expression pathways related to IFN- γ responses, inflammation and epithelial-to-mesenchymal transition, and down-regulation of pathways associated with normal function, including oxidative phosphorylation, DNA repair, and fatty acid metabolism, consistent with SARS-CoV-2 infection in humans (fig. S9D).

To determine the effect of PI3K γ inhibition on lung function and immune responses, we compared transcriptomes from normal lungs (sham) and maSARS-CoV-2-infected lungs that were treated with vehicle or IPI-549. Heatmaps illustrate that IPI-549 treatment of virus-infected animals from dpi 0 to 2 (cohort 1) only modestly affected gene expression compared with treatment with vehicle (fig. S9E). In contrast, IPI-549 treatment from 2 to 4 dpi (cohort 3) significantly ($P_{\text{adj}} < 0.05$) altered gene expression patterns by reducing immune response gene (ISG) and inflammatory gene expression signatures and increasing expression of lung alveolar macrophage genes, such as *Siglec1f*, *Mrc1*, *Csf1r*, *Trem2*, and *Apoe*, to that found in sham-treated lung (fig. S9E). Gene signature and pathway analyses revealed that IPI-549 treatment stimulated blood vessel and epithelial morphogenesis signatures characterized by expression of key endothelial cell regulators (*Vwf*, *Fn1*, *Itga5*, and *Itgb3*), alveolar macrophage markers (*Trem2* and *Apoe*), and other repair genes (fig. S9, F to H). These results are similar to those shown in Fig. 4 for hACE2Tg mice. Together, results from these two mouse models suggest that IPI-549 treatment restored some normal alveolar macrophage and epithelial tissue markers and reduced expression of recruited proinflammatory macrophage markers while also up-regulating markers of tissue repair.

When gene expression signatures between SARS-CoV-2-infected murine and human lungs were compared, overlap was observed primarily in IFN- γ and viral response signatures; expression of these IFN response signatures was strongly suppressed in IPI-549-treated mouse lungs (fig. S9, I and J). IPI-549 treatment was associated with a reduction in gene expression signatures found in other infectious diseases, including hepatitis A, B, and C; pneumonitis; and tuberculosis (fig. S9K). It is notable that PI3K γ inhibition similarly reduced inflammatory response gene signatures and increased signatures of wound repair and vascularization in both young and old mice. These results indicate that PI3K γ inhibition can reduce damaging inflammation in the lung and protect normal lung function during infectious lung disease.

PI3K γ inhibition reduces inflammation, vascular leak, and cytokine storm in mouse models of ARDS

To explore whether PI3K γ inhibition could provide therapeutic benefit in animal models of other pulmonary diseases and identify mechanisms of therapeutic benefit, we inoculated WT and *Pik3cg*^{-/-} mice with methicillin-resistant *Staphylococcus aureus* (MRSA) or multidrug resistant *Escherichia coli* O157:H7 (Fig. 6A and fig. S10A). Whereas all WT-infected mice succumbed to MRSA infection over a period of 24 hours, 40% of *Pik3cg*^{-/-} mice survived infection

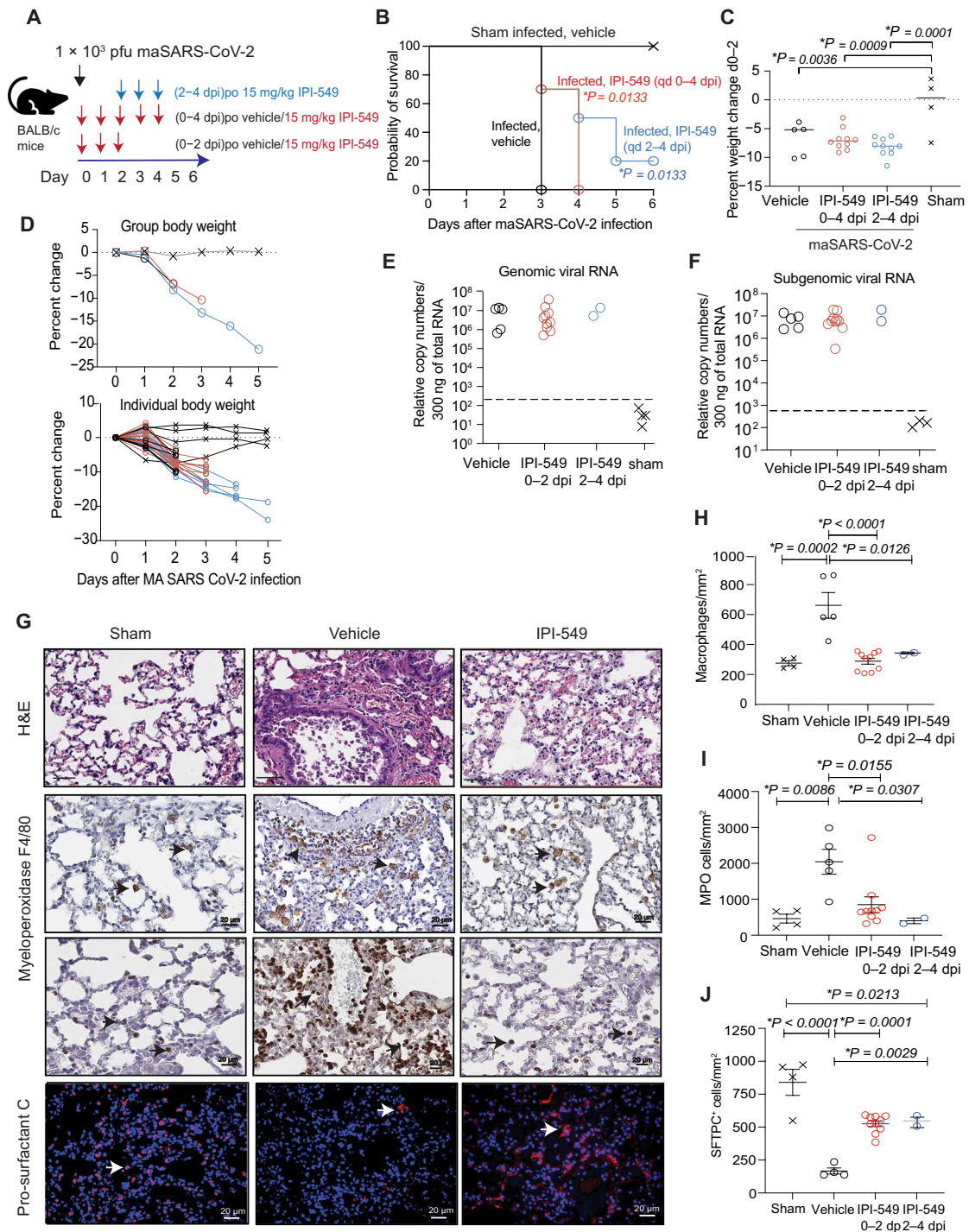


Fig. 5. PI3K γ inhibition suppresses inflammation and promotes survival from maSARS-CoV-2 infection. (A) Schematic of maSARS-CoV-2 infection in 10-month-old mice. Cohorts of mice were inoculated with virus and treated with vehicle or IPI-549 from 0 or 2 dpi. Tissue was collected at 2 dpi or 6 dpi (B) Probability of survival graph of mice treated with vehicle alone (black x, sham infected, $n = 4$) or inoculated with virus and treated with vehicle from 0 to 4 dpi (black open circles, $n = 5$), with IPI-549 from 0 to 4 dpi (red circles, $n = 10$) or with IPI-549 from 2 to 4 dpi (blue circles, $n = 10$). (C) Graph of median weight changes at 2 dpi of mice from each group in (B). (D) Graph of group and individual body weight changes over time in mice from (B). (E and F) Graph of genomic (E) and subgenomic (F) viral RNA relative to total RNA in tissues from mice treated 0 to 2 dpi with vehicle ($n = 5$) or IPI-549 ($n = 10$) (cohort 1) and from surviving mice at day 6 that had been treated 2 to 4 dpi with IPI-549 ($n = 2$) or sham-infected ($n = 4$). Dashed line indicates lower limit of virus detection. (G) Images of H&E as well as anti-F4/80, anti-MPO, and anti-prosurfactant C staining of lung tissues from (A). Arrowheads identify CD68⁺ macrophages, MPO⁺ granulocytes, and prosurfactant C⁺ ATIIL cells. (H to J) Graphs of means \pm SEM of F4/80⁺ macrophages/mm² (H), MPO⁺ granulocytes/mm² (I), and prosurfactant C⁺ cells (J) in tissues from (A). Significance determined by log-rank (Mantel-Cox) test (B), one-way ANOVA with Dunnett's multiple comparisons test (C), or Tukey's multiple comparisons test (H to J).

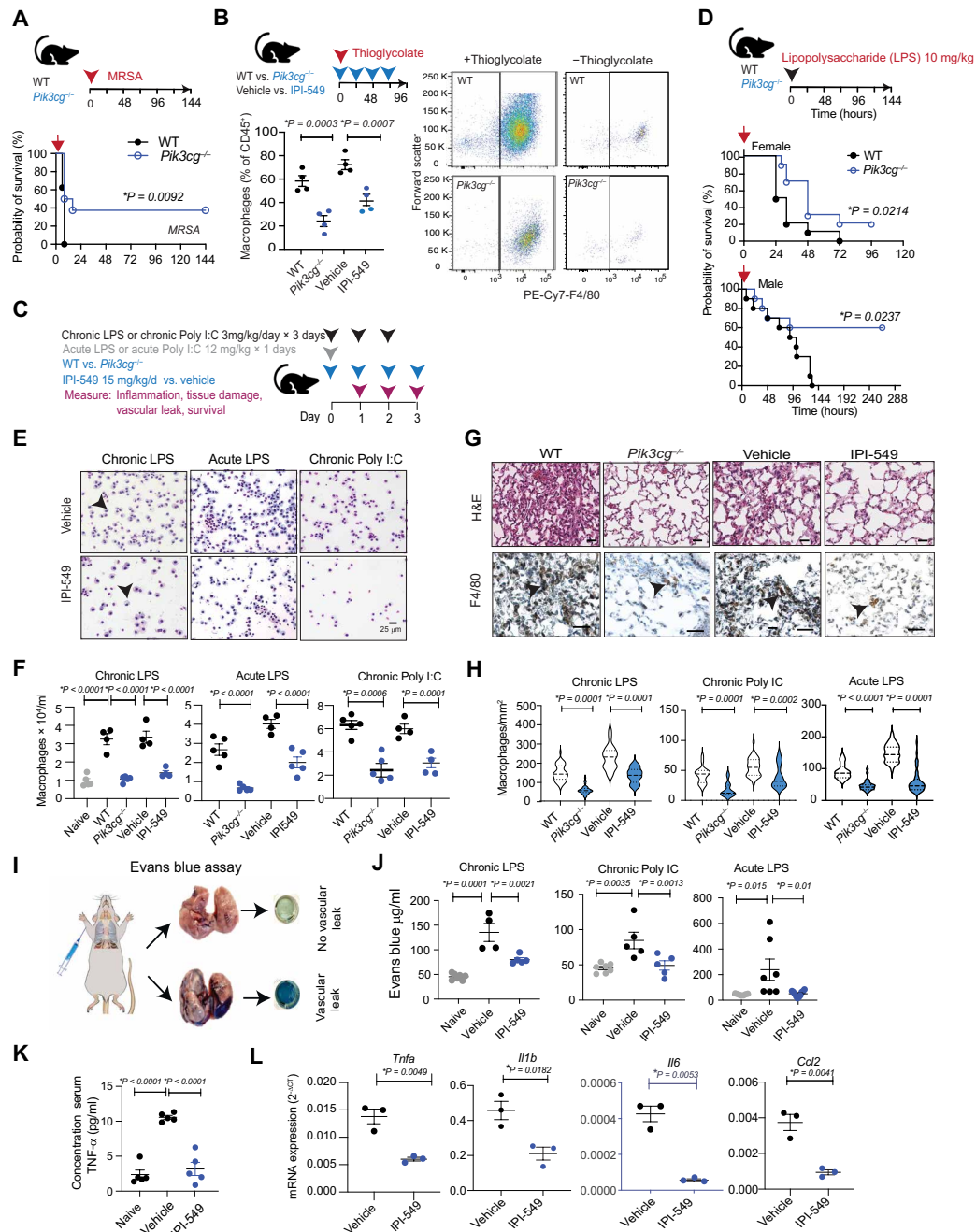


Fig. 6. PI3K γ inhibition suppresses inflammation and promotes survival in mouse models of ARDS and sepsis. (A) Kaplan-Meier survival plots of WT ($n = 8$) and $Pik3cg^{-/-}$ mice ($n = 8$) inoculated with MRSA. (B) Left, graph of mean \pm SEM macrophages in thioglycolate-stimulated peritoneal exudates of WT and $Pik3cg^{-/-}$ ($n = 4$) and in vehicle versus IPI-549-treated mice ($n = 4$). Right, flow cytometry profiles of F4/80⁺ macrophages in peritoneal exudates from WT and $Pik3cg^{-/-}$ animals with and without thioglycolate treatment. (C) Schematic of animal models of ARDS and outcome measures. (D) Kaplan-Meier survival plots of female and male WT ($n = 10$) and $Pik3cg^{-/-}$ ($n = 10$) mice treated once with 10 mg/kg (acute) LPS. (E) Representative images of Giemsa-stained cells in BAL from WT or $Pik3cg^{-/-}$ animals stimulated with 12 mg/kg (acute) LPS or with 3 mg/kg (chronic) LPS or poly I:C and treated with vehicle or IPI-549. Arrowheads indicate macrophages. (F) Graph of macrophages/ml (means \pm SEM) in BAL from WT ($n = 5$) versus $Pik3cg^{-/-}$ ($n = 5$) and vehicle ($n = 5$) versus IPI-549-treated ($n = 5$) animals after treatment with acute LPS, chronic LPS, or chronic poly I:C. (G) H&E and anti-F4/80-stained images of lungs isolated from WT versus $Pik3cg^{-/-}$ and vehicle versus IPI-549-treated animals 96 hours after stimulation with chronic LPS. Arrowheads indicate macrophages. (H) Violin plots of macrophages/mm² (mean and interquartile range indicated by dotted lines) in lungs from WT ($n = 5$) versus $Pik3cg^{-/-}$ ($n = 5$) and vehicle ($n = 5$) versus IPI-549-treated ($n = 5$) animals. (I) Schematic depicting vascular leak assay. (J) Graph of Evans blue concentration (means μ g/ml \pm SEM) in lungs of naïve mice ($n = 7$) or mice treated with chronic LPS ($n = 5$), poly I:C ($n = 5$), or acute LPS ($n = 9$ to 10) and vehicle or IPI-549 treatment. (K) Graph of means \pm SEM pg/ml TNF- α in serum from naïve ($n = 5$) and chronic LPS-stimulated, vehicle- ($n = 5$), or IPI-549-treated ($n = 5$) animals. (L) Graph of cytokine mRNA expression (mean $2^{-\Delta CT} \pm$ SEM) in CD11b⁺ cells from lungs of chronic LPS-stimulated animals treated with vehicle or IPI-549 ($n = 3$). Statistical significance was determined by log-rank Mantel-Cox test (A and D), one-way ANOVA with Tukey's multiple comparisons test (J and K), or t test [(B), (F), (H), and (L)].

(Fig. 6A, $P = 0.0092$). A reduction in serum interleukin-1 β (IL-1 β), a key biomarker in systemic inflammation, was observed in *Pik3cg*^{-/-} animals, although no significant differences in IL-6, bacterial load, or the abilities of WT and *Pik3cg*^{-/-} macrophages to mediate killing of bacteria in vitro by phagocytosis were noted (fig. S10, B to D). These results indicate that PI3K γ inhibition can provide therapeutic benefits in acute infections even without directly affecting pathogen load. We also examined the effects of PI3K γ inhibition during sterile inflammation models using both *Pik3cg*^{-/-} mice and the PI3K γ inhibitor IPI-549. In a model of sterile inflammation, peritoneal administration of thioglycolate, a bacterial nutrient, stimulated substantial macrophage recruitment to the peritoneum that was suppressed by both PI3K γ deletion and IPI-549 treatment (Fig. 6B).

To determine whether PI3K γ controls inflammation in bacterial and viral infection, we investigated mouse models of ARDS, in which acute or chronic poly-inosine:cytosine (poly I:C) or lipopolysaccharide (LPS) administration induces sterile lung inflammation, vascular leak, and local and systemic cytokine elevation (Fig. 6C) (35). Significantly ($P = 0.0214$ female; $P = 0.0237$ male) increased survival from lethal LPS administration was observed in *Pik3cg*^{-/-} animals (Fig. 6D). Analysis of BAL of treated mice demonstrated that each inflammatory stimulus induced significant ($P < 0.0001$) macrophage recruitment to airways that was suppressed at all time points in both *Pik3cg*^{-/-} mice and IPI-549-treated mice (Fig. 6, E and F, and fig. S11, A and B). H&E analysis also revealed that PI3K γ inhibition reduced inflammatory changes in the lung (fig. S11B). In contrast with clear airway spaces in *Pik3cg*^{-/-} and IPI-549-treated animals, WT and vehicle-treated animal lungs exhibit thickened septa, congested vessels, and hemorrhage (Fig. 6G and fig. S11B). PI3K γ inhibition decreased F4/80⁺ macrophage recruitment to the lungs in all inflammation models because substantially fewer macrophages were observed in *Pik3cg*^{-/-} and IPI-549-treated animals than in WT and vehicle-treated animals (Fig. 6, G and H, and fig. S11B).

Vascular leak is a major complicating factor in sepsis, ARDS, and viral pneumonia that is induced by histamine and vascular endothelial growth factor (VEGF) secreted by myeloid cells, as well as other cells in injured tissues. We evaluated the effect of PI3K γ inhibition on vascular leak in the ARDS models using the Miles assays, in which the quantification of intravascular Evans blue dye leakage into tissues serves as a measure of vascular leak (Fig. 6, I and J). Both PI3K γ deletion and IPI-549 treatment suppressed vascular leak in the lungs and other organs in chronic and acute ARDS models, although with some variability between models and tissues (Fig. 6J and fig. S12, A to E). PI3K γ inhibition directly suppresses vascular leak induced by VEGF-A (fig. S12F), suggesting added therapeutic benefit to PI3K γ inhibition in sepsis and infectious diseases characterized by vascular leak.

To determine the role of PI3K γ on cytokine storm associated with severe inflammation, we examined the effect of inhibition PI3K γ on inflammatory cytokine expression in serum and lung myeloid cells. Systemic, acute administration of LPS promoted a transient rise in serum cytokines and chemokines, including tumor necrosis factor- α (TNF- α), IL-1 β , and IL-6, which peaked at 24 hours and returned to normal within 48 hours (fig. S13A). PI3K γ inhibition transiently elevated the expression of some inflammatory cytokines upon acute LPS administration (fig. S13B). In contrast, PI3K γ inhibition suppressed chronic LPS-induced cytokine release, as shown for TNF- α

in serum, BAL, and peritoneal lavage (Fig. 6K and fig. S13, C and D). Chronic LPS stimulated RNA expression of inflammatory cytokines in lung CD11b⁺ cells but not lung CD11b⁻ cells; PI3K γ inhibition substantially reduced expression of inflammatory cytokines in lung myeloid cells (Fig. 6L and fig. S13E). Together, these data indicate that PI3K γ inhibition can reduce inflammation and associated inflammatory sequelae, such as vascular leak, cytokine storm, and lethality in infectious disease models.

PI3K γ inhibition promotes recovery in MHV infection

To evaluate the impact of dampening myeloid cell infiltration in viral pneumonia, mice that were intranasally inoculated with the betacoronavirus murine hepatitis virus (MHV-A59) were treated with the PI3K γ inhibitor IPI-549 or vehicle and compared with sham-infected animals (Fig. 7A). MHV administered intranasally induces nonlethal pneumonia that lasts approximately 10 days (36). Treatment with IPI-549, but not vehicle, partially attenuated virus-induced weight loss without affecting viral load from 5 dpi (Fig. 7, B and C). Treatment with IPI-549 substantially inhibited airway inflammation; fewer macrophages were present in BAL collected from IPI-549-treated versus vehicle-treated animals 5 dpi (Fig. 7D). PI3K γ blockade also reduced lung septal wall thickening, vascular congestion, and hemorrhage (Fig. 7E and fig. S14) while substantially reducing macrophage and granulocyte infiltration of lungs at all time points after viral infection (Fig. 7, E to G, and fig. S14).

Our previous results indicated that PI3K γ inhibition may reduce virus-induced cytokine storm; therefore, we quantified cytokine concentrations in serum and mRNA expression of cytokines in lung tissue from sham-infected and MHV-infected mice treated with vehicle or IPI-549. IPI-549 treatment reduced TNF- α , IFN- γ , IL-12, IL-6, and CXCL10 in serum (Fig. 7H). Viral infection increased expression of genes encoding proinflammatory cytokines, inflammatory signaling factors, and T cell biomarkers in the lung (Fig. 7I). In contrast, PI3K γ inhibition reduced expression of these factors, particularly at later time points (Fig. 7I). Because elevated serum cytokines are associated with severe or lethal coronavirus infection (1, 2), these results suggest that PI3K γ inhibition can suppress myeloid cell accumulation and expression of inflammatory cytokines that contribute to cytokine storm.

DISCUSSION

Infectious diseases like SARS-CoV-2 continue to kill millions of individuals worldwide (37). Despite increased attention to disease prevention and management, new therapeutic approaches are still needed to manage this and other aggressive pulmonary infections, which are characterized by aberrant pulmonary and systemic inflammation leading to ARDS, vascular leak, coagulation, and fatal organ damage (1, 2). Here, we showed using animal models of disease that PI3K γ inhibition with the clinical inhibitor IPI-549 (eganalisib) can protect against ARDS, vascular damage, and, in some cases, lethality induced by severe infectious agents such as MRSA and SARS-CoV-2.

SARS-CoV-2 and other viral and bacterial infections in mouse, hamster, and human are characterized by extensive recruitment of PI3K γ -expressing wound healing-type, profibrotic monocyte/macrophages and granulocytes to the lungs, concomitant with loss of surfactant C-expressing alveolar cells. Several studies have revealed neutrophilia in blood and extensive neutrophil infiltration of

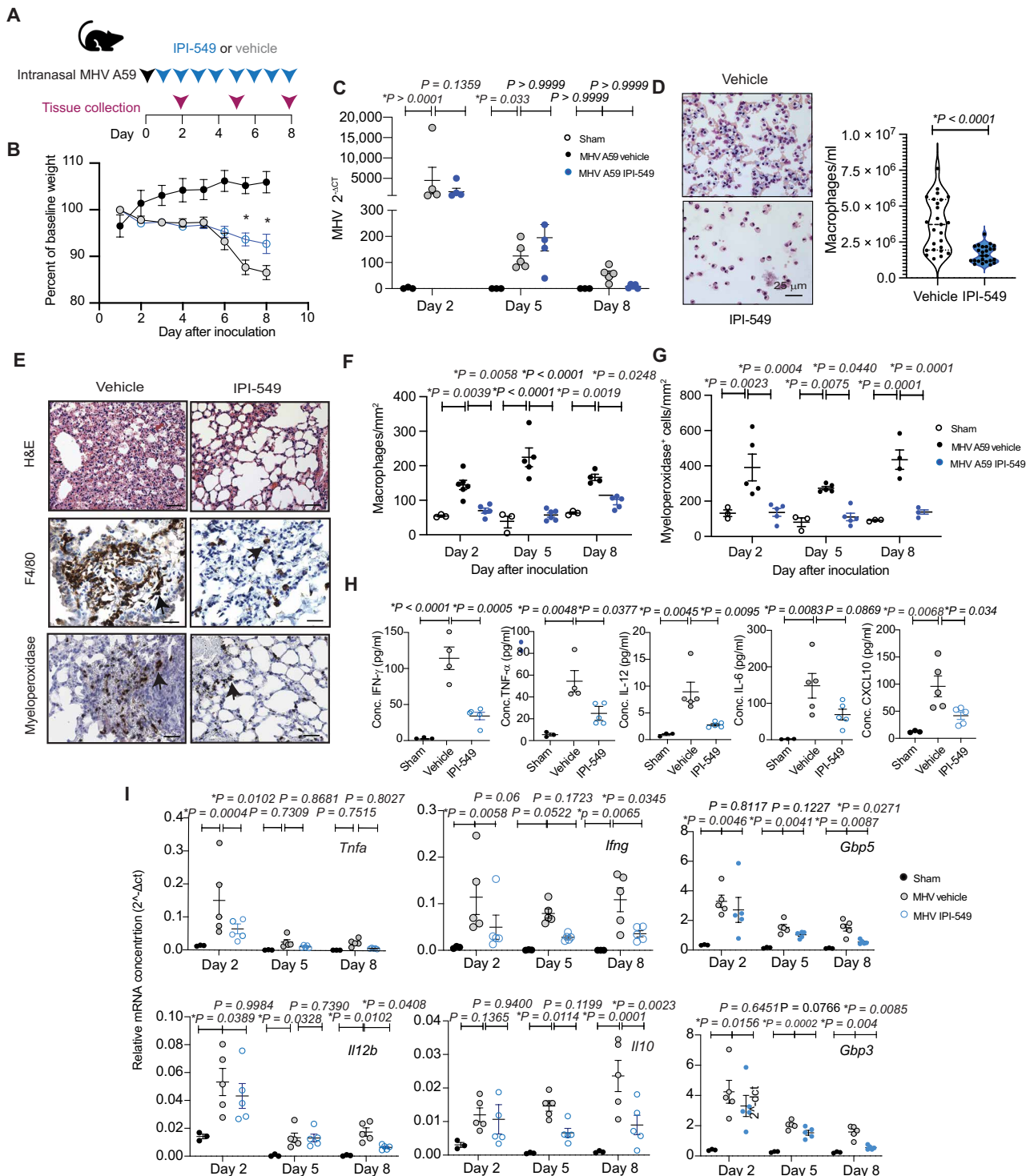


Fig. 7. The PI3Ky inhibitor IPI-549 reduces inflammation and promotes recovery in a mouse model of MHV infection. (A) Schematic of MHV A59 pulmonary infection, treatment, and tissue collection. (B) Time course graph of means \pm SEM weight changes in sham-infected ($n = 5$) or MHV-infected mice treated with vehicle ($n = 5$) or IPI-549 ($n = 5$). (C) Graph of means \pm SEM MHV nucleocapsid N gene transcripts ($2^{-\Delta CT}$) determined by quantitative RT-PCR normalized to L32 ribosomal protein house-keeping gene in lungs from sham-infected ($n = 3$) and MHV-infected mice treated with vehicle ($n = 5$ per time point) or IPI-549 ($n = 5$ per time point). (D) Images of Giemsa-stained cells and graphs of macrophages/ml quantification in BAL from MHV-infected animals at 5 dpi after treatment with vehicle or IPI-549. (E) Images of H&E, anti-F4/80-, and anti-MPO-stained lung tissues from (B). Arrowheads indicate macrophages and granulocytes. (F and G) Graphs of means \pm SEM F4/80⁺ macrophages/mm² (F) and MPO⁺ granulocytes/mm² (G) from (E). (H) Graph of cytokine concentration \pm SEM in sera of mice treated from (A). (I) Graph of mRNA expression ($2^{-\Delta CT}$) of inflammatory factors relative to *Gapdh* in lung lysates from (A). Statistical significance was determined by *t* test (B and D) or by one-way ANOVA with Tukey's multiple comparisons test [(C) and (F) to (I)].

airways in patients with COVID-19 (35). Neutrophils can damage tissues in part through NETosis, the release of intracellular proteinases and DNA that can create a physical trap for bacteria but can also induce thrombosis and damage organs (38). Because they self-destruct in tissues, neutrophils can be difficult to study. Our use of spatial transcriptomics and fixed-tissue RNA sequencing provided an opportunity to characterize neutrophil and macrophages' roles in lungs from individuals with COVID-19. Recent single-cell sequencing studies demonstrated increased macrophages and fibroblasts in lungs from patients with COVID-19, consistent with our findings (3).

Our studies uniquely compare and contrast inflammation and transcriptomics in the response to COVID-19 in both BAL specimens and lung tissues from patients with COVID-19. These studies show that BAL reveals a subset of the inflammation and damage done to lungs during diseases like COVID-19 and demonstrates the recruitment of immature monocytes and neutrophils to the site of infection. Analysis of lung tissue, however, reveals that the alveolar spaces of the infected lung are replaced by extensive macrophage recruitment, interstitial inflammation, and remodeling of tissue extracellular matrix, features that cannot be revealed in BAL specimens. Extensive areas of the infected lung are compromised by fibrosis and lung collapse and thus would not be accessible to lavage. Ongoing viral infections were associated with greater abundance of immature myeloid cells (myeloid-other) and CD163⁺CD68⁺ macrophages and increased expression of PD-L1 on dendritic cells and granulocytes. Virus-negative patients exhibited much greater fibroblast content.

We further showed that PI3K γ is expressed in myeloid cells from SARS-CoV-2-infected human and animal tissues, suggesting a potential therapeutic target for reduction of inflammation, vascular leak, cytokine storm, and mortality from infectious lung diseases. We then demonstrated that inhibition of myeloid cell recruitment to infected lungs with the clinical PI3K γ inhibitor IPI-549 promoted survival and recovery in animal models of sterile inflammation and infectious disease. IPI-549, also called egeanlisib, is currently in cancer immune therapy phase 2 clinical trials. Antagonism of PI3K γ reduced myeloid cell recruitment to lungs in several models of inflammation and infection. RNA expression analysis showed that lungs of patients with COVID-19 and SARS-CoV-2-infected animals exhibited inflammation as well as a T_H2-like, immune-suppressed, wound-healing profile, which was suppressed prevented in animals by PI3K γ inhibition. Our studies thus indicated that PI3K γ inhibition can reduce inflammatory disease by suppressing organ-damaging sequelae, such as fibrosis, vascular leak, and cytokine storm.

Our study has some limitations. Whereas PI3K γ inhibition reduces myeloid cell recruitment, weight loss, and lung damage associated with SARS-CoV-2 and other infections, our studies did not show a curative benefit in animal models of SARS-CoV-2 infection. PI3K γ inhibition did extend the survival of aging animals infected with SARS-CoV-2 in two separate cohorts of one study, although these studies need to be repeated and extended. In addition, our analyses of biological materials from SARS-CoV-2-infected patients and animals were largely limited to fixed tissues for biosafety reasons. Further analyses of the mechanisms by which myeloid cells and PI3K γ promote SARS-CoV-2-mediated inflammation and disease progression are needed to learn how to modulate viral diseases such as SARS-CoV-2 and the inflammation that is associated with them.

Together, these results indicate that PI3K γ inhibition can reduce recruitment of inflammatory neutrophils, monocytes, and macrophages to the lung, which in turn lessens damage to the lung and distal organs by preventing cytokine surge and vascular leak. These results indicate that IPI-549 might provide benefit to patients with infectious lung diseases including and beyond COVID-19.

MATERIALS AND METHODS

Study design

The objective of this study was to investigate the contributions of macrophages and granulocytes to the progression of COVID-19 and other inflammatory lung diseases and to evaluate the therapeutic potential of PI3K γ inhibition to ameliorate inflammation and progression of disease. Immune cell content and state were investigated in lungs and BAL specimens from normal donors and in individuals with COVID-19 or other inflammatory diseases. In this study, immune cell composition and state were investigated in lungs and BAL specimens from uninfected patients and patients with COVID-19, using IHC, mIHC, RNA sequencing, and spatial transcriptomics. The effect of PI3K γ inhibition on disease progression was evaluated in *Pik3cg*^{-/-} mice and mice treated with the PI3K γ antagonist, IPI-549. Animal models included infection with SARS-CoV-2, MHV, MRSA, and antibiotic-resistant *E. coli* as well as ARDS induced by LPS and PolyI:C administration. Survival, weight loss, inflammation, and vascular leak were measured as an index of disease progression. Inflammation in lung tissue was measured by IHC for macrophage, granulocyte, and alveolar epithelial cell content. Serum and lung cytokines were measured by multiplex enzyme-linked substrate assay, and gene expression was measured in lung tissue by RNA sequencing.

For studies evaluating the effect of PI3K γ inhibition on inflammation in mice, a sample size of at least 10 mice per group provided 80% power to detect mean difference of 2.25 SD between two groups (based on a two-sample *t* test with two-sided 5% significance level). Mice were randomized after infection before treatment with inhibitors or controls. Where feasible, treatment groups were blinded until study end. All data are from biological replicates. Before statistical analyses, data were examined for normal distribution and possible outliers. In these studies, no data points were omitted. Animal studies were ended when mouse weight loss was greater than 20% of starting body weight or at predetermined designated end points. All animal studies and histological analyses were performed with investigators blinded to study group identity.

IHC and RNA sequencing were performed on lung tissues from patients with COVID-19 ($n = 15$) and normal patients ($n = 5$), as well as BAL isolates from patients with SARS-CoV-2 ($n = 7$) and uninfected patients ($n = 3$). All animal experiments were performed two to six times with $n = 5$ to 15 per group, except the maSARS-CoV-2 viral infection study in 270-day-old mice, which was performed once, with $n = 5$ to 20 mice per group. ARDS and vascular leak studies with LPS and PolyI:C were performed three to five times each, with $n = 5$ to 10 per group.

Human participants

All human tissue analyses were conducted on deidentified tissue under guidelines established by the IRB for human participant research of the UCSF. Postmortem tissue studies received IRB exemption from oversight because research on deceased patients is not classified as human participant research by the US Department of Health

and Human Services or the US Food and Drug Administration. All patients in this study were admitted early in the pandemic during the first 3 to 6 months after the first cases of COVID-19 were reported in the US when no specific therapeutics had been developed. Deidentified lung tissue was obtained upon rapid autopsy of deceased patients with COVID-19, formalin-fixed for 48 hours, and processed by the Department of Pathology, UCSD, into paraffin-embedded tissue blocks by the Moores Cancer Center Histology Shared Resource, UCSD, San Diego, CA. Normal human lung tissue was obtained from consenting patients during lung cancer surgery at the Moores Cancer Center, UCSD and processed into paraffin-embedded tissue blocks by the UCSD Department of Pathology. BAL cells from consenting patients infected with SARS-CoV-2 and from consenting hospitalized patients who were diagnosed with no infections were pelleted, fixed, paraffin embedded, and sectioned. All tissue was used for IHC and bioinformatics analysis.

Animals

Eight- to 9-week-old C57BL/6 stock 000664 (RRID: IMSR_JAX:000664) male and female mice were purchased from the Jackson Laboratories. Six- to eight-week-old male K18-hACE2 (RRID: IMSR_JAX:034860) mice were purchased from the Jackson Laboratories. Ten-month-old female Balb/c animals (RRID: IMSR_CRL:028) were purchased from Charles River for SARS-CoV-2 infection studies. Six- to 7-week-old golden Syrian hamsters (*Mesocricetus auratus*; genotype: HsdHan: AURA) were from Envigo. *Pik3cg^{-/-}* mice on the C57BL/6 background (RRID: MGI:3619226) were maintained in the Varner laboratory at the UCSD. All MRSA, MHV, and ARDS studies were performed at the UCSD with the approval of the Institutional Animal Care and Use Committees and Institutional Biosafety Committees of the UCSD. MRSA and MHV studies were conducted in animal biosafety level 1 (ABSL2) facilities at UCSD. ARDS studies were performed in ABSL1 facilities at UCSD. SARS-CoV-2 infection of K18-hACE2 mice studies were performed at the Scripps Research Institute with the approval of the Institutional Animal Care and Use Committee of the Scripps Research Institute. maSARS-CoV-2 models were conducted in ABSL3 facilities with support from the National Institutes of Health (NIH)–Accelerating COVID-19 Therapeutic Interventions and Vaccines (ACTIV) program of NIAID, NIH at the Institute for Antiviral Research, Animal, Dairy and Veterinary Science, Utah State University, Logan, UT, with the approval of the Institutional Animal Care and Use Committees and Institutional Biosafety Committees of Utah State University. SARS-CoV-2 hamster studies were performed at the Department of Infectious Diseases and Global Health, Tufts University Cummings School of Veterinary Medicine. All animal experiments were performed with the approval of the Institutional Animal Care and Use Committees and Institutional Biosafety Committees of Tufts University. SARS-CoV-2 hamster experiments were conducted in ABSL3 facilities on the campus of Tufts University.

Statistical analysis

All data points as well as the means \pm SEM were graphed using Graph Pad Prism version 9.1.0. Results were analyzed statistically using one-way analysis of variance (ANOVA) with Tukey's or Dunnett's post hoc test for multiple-group analyses, Student's *t* test for parametric two-sample analysis, Mann Whitney test for nonparametric two-sample analysis, and log-rank (Mantel-Cox) test for survival analysis using Graph Pad Prism version 9.1.0. D'Agostino-Pearson and Kolmogorov-Smirnov normality testing using Graph Pad Prism

version 9.1.0 was performed to inform selection of parametric versus nonparametric significance testing. Data with $P \leq 0.05$ were considered statistically significant. Statistical significance in differential gene expression analysis was performed by limma-voom method, where $P_{\text{adj}} < 0.05$. Raw datasets were deposited to Dryad (<https://doi.org/10.5061/dryad.sf7m0cgbm>).

Supplementary Materials

This PDF file includes:

Materials and Methods
Figs. S1 to S14
Tables S1 to S6
References (39–56)

Other Supplementary Material for this manuscript includes the following:

MDAR Reproducibility Checklist

REFERENCES AND NOTES

1. J. Liu, X. Zheng, Q. Tong, W. Li, B. Wang, K. Sutter, M. Trilling, M. Lu, U. Dittmer, D. Yang, Overlapping and discrete aspects of the pathology and pathogenesis of the emerging human pathogenic coronaviruses SARS-CoV, MERS-CoV, and 2019-nCoV. *J. Med. Virol.* **92**, 491–494 (2020).
2. E. J. Giamarellos-Bourboulis, M. G. Netea, N. Rovina, K. Akinosoglou, A. Antoniadou, N. Antonakos, G. Damoraki, T. Gkavogianni, M. E. Adami, P. Katsaounou, M. Ntaganou, M. Kyriakopoulou, G. Dimopoulos, I. Koutsodimitropoulos, D. Velissaris, P. Koufargyris, A. Karageorgos, K. Katrini, V. Lekakis, M. Lupse, A. Kotsaki, G. Renieris, D. Theodoulou, V. Panou, E. Koukaki, N. Koulouris, C. Gogos, A. Koutsoukou, Complex immune dysregulation in COVID-19 patients with severe respiratory failure. *Cell Host Microbe* **27**, 992–1000.e3 (2020).
3. J. C. Melms, J. Biermann, H. Huang, Y. Wang, A. Nair, S. Tagore, I. Katsyv, A. F. Rendeiro, A. D. Amin, D. Schapiro, C. J. Frangieh, A. M. Luoma, A. Filliol, Y. Fang, H. Ravichandran, M. G. Clausi, G. A. Alba, M. Rogava, S. W. Chen, P. Ho, D. T. Montoro, A. E. Kornberg, A. S. Han, M. F. Bakhoum, N. Anandasabapathy, M. Suárez-Fariñas, S. F. Bakhoum, Y. Bram, A. Borczuk, X. V. Guo, J. H. Lefkowitz, C. Marboe, S. M. Laguna, A. Del Portillo, E. J. Tsai, E. Zorn, G. S. Markowitz, R. F. Schwabe, R. E. Schwartz, O. Elemento, A. Saqi, H. Hibshoosh, J. Que, B. Izar, A molecular single-cell lung atlas of lethal COVID-19. *Nature* **595**, 114–119 (2021).
4. S. T. Chen, M. D. Park, D. M. Del Valle, M. Buckup, A. Tabachnikova, R. C. Thompson, N. W. Simons, K. Mouskas, B. Lee, D. Geanon, D. D'Souza, T. Dawson, R. Marvin, K. Nie, Z. Zhao, J. LeBerichel, C. Chang, H. Jamal, G. Akturk, U. Chaddha, K. Mathews, S. Acquah, S. A. Brown, M. Reiss, T. Harkin, M. Feldmann, C. A. Powell, J. L. Hook, S. Kim-Schulze, A. H. Rahman, B. D. Brown, Mount Sinai COVID-19 Biobank Team, N. D. Beckmann, S. Gnjatich, E. Kenigsberg, A. W. Charney, M. Merad, A shift in lung macrophage composition is associated with COVID-19 severity and recovery. *Sci. Transl. Med.* **14**, eabn5168 (2022).
5. A. F. Rendeiro, H. Ravichandran, Y. Bram, V. Chandar, J. Kim, C. Meydan, J. Park, J. Foox, T. Hether, S. Warren, Y. Kim, J. Reeves, S. Salvatore, C. E. Mason, E. C. Swanson, A. C. Borczuk, O. Elemento, R. E. Schwartz, The spatial landscape of lung pathology during COVID-19 progression. *Nature* **593**, 564–569 (2021).
6. R. Channappanavar, A. R. Fehr, J. Zheng, C. Wohlford-Lenane, J. E. Abrahante, M. Mack, R. Sompallae, P. B. McCray Jr., D. K. Meyerholz, S. Perlman, IFN-I response timing relative to virus replication determines MERS coronavirus infection outcomes. *J. Clin. Invest.* **129**, 3625–3639 (2019).
7. M. Yoshida, K. B. Worlock, N. Huang, R. G. H. Lindeboom, C. R. Butler, N. Kumasaka, C. D. Conde, L. Mamanova, L. Bolt, L. Richardson, K. Polanski, E. Madisson, J. L. Barnes, J. Allen-Hyttinen, E. Kilich, B. C. Jones, A. de Wilton, A. Wilbrey-Clark, W. Sungnak, J. P. Pett, J. Weller, E. Prigmore, H. Yung, P. Mehta, A. Saleh, A. Saigal, V. Chu, J. M. Cohen, C. Cane, A. Iordanidou, S. Shibuya, A. K. Reuschl, I. T. Herczeg, A. C. Argento, R. G. Wunderink, S. B. Smith, T. A. Poor, C. A. Gao, J. E. Dematte, NU SCRIPT Study Investigators, G. Reynolds, M. Haniffa, G. S. Bowyer, M. Coates, M. R. Clatworthy, F. J. Calero-Nieto, B. Göttgens, C. O'Callaghan, N. J. Sebire, C. Jolly, P. De Coppi, C. M. Smith, A. V. Misharin, S. M. Janes, S. A. Teichmann, M. Z. Nikolic, K. B. Meyer, Local and systemic responses to SARS-CoV-2 infection in children and adults. *Nature* **602**, 321–327 (2022).
8. M. C. Schmid, C. J. Avraamides, H. C. Dippold, I. Franco, P. Foubert, L. G. Ellies, L. M. Acevedo, J. R. Manglicmot, X. Song, W. Wrasidlo, S. L. Blair, M. H. Ginsberg, D. A. Chereshe, E. Hirsch, S. J. Field, J. A. Varner, Receptor tyrosine kinases and TLR/IL1Rs unexpectedly activate myeloid cell PI3K γ , a single convergent point promoting tumor inflammation and progression. *Cancer Cell* **19**, 715–727 (2011).

9. M. M. Kameda, K. S. Messer, N. Ralainirina, H. Li, C. J. Leem, S. Gorjestani, G. Woo, A. V. Nguyen, C. C. Figueiredo, P. Foubert, M. C. Schmid, M. Pink, D. G. Winkler, M. Rausch, V. J. Palombella, J. Kutok, K. McGovern, K. A. Frazier, X. Wu, M. Karin, R. Sasik, E. E. Cohen, J. A. Varner, PI3K γ is a molecular switch that controls immune suppression. *Nature* **539**, 437–442 (2016).
10. M. M. Kameda, P. Cappello, A. V. Nguyen, N. Ralainirina, C. R. Hardamon, P. Foubert, M. C. Schmid, P. Sun, E. Mose, M. Bouvet, A. M. Lowy, M. A. Valasek, R. Sasik, F. Novelli, E. Hirsch, J. A. Varner, Macrophage PI3K γ drives pancreatic ductal adenocarcinoma progression. *Cancer Discov.* **6**, 870–885 (2016).
11. E. L. Martin, D. G. Souza, C. T. Fagundes, F. A. Amaral, B. Assenzio, V. Puntorieri, L. Del Sorbo, V. Fanelli, M. Bosco, L. Delsedime, J. F. Pinho, V. S. Lemos, F. O. Souto, J. C. Alves-Filho, F. Q. Cunha, A. S. Slutsky, T. Ruckle, E. Hirsch, M. M. Teixeira, V. M. Ranieri, Phosphoinositide-3 kinase gamma activity contributes to sepsis and organ damage by altering neutrophil recruitment. *Am. J. Respir. Crit. Care Med.* **182**, 762–773 (2010).
12. O. De Henau, M. Rausch, D. Winkler, L. F. Campesato, C. Liu, D. H. Cymerman, S. Budhu, A. Ghosh, M. Pink, J. Tchaicha, M. Douglas, T. Tibbitts, S. Sharma, J. Proctor, N. Kosmider, K. White, H. Stern, J. Soglia, J. Adams, V. J. Palombella, K. McGovern, J. L. Kutok, J. D. Wolchok, T. Merghoub, Overcoming resistance to checkpoint blockade therapy by targeting PI3K γ in myeloid cells. *Nature* **539**, 443–447 (2016).
13. B. Chmielowski, R. Sullivan, M. Postow, A. Patnaik, G. Shapiro, E. E. W. Cohen, M. Gutierrez, C. Steuer, A. Ribas, L. Lee, B. O'Connell, J. Kutok, J. Roberts, S. Mahabhashyam, M.-L. Fjallogk, J. D. Wolchok, D. Hong, The first clinical/translational data from the expansion cohorts of a Ph1/1b study of IPI-549, a tumor macrophage-reprogramming small molecule, in combination with nivolumab in advanced solid tumors. *J. Immunotherapy Cancer* **6** (Suppl. 1), abstract no. P716 (2018).
14. D. S. Hong, M. Postow, B. Chmielowski, R. Sullivan, A. Patnaik, E. E. W. Cohen, G. Shapiro, C. Steuer, M. Gutierrez, H. Yeckes-Rodin, R. Ilaria, B. O'Connell, J. Peng, G. Peng, N. Zizlsparger, A. Tolcher, J. D. Wolchok, Eganalisib, a first-in-class PI3K- γ inhibitor, in patients with advanced solid tumors: Results of the phase 1/1b MARIO-1 Trial. *Clin. Cancer Res.* **29**, 2210–2219 (2023).
15. T. Tsujikawa, S. Kumar, R. N. Borkar, V. Azimi, G. Thibault, Y. H. Chang, A. Balter, R. Kawashima, G. Choe, D. Sauer, E. El Rassi, D. R. Clayburgh, M. F. Kulesz-Martin, E. R. Lutz, L. Zheng, E. M. Jaffee, P. Leyshock, A. A. Margolin, M. Mori, J. W. Gray, P. W. Flint, L. M. Coussens, Quantitative multiplex immunohistochemistry reveals myeloid-inflamed tumor-immune complexity associated with poor prognosis. *Cell Rep.* **19**, 203–217 (2017).
16. W. Ni, X. Yang, D. Yang, J. Bao, R. Li, Y. Xiao, C. Hou, H. Wang, J. Liu, D. Yang, Y. Xu, Z. Cao, Z. Gao, Role of angiotensin-converting enzyme 2 (ACE2) in COVID-19. *Crit. Care* **24**, 422 (2020).
17. M. H. Barros, F. Hauck, J. H. Dreyer, B. Kempkes, G. Niedobitek, Macrophage polarisation: An immunohistochemical approach for identifying M1 and M2 macrophages. *PLOS ONE* **8**, e80908 (2013).
18. M. K. Skytthe, J. H. Graversen, S. K. Moestrup, Targeting of CD163⁺ macrophages in inflammatory and malignant diseases. *Int. J. Mol. Sci.* **21**, 5497 (2020).
19. F. J. Gil-Etayo, P. Suárez-Fernández, O. Cabrera-Marante, D. Arroyo, S. Garcinuño, L. Naranjo, D. E. Pleguezuelo, L. M. Allende, E. Mancebo, A. Lalueza, R. Diaz-Simón, E. Paz-Artal, A. Serrano, T helper cell subset response is a determining factor in COVID-19 progression. *Front. Cell. Infect. Microbiol.* **11**, 624483 (2021).
20. B. Diao, C. Wang, Y. Tan, X. Chen, Y. Liu, L. Ning, L. Chen, M. Li, Y. Liu, G. Wang, Z. Yuan, Z. Feng, Y. Zhang, Y. Wu, Y. Chen, Reduction and functional exhaustion of t cells in patients with coronavirus disease 2019 (COVID-19). *Front. Immunol.* **11**, 827 (2020).
21. X. Wang, G. Wang, Z. Wang, B. Liu, N. Han, J. Li, C. Lu, X. Liu, Q. Zhang, Q. Yang, G. Wang, PD-1-expressing B cells suppress CD4⁺ and CD8⁺ T cells via PD-1/PD-L1-dependent pathway. *Mol. Immunol.* **109**, 20–26 (2019).
22. C. L. Trejo, M. Babić, E. Imler, M. Gonzalez, S. I. Bibikov, P. J. Shepard, H. C. VanSteenhouse, J. M. Yeakley, B. E. Seligmann, Extraction-free whole transcriptome gene expression analysis of FFPE sections and histology-directed subareas of tissue. *PLOS ONE* **14**, e0212031 (2019).
23. A. K. Turnbull, C. Selli, C. Martinez-Perez, A. Fernando, L. Renshaw, J. Keys, J. D. Figueroa, X. He, M. Tanioka, A. F. Munro, L. Murphy, A. Fawkes, R. Clark, A. Coutts, C. M. Perou, L. A. Carey, J. M. Dixon, A. H. Sims, Unlocking the transcriptomic potential of formalin-fixed paraffin embedded clinical tissues: Comparison of gene expression profiling approaches. *BMC Bioinfo.* **21**, 30 (2020).
24. P. Danaher, Y. Kim, B. Nelson, M. Griswold, Z. Yang, E. Piazza, J. M. Beechem, Advances in mixed cell deconvolution enable quantification of cell types in spatial transcriptomic data. *Nat. Commun.* **13**, 385 (2022).
25. M. D. Robinson, D. J. McCarthy, G. K. Smyth, edgeR: A bioconductor package for differential expression analysis of digital gene expression data. *Bioinformatics* **26**, 139–140 (2010).
26. R. Shaykhiev, Emerging biology of persistent mucous cell hyperplasia in COPD. *Thorax* **74**, 4–6 (2019).
27. P. A. Szabo, P. Dogra, J. I. Gray, S. B. Wells, T. J. Connors, S. P. Weisberg, I. Krupska, R. Matsumoto, M. M. L. Poon, E. Idzikowski, S. E. Morris, C. Pasin, A. J. Yates, A. Ku, M. Chait, J. Davis-Porada, X. V. Guo, J. Zhou, M. Steinle, S. Mackay, A. Saqi, M. R. Baldwin, P. A. Sims, D. L. Farber, Longitudinal profiling of respiratory and systemic immune responses reveals myeloid cell-driven lung inflammation in severe COVID-19. *Immunity* **54**, 797–814.e6 (2021).
28. S. D. Stampfer, M. S. Goldwater, S. Bujarski, B. Regidor, W. Zhang, A. J. Feinstein, R. Swift, S. Eshaghian, E. Vail, J. R. Berenson, Severe breakthrough COVID-19 with a heavily mutated variant in a multiple myeloma patient 10 weeks after vaccination. *Clin. Infect. Pract.* **13**, 100130 (2022).
29. M. S. Palanki, E. Dneprovskaja, J. Doukas, R. M. Fine, J. Hood, X. Kang, D. Lohse, M. Martin, G. Noronha, R. M. Soll, W. Wrasidlo, S. Yee, H. Zhu, Discovery of 3,3'-(2,4-diaminopteridine-6,7-diy) diphenol as an isozyme-selective inhibitor of PI3K for the treatment of ischemia reperfusion injury associated with myocardial infarction. *J. Med. Chem.* **50**, 4279–4294 (2007).
30. D. Serban, J. Leng, D. Cheresif, H-ras regulates angiogenesis and vascular permeability by activation of distinct downstream effectors. *Circ. Res.* **102**, 1350–1358 (2008).
31. L. H. Tostanoski, F. Wegmann, A. J. Martinot, C. Loos, K. McMahan, N. B. Mercado, J. Yu, C. N. Chan, S. Bondoc, C. E. Starke, M. Nekorchuk, K. Busman-Sahay, C. Piedra-Mora, L. M. Wrijil, S. Ducat, J. Custers, C. Atyeo, S. Fischinger, J. S. Burke, J. Feldman, B. M. Hauser, T. M. Caradonna, E. A. Bondzie, G. Dagotto, M. S. Gebre, C. Jacob-Dolan, Z. Lin, S. H. Mahrokhian, F. Nampanya, R. Nityanandam, L. Pessaint, M. Porto, V. Ali, D. Benetiene, K. Tevi, H. Andersen, M. G. Lewis, A. G. Schmidt, D. A. Lauffenburger, G. Alter, J. D. Estes, H. Schuitemaker, R. Zahn, D. H. Barouch, Ad26 vaccine protects against SARS-CoV-2 severe clinical disease in hamsters. *Nat. Med.* **26**, 1694–1700 (2020).
32. P. B. McCray, L. Pewe, C. Wohlford-Lenane, M. Hickey, L. Manzel, L. Shi, J. Netland, H. P. Jia, C. Halabi, C. D. Sigmund, D. K. Meyerholz, P. Kirby, D. A. Cook, S. Perlman, Lethal infection of K18-hACE2 mice infected with severe acute respiratory syndrome coronavirus. *J. Virol.* **81**, 813–821 (2007).
33. O. Franzén, L.-M. Gan, J. L. M. Björkegren, PanglaoDB: A web server for exploration of mouse and human single-cell RNA sequencing data. *Database* **2019**, baz046 (2019).
34. S. R. Leist, K. H. Dinnon III, A. Schäfer, L. V. Tse, K. Okuda, Y. J. Hou, A. West, C. E. Edwards, W. Sanders, E. J. Fritch, K. L. Gully, T. Scobey, A. J. Brown, T. P. Sheahan, N. J. Moorman, R. C. Boucher, L. E. Gralinski, S. A. Montgomery, R. S. Baric, A mouse-adapted SARS-CoV-2 induces acute lung injury and mortality in standard laboratory mice. *Cell* **183**, 1070–1085.e12 (2020).
35. J. A. Bastarache, T. S. Blackwell, Development of animal models for the acute respiratory distress syndrome. *Dis. Model. Mech.* **2**, 218–223 (2009).
36. Z. Yang, J. Du, G. Chen, J. Zhao, X. Yang, L. Su, G. Cheng, H. Tang, Coronavirus MHV-A59 infects the lung and causes severe pneumonia in C57BL/6 mice. *Virol. Sin.* **29**, 393–402 (2014).
37. K. W. Hendrickson, I. D. Peltan, S. M. Brown, The epidemiology of acute respiratory distress syndrome before and after coronavirus disease 2019. *Crit. Care Clin.* **37**, 703–716 (2021).
38. E. A. Middleton, X. Y. He, F. Denorme, R. A. Campbell, D. Ng, S. P. Salvatore, M. Mostyka, A. Baxter-Stoltzfus, A. C. Borczuk, M. Loda, M. J. Cody, B. K. Manne, I. Portier, E. S. Harris, A. C. Petrey, E. J. Beswick, A. F. Caulin, A. Iovino, L. M. Abegglen, A. S. Weyrich, M. T. Rondina, M. Egeblad, J. D. Schiffman, C. C. Yost, Neutrophil extracellular traps contribute to immunothrombosis in COVID-19 acute respiratory distress syndrome. *Blood* **136**, 1169–1179 (2020).
39. A. S. Jureka, C. F. Basler, Propagation and quantification of SARS-CoV-2. *Methods Mol. Biol.* **2452**, 111–129 (2022).
40. J. Schindelin, I. Arganda-Carreras, E. Frise, V. Kaynig, M. Longair, T. Pietzsch, S. Preibisch, C. Rueden, S. Saalfeld, B. Schmid, J. Y. Tinevez, D. J. White, V. Hartenstein, K. Eliceiri, P. Tomancak, A. Cardona, Fiji: An open-source platform for biological-image analysis. *Nat. Methods* **9**, 676–682 (2012).
41. A. E. Carpenter, T. R. Jones, M. R. Lamprecht, C. Clarke, I. H. Kang, O. Friman, D. A. Guertin, J. H. Chang, R. A. Lindquist, J. Moffat, P. Golland, D. M. Sabatini, CellProfiler: Image analysis software for identifying and quantifying cell phenotypes. *Genome Biol.* **7**, R100 (2006).
42. M. Ritchie, B. Phipson, D. Wu, Y. Hu, C. W. Law, W. Shi, G. K. Smyth, limma powers differential expression analyses for RNA-sequencing and microarray studies. *Nucleic Acids Res.* **43**, e47 (2015).
43. C. W. Law, Y. Chen, W. Shi, G. K. Smyth, voom: Precision weights unlock linear model analysis tools for RNA-seq read counts. *Genome Biol.* **15**, R29 (2014).
44. M. D. Robinson, A. Oshlack, A scaling normalization method for differential expression analysis of RNA-seq data. *Genome Biol.* **11**, R25 (2010).
45. Y. Benjamini, Y. Hochberg, Controlling the false discovery rate: A practical and powerful approach to multiple testing. *J. R. Stat. Soc. B. Methodol.* **57**, 289–300 (1995).
46. A. L. Tarca, S. Draghici, P. Khatri, S. S. Hassan, P. Mittal, J. S. Kim, C. J. Kim, J. P. Kusanovic, R. Romero, A novel signaling pathway impact analysis. *Bioinformatics* **25**, 75–82 (2009).

47. U. Raudvere, L. Kolberg, I. Kuzmin, T. Arak, P. Adler, H. Peterson, J. Vilo, g:Profiler: A web server for functional enrichment analysis and conversions of gene lists (2019 update). *Nucleic Acids Res.* **47**, W191–W198 (2019).
48. G. Korotkevich, V. Sukhov, N. Budin, B. Shpak, M. N. Artyomov, A. Sergushichev, Fast gene set enrichment analysis. bioRxiv 060012 [Preprint] (2021). <https://doi.org/10.1101/060012>.
49. M. Aid, K. Busman-Sahay, S. J. Vidal, Z. Maliga, S. Bondoc, C. Starke, M. Terry, C. A. Jacobson, L. Wrijil, S. Ducat, O. R. Brook, A. D. Miller, M. Porto, K. L. Pellegrini, M. Pino, T. N. Hoang, A. Chandrashekar, S. Patel, K. Stephenson, S. E. Bosinger, H. Andersen, M. G. Lewis, J. L. Hecht, P. K. Sorger, A. J. Martinot, J. D. Estes, D. H. Barouch, Vascular disease and thrombosis in SARS-CoV-2-infected rhesus macaques. *Cell* **183**, 1354–1366. e13 (2020).
50. M. Aid, S. J. Vidal, C. Piedra-Mora, S. Ducat, C. N. Chan, S. Bondoc, A. Colarusso, C. E. Starke, M. Nekorchuk, K. Busman-Sahay, J. D. Estes, A. J. Martinot, D. H. Barouch, Ad26.COV2.S prevents upregulation of SARS-CoV-2 induced pathways of inflammation and thrombosis in hamsters and rhesus macaques. *PLoS Pathog.* **18**, e1009990 (2022).
51. L. R. Wong, K. Li, J. Sun, Z. Zhuang, J. Zhao, P. B. McCray Jr., S. Perlman, Sensitization of non-permissive laboratory mice to SARS-CoV-2 with a replication-deficient adenovirus expressing human ACE2. *STAR Protoc.* **1**, 100169 (2020).
52. K. R. Bewley, N. S. Coombes, L. Gagnon, L. McInroy, N. Baker, I. Shaik, J. R. St-Jean, N. St-Amant, K. R. Buttigieg, H. E. Humphries, K. J. Godwin, E. Brunt, L. Allen, S. Leung, P. J. Brown, E. J. Penn, K. Thomas, G. Kulnis, B. Hallis, M. Carroll, S. Funnell, S. Charlton, Quantification of SARS-CoV-2 neutralizing antibody by wild-type plaque reduction neutralization, microneutralization and pseudotyped virus neutralization assays. *Nat. Protoc.* **16**, 3114–3140 (2021).
53. K. H. Dinnon III, S. R. Leist, A. Schäfer, C. E. Edwards, D. R. Martinez, S. A. Montgomery, A. West, B. L. Yount Jr., Y. J. Hou, L. E. Adams, K. L. Gully, A. J. Brown, E. Huang, M. D. Bryant, I. C. Choong, J. S. Glenn, L. E. Gralinski, T. P. Sheahan, R. S. Baric, A mouse-adapted model of SARS-CoV-2 to test COVID-19 countermeasures. *Nature* **586**, 560–566 (2020).
54. G. Dagotto, N. B. Mercado, D. R. Martinez, Y. J. Hou, J. P. Nkolola, R. H. Carnahan, J. E. Crowe Jr., R. S. Baric, D. H. Barouch, Comparison of subgenomic and total RNA in SARS-CoV-2-challenged rhesus macaques. *J. Virol.* **95**, e02370–e02320 (2021).
55. T. Ishige, S. Murata, T. Taniguchi, A. Miyabe, K. Kitamura, K. Kawasaki, M. Nishimura, H. Igari, K. Matsushita, Highly sensitive detection of SARS-CoV-2 RNA by multiplex rRT-PCR for molecular diagnosis of COVID-19 by clinical laboratories. *Clin. Chim. Acta.* **507**, 139–142 (2020).
56. Y. Kumaki, A. M. Salazar, M. K. Wandersee, D. L. Barnard, Prophylactic and therapeutic intranasal administration with an immunomodulator, Hiltonol® (Poly IC:LC), in a lethal SARS-CoV-infected BALB/c mouse model. *Antiviral Res.* **139**, 1–12 (2017).

Acknowledgments: We thank T. Pickett and A. Eakin, NIAID, for access to SARS-CoV-2 animal models through the NIH-ACTIV program; V. Siddharthan (USU), S. O'Connor (Tufts), and

G. Gonzalez (OHSU) for technical assistance; and David Smith (UCSD) for valuable advice. **Funding:** This study was supported by National Institutes of Health grants (R01CA226909, R01CA167426, and R01DE027325 to J.A.V. and R01CA226909 subaward to L.C.M. and R01AI176554 to V.N.); the California Office of the President Emergency COVID-19 Research Seed Funding (R00RG2398 to J.A.V.); the Cowlin Family Foundation (to S.P.P.); Fast Grants, Emergent Ventures, Mercatus Center at George Mason University (to A.J.M.); and Cancer Research Institute/Irvington postdoctoral fellowships (to J.Z. and A.G.). This work was also supported by NIH UL1TR001442 and NIH S10 OD026929 to the UCSD Center for Computational Biology & Bioinformatics Shared Resource and Genomics Center), by NIH P30CA23100 to UCSD Moores Comprehensive Cancer Center, and Department of Health and Human Services Contract HHSN272201700041/75N93021F00002 to J.D.M. **Author contributions:** This study was conceptualized and supervised by J.A.V., L.M.C., A.J.M., V.N., S.P.P., J.D.M., and J.R.T. R.M.S., A.G., I.P., S.R.R., C.B., H.C., M.P., J.R., M.A., S.U., H.S., D.A.D., S.T., C.P.-M., N.C.K., and S.C. performed animal models of ARDS and viral infection, histological and molecular biological experiments, and data analysis. R.M.S., A.D.C., R.S., K.M.F., and J.Z. performed bioinformatic analyses. R.A., B.O.C., and T.A.M. provided IPI-549 for this study. J.H., F.H., S.D., H.R., L.X., X.S., L.E.C.A., J.M.D., M.O., V.P., T.V.S., and D.C. provided tissues from patients with COVID-19 or uninfected, normal tissues. All authors analyzed data and reviewed and approved the manuscript. **Competing interests:** R.A., B.O.C., and T.A.M. were employees of and J.A.V. and A.J.M. were consultants for Infinity Pharmaceuticals. D.A.C. and J.A.V. are shareholders in Impact Biosciences and AlphaBeta Therapeutics. L.E.C.A. is a consultant for Regeneron. V.N. is a consultant for Cellics Therapeutics, I2 Pure Inc., Clarametix BioTherapeutics, logen Inc., Staurus Therapeutics, and Aequor Inc. and received research funding from Micronbrane Inc. and Vaxcyte Inc. A.J.M. was a consultant for HistoWiz Inc. C.B. is currently an employee of, and holds equity in, Akoya Biosciences Inc. J.M.D. is a current employee of Ionis Pharmaceuticals in Carlsbad, CA, and was a consultant for Lexeo Therapeutics. The other authors declare that they have no competing interests. **Data and materials availability:** All data associated with this study are present in the paper or the Supplementary Materials. Data and code are available at DOI 10.5061/dryad.sf7m0cgbm. All raw and processed RNA sequence data are publicly available at Gene Expression Omnibus (GEO) under accession numbers GSE190494, GSE190496, GSE229570, and GSE255211. mHC protocols are available at [dx.doi.org/10.17504/protocols.io.n92ldmmzn15b/v2](https://doi.org/10.17504/protocols.io.n92ldmmzn15b/v2) with custom color deconvolution macro available at DOI 10.5281/zenodo.11287476. IPI-549 was provided to the University of California, San Diego, the Scripps Research Institute, and Tufts University under material transfer agreements and is commercially available. Resources are available upon reasonable request to J.A.V.

Submitted 11 May 2023
Resubmitted 10 February 2024
Accepted 4 June 2024
Published 3 July 2024
10.1126/scitranslmed.adi6887

Supplementary Materials for
**PI3K γ inhibition circumvents inflammation and vascular leak in
SARS-CoV-2 and other infections**

Ryan M. Shepard *et al.*

Corresponding author: Judith A. Varner, jvarner@ucsd.edu

Sci. Transl. Med. **16**, eadi6887 (2024)
DOI: 10.1126/scitranslmed.adi6887

The PDF file includes:

Materials and Methods
Figs. S1 to S14
Tables S1 to S6
References (39–56)

Other Supplementary Material for this manuscript includes the following:

MDAR Reproducibility Checklist

MATERIALS AND METHODS

Reagents

Murine L929 cells (RRID:CVCL_0462, L cell, L-929, derivative of Strain L) were purchased from American Type Culture Collection (ATCC) and maintained in completed Dulbecco's Modified Eagle Medium (DMEM) media supplemented with 10% heat-inactivated fetal bovine serum (FBS) and antibiotics (100 µg/mL penicillin and 100 µg/mL streptomycin). Murine hepatitis virus (MHV)-A59 infectious clone in L929 cells (BEI NR-43000), maSARS-CoV-2 (MA10) infectious clone in Calu-3 cells (BEI NR-55429), and SARS-CoV-2/human/USA/WA-CDC-WA1/2020 (SARS2-WA) were obtained from BEI Resources, NIAID, NIH. SARS-CoV-2/human/USA-WA1/2020 (BEI Resources) was propagated on African green monkey Vero E6 cells as described (39). Formulated IPI-549 and vehicle were provided by Infinity Pharmaceuticals.

Human histopathology

Lung tissue was obtained upon rapid autopsy of recently deceased COVID-19 patients by the Department of Pathology, UCSD, formalin fixed for 48h, and processed into paraffin embedded tissue blocks by the Moores Cancer Center histology shared resource, UCSD. Normal human lung tissue was obtained during lung cancer surgery at the Moores Cancer Center, UCSD and processed into paraffin embedded tissue blocks by the UCSD Department of Pathology. BAL cells from hospitalized COVID-19 positive and COVID-19 negative patients were pelleted, fixed, paraffin embedded and sectioned. Glass slides containing 4-5µm thick tissue sections were deparaffinized and stained with hematoxylin and eosin or Mason's Trichrome by the Moores Cancer Center histology shared resource. Alternatively, slides were deparaffinized, rehydrated, and treated for 20 minutes with Diva Decloaker (901-DV2004X-071017 Biocare Medical) antigen retrieval solution followed by treatment with endogenous peroxidase blocking and incubation with 5% normal horse serum for 1h. Slides were then incubated with 1:200 mouse anti-human CD68 (RRID:AB_2074844 clone PG-M1, Dako/Agilent), 1:400 rabbit anti-PI3 Kinase-gamma (RRID:AB_1904087 Cell Signaling Technology, Inc., clone D55D5, #5405), or 1:200 rabbit anti-Myeloperoxidase (RRID:AB_2864724 ab208670, Abcam). Following primary antibody incubation, slides were washed in Tris buffered saline containing Tween 20 (TBST) and incubated with ImmPRESS HRP horse anti-mouse IgG Plus kit (MP-7802-15 Vector Labs) or ImmPRESS HRP horse anti-rabbit IgG Plus kit (MP-7801-15 Vector Labs) according to manufacturer's instructions for 30 minutes at room temperature, washed in TBST, incubated in 3,3'-diaminobenzidine (DAB) substrate for up to 5 minutes, water-washed for 5 minutes and counterstained for 1 minute with hematoxylin. Slides were mounted with Cytoseal permanent mounting medium (Richard-Allan Scientific Cat #8310-4). Biomarker quantification was performed using QPath open-source digital image analysis software.

Multiplex IHC

Sequential IHC was performed on 5 µm FFPE sections using an adapted protocol based on methodology previously described (20). Briefly, slides were deparaffinized and stained with hematoxylin (S3301, Dako), followed by whole-slide scanning at 20X magnification on an Aperio AT2 (Leica Biosystems). Tissues then underwent 20 minutes heat-mediated antigen retrieval in pH 6.0 Citra solution (BioGenex), followed by 10 minutes endogenous peroxidase blocking in Dako Dual Endogenous Enzyme Block (S2003, Dako), then 10 minutes protein blocking with 5% normal goat serum and 2.5% bovine serum albumin (BSA) in TBST. Primary antibody conditions are listed in table S1. Following primary antibody incubation, slides were washed in TBST, and incubated with either anti-rat, anti-mouse, or anti-rabbit Histofine Simple Stain MAX PO HRP-conjugated polymer (RRID:AB_2811178 Biosciences) for 30 minutes at room temperature, followed by AEC chromogen (RRID:AB_2336076 Vector Laboratories). Slides were digitally scanned following each chromogen development, then AEC was removed with 100% EtOH. Between rounds, peroxidase blocking with Dako Dual Endogenous Enzyme Block was performed for 10 minutes at room temperature to inactivate HRP enzyme still present on the secondary antibody of the previous round. Another primary produced in a distinct species could be utilized within the same staining cycle. Between cycles, citrate antigen retrieval was completed as described above to remove all primary antibodies primary-secondary antibody complexes.

Following iterative staining, computational image processes and analysis was performed. Scanned images were registered in MATLAB version R2018b using the SURF algorithm in the Computer Vision Toolbox (The MathWorks, Inc.). Image processing and cell quantification were performed using FIJI (FIJI Is Just ImageJ) (40). AEC signal was extracted for quantification and visualization in FIJI. The FIJI plugin Color_Deconvolution [H AEC] was used to separate hematoxylin, followed by postprocessing steps for signal cleaning and background elimination as described (dx.doi.org/10.17504/protocols.io.n92ldmmzn15b/v2). AEC signal was extracted in FIJI using with the NIH plugin RGB_to_CMYK. Color deconvoluted images were processed in CellProfiler Version 3.5.1 (41) using custom macro deposited at doi: 10.5281/zenodo.11287476 to quantify single cell mean intensity signal measurements for every stained marker. FCS Express 6 Image Cytometry RUO (De Novo Software) was used to perform hierarchical gating and cell classification based on expression of known markers as shown in fig. S1. For visualization, signal-extracted images were overlaid and pseudocolored in FIJI.

TempoSeq FFPE tissue RNA Sequencing

Two five-micron FFPE sections from each of twelve postmortem lung specimens from COVID-19 patients, five normal lung specimens, eight BAL specimens from COVID-19 patients, and five BAL specimens from normal patients were used to perform TempoSeq (Templated Oligo assay with Sequencing readout) FFPE human whole transcriptome RNA sequencing at BioSpyder Technologies, Inc, as previously described (27, 28). Of these, one upper lung and one lower lung specimens from each of two patients were included in initial analysis. Two 5 FFPE tissue sections per sample were scraped from glass slides, paraffin removed, and at least two 25-nucleotide long oligonucleotides specific for 19,283 genes (21,111 probes) were used to prepare full-length (50-nucleotide-long) probes that were amplified prior to sequencing library preparation. Prepared libraries were sequenced on an Illumina HiSeq2500; mapped reads were generated by TempO-SeqR alignment of demultiplexed FASTQ files using Bowtie, allowing for up to 2 mismatches in the 50-nucleotide target sequence.

RNA sequencing analysis

Unnormalized read counts were obtained from BioSpyder TempO-seq. The R BioConductor packages edgeR (30) and limma (42) were used to implement the limma-voom (43) method for differential expression analysis. We analyzed normal lung and COVID-19 lung sample groups together. We also analyzed COVID-19 BAL and normal BAL together. One COVID-19 BAL sample was removed from downstream analysis because it had <300,000 quantified reads. Lowly expressed genes, those not having counts per million (cpm) ≥ 10 in at least 10 of the samples, were filtered out in the combined analysis and for lung samples only a less stringent filter of (cpm) ≥ 1 in at least 5 of the samples was applied. Trimmed mean of M-values (TMM) normalization (44) was applied after filtering. The experimental design was modeled upon condition, called condition ($\sim 0 +$ condition). The voom method was employed to model the mean-variance relationship, after which lmFit was used to fit per-gene linear models and empirical Bayes moderation was applied with the eBayes function. Significance was defined by using an adjusted p-value cut-off of <0.05 after multiple testing correction (45) using a moderated t-statistic in limma. Functional enrichment of the differentially expressed genes was performed using SPIA (46), gProfiler (47) and fGSEA (48). R version 4.2.2 was used for plotting.

Cell type deconvolution was performed using the log-normal regression algorithm of Danaher *et al.* (29) and its implementation in Bioconductor (30). Inputs were the normalized expression values (cpm), the background matrix of background values set to a value of 6, and the training matrix containing log₂ expression values in the training set, which is part of the R package and named “Human_Cell_Landscape”. The training matrix originally contained 102 human cell types, but we excluded non-specific cell types not expected to be in these tissues, such as glial cells, kidney cells, etc. A total of 56 cell types for the lung tissue remained. Normalized gene counts for select genes were graphed in Prism (GraphPad); statistical analysis was performed across all genes with limma-voom using log fold change (FC) and adjusted p value from the limma-voom analysis.

GeoMx Digital Spatial Profiling (DSP)

nanoString GeoMx digital spatial profiling was applied to COVID-19 and normal lung tissues to acquire spatially resolved, quantitative measurements of gene expression in human lung macrophages, granulocytes, and epithelium in FFPE tissue sections. Three cases of post-mortem COVID lung tissues and one case of surgically resected normal lung tissue were sectioned, deparaffinized, rehydrated and treated with low pH retrieval solution. nanoString GeoMX Digital Spatial ImmuneOncology and COVID-19 RNA probes were hybridized to sections overnight. Sections were then stained with a cocktail of immunofluorescent antibodies comprised of Alexa fluor 532-labeled anti-CD68 (RRID: AB_2074852 Clone KP1, 1:100, Novus Biologicals), Alexa fluor 647-labeled Myeloperoxidase (RRID: AB_964678 Clone 2C7, 1:500, Novus Biologicals), Alexa fluor 594 labelled anti-PanCytokeratin (AE-1, AE-3, Novus Biologicals, NBP2-33200AF594) and SYTO13 Nuclear stain (S7575 ThermoFisher Scientific). Digital scanning of slides was performed on the GeoMX Digital Profiler (nanoString Technologies, Inc.). Regions of Interest (ROI) and cell type with a spatial resolution of approximately 10 mm were selected, exposed to UV light for RNA probe cleavage and oligonucleotide collection. Samples were sequenced on a NovaSeq6000. Counts from barcodes corresponding to RNA probes were normalized with internal positive and negative controls and then normalized to ROI area.

DSP RNA sequence analysis

Data were pre-processed in nanoString DSP Software v 2.2.0.123 with Q3 normalization. ROIs were classified according to predominant cell type (epithelium, granulocyte, macrophage) in one of two conditions (COVID-19 positive and normal). The R BioConductor packages edgeR (30) and limma (42) were used to implement the limma-voom (43) method for differential expression analysis within and across cell types and condition. Trimmed mean of M-values (44) normalization was applied. The experimental design was modeled upon cell type and condition (~0 + cell Type_condition). The voom method was employed to model the mean-variance relationship, after which lmFit was used to fit per-gene linear models and empirical Bayes moderation was applied with the eBayes function. Significance was defined by using an adjusted p-value cut-off of <0.05 after multiple testing correction (45) using a moderated t-statistic in limma.

Hamster SARS-CoV-2 model

Hamster viral infection: Six- to seven-week-old Golden (Syrian) Hamsters (Envigo; weight range 90-110g, equal number of male and females) were inoculated with SARS-CoV-2 intranasally with 1×10^5 TCID₅₀ (Median Tissue Culture Infectious Dose) in 100µl volume as described (49, 50). The viral isolate USA-WA1/2020 (BEI Resources) was propagated on Vero E6 cells and clarified by centrifugation. Uninfected hamsters were sham inoculated with phosphate buffered saline (PBS) intranasally. Hamsters were evaluated daily for changes in bodyweight, temperature, and demeanor or clinical signs of disease. Hamsters were euthanized at 2-, 4-, and 7-days post infection (dpi). Lung tissue was collected at necropsy and fixed in 10% neutral buffered formalin for 24 hours before being transferred to 70% ethanol. For PI3Kγ inhibition studies, hamsters were administered 30 mg/kg IPI-549 or vehicle alone (n=4 per group) by orogastric gavage on days 0, 1, 2, and 3 following challenge and body weight monitored daily. Hamsters were euthanized at 2, 4, 7 and 14 dpi. Lung tissue was collected at necropsy and fixed in 10% neutral buffered formalin for 24 hours before being transferred to 70% ethanol.

Hamster SARS-CoV-2 model histopathology and immunohistochemistry: At time of fixation, lungs were suffused with 10% formalin to expand the alveoli. All tissues were fixed in 10% formalin and blocks sectioned at 5 µm. Slides were baked for 30-60 minutes at 65° C then deparaffinized in xylene and rehydrated through a series of graded ethanol to distilled water. Heat induced epitope retrieval (HIER) was performed using a pressure cooker on steam setting for 25 minutes in citrate buffer (ThermoFisher Scientific, AP-9003-500) followed by treatment with 3% hydrogen peroxide. Slides were then rinsed in distilled water and protein blocked (BioCare, BE965H) for 15 minutes followed by rinses in phosphate buffered saline (PBS). Mouse anti-SARS-CoV-2 nucleocapsid antibody (RRID:AB_2827977 Sino biological; 40143-MM05) diluted 1:1000, rabbit anti-

myeloperoxidase (RRID:AB_2335676 Dako-Agilent; A0398) diluted 1:1000, or rabbit anti-Iba-1 antibody (RRID:AB_839504 Dako; 019-19741) diluted 1:4000 followed by rabbit Mach-2 HRP-Polymer (BioCare; RHRP520L) were incubated for 30 minutes then counterstained with hematoxylin followed by bluing using 0.25% ammonia water. Labeling was performed on a Biocare IntelliPATH autostainer. All antibodies were incubated for 60 min at room temperature. Tissue pathology was assessed independently by two board-certified veterinary pathologists blinded as to treatment conditions.

Hamster SARS-CoV-2 RNAscope: RNAscope in situ hybridization as directed with the following modifications using a custom probe for hamster PI3K γ (ACD Cat. No. 1071581-C1 and DapB (ACD Cat.No 310043) as a negative control. In brief, after slides were deparaffinized in xylene and rehydrated through a series of graded ethanol to distilled water, retrieval was performed for 30 min in ACD P2 retrieval buffer (ACD Cat. No. 322000) at 95-98°C, followed by treatment with protease III (ACD Cat. No. 322337) diluted 1:10 in PBS for 20 minutes at 40°C. Slides were then incubated with 3% H₂O₂ in PBS for 10 minutes at room temperature. All washes were performed in 0.5x kit provided SSC. Slides were developed using the RNAscope 2.5 HD Detection Reagents-RED (ACD Cat. No.322360).

Hamster SARS-CoV2 Quantitative Image Analysis: Quantitative image analysis was performed using HALO software (v3.0.311.405; Indica Labs) on at least one lung lobe cross-section from each animal as described (49, 50). In cases where more than one cross-section was available, all lung lobes were quantified as an individual data point. For PI3K γ , the whole slide digital images were deconvoluted using the Indica Labs – Deconvolution algorithm (v1.1.1). The deconvoluted images were analyzed with Indica Labs – FISH-IF (v2.1.5) algorithm to determine the PI3K γ copies per mm² total tissue area. For Iba-1, the Indica Labs - Multiplex IHC algorithm (v3.1.4) was used for quantitation. In all instances, manual inspection of all images was performed on each sample to ensure that the annotations were accurate.

Mouse SARS-CoV-2 models

SARS-CoV-2 viral infection in hACE2 transgenic mice: 8-week-old K18-hACE2 C57Bl/6 male mice (Jackson Laboratories) were intranasally (i.n.) infected with 5000 Plaque Forming Units (pfu) of SARS-CoV-2/human/USA/WA-CDC-WA1/2020. At 0- or 2-days post-infection (dpi), mice were treated with either vehicle or 25mg/kg IPI-549 once daily by oral gavage (n=5 or 10 per study). Weight loss was monitored at 0, 3, 4 and 5 dpi. Lungs were collected at 5 dpi and stored in z-Fix for histological analysis or in Trizol (Thermo Fisher Scientific, 15596018) for RNA-sequencing. Some lungs were dissociated and processed for flow cytometry and virus detection by focus-forming assay. SARS-CoV-2 viral infection in hACE2 transgenic mice was performed 6 times.

SARS-CoV-2 Focus-Forming Assay

Viral titer was determined using a focus-forming assay protocol adapted from previous publications (51,52). In short, Vero E6 cells were seeded at 2.5×10^4 cells/well in a flat-bottom 96-well plate in culture media containing DMEM supplemented with 10% FBS and 1% Pen-Strep. The following day, lungs were collected from the vehicle and IP-549 treated mice on day 5 post-infection. Lungs were weighted and bead-homogenized in 1 ml infection media containing DMEM supplemented with 2% FBS and 1% Pen-Strep. In a U-bottom 96-well plate, lung homogenates were serially 10-fold diluted in infection media. Culture media was aspirated completely from Vero E6 cells and 100 μ l diluted samples were transferred to each well of Vero cells. The plate was incubated at 37°C for 1 hr before 100 μ l of pre-warmed 1.6% methylcellulose was added to each well. Plate was incubated for another 24hr at 37°C and fixed with 4% PFA for 30min at RT. Fixative was removed and plate was washed with PBS before staining with 50 μ l/well of anti-spike rabbit polyclonal antibody (Sino Biologicals, 40592-T62, 1:1000) in PBS containing 0.2% Triton X-100 and 1% BSA at RT°C for 1 hr. Primary antibody was discarded and plate was washed 3 times with PBS containing 1%Tween (PBST). 50 μ l/well anti-rabbit IgG goat-horseradish

peroxidase conjugate in PBS containing 0.2% Triton X-100 and 1% BSA was added (Invitrogen, G21234, 1:5000) and plate was incubated at RT for 1 hr. Secondary antibody was discarded, and plate was washed 3 times with PBST before 50 µl/well TrueBlue substrate was added (SeraCare KPL, 5510-0050). The plate was incubated for 10min at RT and washed once with PBST. Residue liquid was completely removed from the plate and foci were counted using an ELISPOT reader (CTL-Immunospot S6 Universal analyzer). Viral titer is calculated in focus-forming units per gram of tissue (FFU/gram of tissue): $FFU/g = (\text{foci/well}) \times (\text{dilution factor}) / \text{gram of tissue}$.

Flow cytometry for SARS-CoV-2-infected hACE2 transgenic mice: Lungs were collected from vehicle and IPI-549 treated mice on day 5 post-infection. Lungs were minced with scissors and incubated in 10 ml digestion buffer containing RPMI-1640 supplemented with 10% FBS, 10 mg collagenase (C-5138, Sigma) and 100 µg DNase I (10104159001, Roache). Cell suspension was placed on a shaker at 37°C for 45 minutes and tissue was subsequently dissociated through 70 µm cell strainer. Red blood cells were lysed with ACK lysing buffer (118156101, Quality Biological Inc.) for 2 minutes and washed once with PBS. Single-cell suspensions were incubated with 50 µl/sample PBS containing 1:1000 Ghost Dye Violet 510 (SKU 13-0870-T100, Cytex) and 1:50 TruStain FcX (101320, BioLegend) for 30 minutes at 4°C. Cells were then washed once with 200µl/sample PBS before surface staining with 50µl/sample antibody cocktail containing anti-CD11b BUV563 (RRID: AB_312788, M1/70, BioLegend), anti-mouse-CD11c APC-Cy7 (RRID: AB_313772, N418, BioLegend), anti-mouse CD170/SiglecF BV421 (RRID: AB_2750234, S17007L, BioLegend), anti-mouse CD206/MMR (RRID: AB_10918434 C068C2, BioLegend), anti-mouse F4/80 PerCP-Cy5.5 (RRID: AB_893499 BM8, BioLegend) anti-mouse CD90.2/Thy1.2 (RRID: AB_313175, 30-H12, BioLegend), anti-mouse Ly-6G BV650 (RRID: AB_2563207, 1A8, BioLegend), anti-mouse CD64 BV711 (X54-5/7.1, BioLegend), anti-mouse/human CD44 (RRID: AB_2566557, IM7, BD Bioscience) anti-mouse Ly-6C APC-A (RRID: AB_10640820 HK1.4, BioLegend), anti-mouse NK-1.1 (RRID: AB_493184, PK136, BD Bioscience), anti-mouse CD45 Alexa Fluor 700 (RRID: AB_394611, BD Bioscience, 30-F11), anti-mouse CD19 BUV737 (RRID: AB_2716855, 1D3, BD Bioscience), anti-mouse CD8a BUV395 (RRID: AB_1080575053-6.7, BD Bioscience), and anti-TCRB PE-Cy7 (RRID: AB_893627, H57-597, BioLegend) at 1:200 for 1 hr at 4°C. Cells were washed with PBS once, followed by 4% paraformaldehyde fixation for 30 minutes at 4°C. Flow cytometry was performed on a Cytex Aurora with 5 lasers. Data analysis was performed using FlowJo (BD Biosciences).

Mouse-adapted SARS-CoV-2 viral infection: maSARS-CoV-2 (MA10 variant, infectious clone in Calu-3 cells, BEI NR-55429) (53) was prepared based on a stock titer = 1.97×10^4 pfu/ml. Female BALB/c mice 270 to 300 days old were ear-tagged, randomized to groups, and infected with 1×10^3 pfu/mouse SARS-CoV-2 in 90 µl of Modified Eagle's Medium (MEM) or sham-infected by intranasal instillation at the Antiviral Institute of Utah State University. Within less than an hour at day 0, mice were administered by oral gavage vehicle (n=10) or 15mg/kg IPI-549 in a volume of 0.1 ml/25 g-mouse from day 0-4 (or until death, n=20). Another cohort was treated on day 2-4 (or until death, n=20) in the same manner. After morning treatments on day 2, 5 animals treated with vehicle and 10 animals treated with IPI-549 from 0-2 dpi were necropsied. Individual whole-body weights and survival were monitored for up to 6 days. Remaining animals were monitored until death or day 6. Serum samples and lung tissues were collected from mice necropsied on day 2 and on day 6. No tissue was collected from mice that died between day 2 and 6.

Mouse-adapted SARS-CoV-2 tissue processing: Serum samples and lungs were collected from IPI-549 and vehicle-treated maSARS-CoV-2 infected groups on days 2 and 6, respectively. Blood samples were collected by cardiac puncture, clotted, centrifuged to collect serum, heat-inactivated at 65°C for 45 minutes to inactivate virus, and stored frozen. On day 2 or 6, the left lung lobe was perfused with 10% buffered formalin for H&E staining and analysis. A 22-g blunt-ended needle was inserted in the trachea to gently fill the lung with fixative. The tissues were immersed in formalin overnight at refrigeration temperature before removing from the BSL3 lab, embedding, sectioning and scoring pathology. The right lung was weighed, bead-homogenized in 0.3 ml MEM

and two aliquots of 0.1 ml of homogenate added to 1 ml Trizol prepared and frozen until processing for RNA extraction. The remaining homogenized lung volume was used for SARS-CoV-2 viral load assay using 50% cell-culture infectious doses (CCID₅₀) readout (the terminologies TCID₅₀ and CCID₅₀ are interchangeable). RNA was extracted using the standard Trizol method. The pellet was dissolved in 0.1 mL of RNase-free water. Total extracted RNA was quantified using a Nanodrop spectrophotometer so that 300 ng could be added for each RT-PCR reaction.

Mouse SARS-CoV2 RT-PCR: Two different primer/probe sets were used for purposes of comparison, one to detect genomic viral RNA (gRNA), and another to detect subgenomic viral RNA (sgRNA). The sgPCRs measure any one of viral replication products (S, 3a, E, M, 6, 7a, 7b, 8 and N). Any PCR product amplified from a subgenomic coding sequences is present in both the genomic and subgenomic sequences. Therefore, the approach to distinguish sgRNA from gRNA is to amplify a PCR product in both the 5' UTR leader sequence and within specific subgenomic sequence. Validated primer/probe sets in the leader and E sequences (54,55) were used: Forward primer (leader sequence): CGATCTCTTGTAGATCTGTTCTC Reverse primer (E sgRNA): ATATTGCAGCAGTACGCACACA Probe: (5'FAM)/ACACTAGCCATCCTTACTGCGCTTCG/(3'BHQ-2).

Genomic viral RNA does not specifically reflect replicating virus. The primer/probe set was developed at Utah State University from a prototypic SARS-CoV-2 sequence, SARS-CoV-2/human/USA/WA-CDC-WA1/2020, in the ORF1ab sequence (accession MN985325.10). This sequence is only present in gRNA, not sgRNA. Forward primer: CACTAGTGCCACAAGAGCAC Reverse primer: TGCGAGCAGAAGGGTAGTAG Probe: (5'FAM)/TCCAGGGACCACCTGGTACTGGT/(3'BHQ-2). Each sample was run in duplicate using the Probe No-ROX One-step kit. The Magnetic Induction Cycler was programmed at 10 minutes at 45°C, 2 minutes at 95°C, then 40 cycles of 5 seconds at 95°C and 20 seconds at 60°C. A standard curve consisted of 1-log₁₀ serial dilutions of a positive sample. The C(t) values of experimental samples were interpolated from the standard curve to obtain the relative copy number. The values are reported as relative copy number per 300 ng total RNA added to the RT-PCR reaction.

Mouse SARS-CoV-2 infectious virus assay: A published assay to quantify infectious virus was used with some modification (39). Confluent or near-confluent Vero E6 monolayers were prepared in 96-well disposable microplates the day before testing. Cells were maintained in MEM supplemented with FBS as required for each cell line. For antiviral assays, the same medium was used but with FBS reduced to 2% or less and supplemented with 50 µg/ml of gentamicin. The lung tissue of each animal lung was homogenized in MEM supplemented with 10% FBS using a bead-homogenizer, and the tissue fragments were allowed to settle. Growth media was removed from the cells and the tissue homogenate was applied in 0.1 ml volume to wells at 2X concentration. Plates were incubated at 37°C with 5% CO₂ until >80% cytopathic effect (CPE) was observed in virus control wells. The plates were then stained with 0.01% neutral red for approximately two hours at 37°C in a 5% CO₂ incubator. The neutral red medium was removed by complete aspiration, and the cells were rinsed once with PBS to remove residual dye. The PBS was completely removed, and the incorporated neutral red was eluted with 50% Sorensen's citrate buffer/50% ethanol for at least 30 minutes. Neutral red dye penetrates into living cells, thus, the more intense the red color, the larger the number of viable cells present in the wells. The dye content in each well is quantified using a spectrophotometer at 540 nm wavelength. The dye content in each set of wells is converted to a percentage of dye present in untreated control wells using a spreadsheet and normalized based on the virus control. The data are reported as CCID₅₀ per gram tissue.

Mouse SARS-CoV-2 RNA sequencing and analysis: RNA sequencing libraries were prepared in two batches from ribodepleted RNA extracted from lung tissue of animals enrolled in the murine SARS-CoV-2 studies described above. Libraries were sequenced at the University of California San Diego Institute for Genomic Medicine, Genomics Center utilizing an Illumina NovaSeq 6000. Quality trimming of FASTQ files was performed using Trimmomatic (v0.36). Paired-end reads were aligned to the mouse reference genome (GRCm39;

annotation file, vM29) using STAR (v2.5.3a), followed by RSEM (v1.3.0) to quantify expression of transcripts. The R BioConductor package DESeq2 was used to perform differential gene expression analysis from unnormalized counts. Lowly expressed genes, defined as those genes with mean <10 reads across all samples, were excluded prior to differential expression analysis. Plots represent the regularized log transformed (rlog) read counts. Sample clustering is supervised or unsupervised (Pearson correlation) where indicated. Significance was defined by using an adjusted p-value cut-off of <0.05 after multiple testing correction. Completely differentially expressed genes or genes differentially expressed in multiple group comparisons were extracted for gene annotation and functional enrichment analysis using GSEA.

Cell type enrichment scores in mouse RNA sequencing samples were determined from the expression frequency of cell type markers from PanglaoDB (38), a single cell sequencing resource for gene expression data collected and integrated from multiple studies. The reference matrix originally contained 178 cell types, but the data were filtered for cells of lung and immune origin. A total of 32 cell types remained. Only genes specific to mouse were included in the analysis. Cell type enrichment scores were calculated using the standard formula (nN/kM), where N is the total number of genes in the library, k is the number of genes in a specific cell type reference list, M is the number of differentially upregulated or downregulated genes, and n is the number of genes in both k and M. Significance was calculated using a Fisher's exact test and plotted as minus \log_{10} p-value.

Murine hepatitis virus A59 strain (MHV-A59) infection

MHV-A59 viral infection: 8-week-old male C57BL/6 mice (n=15 per group) were inoculated intranasally with 7.5×10^5 pfu MHV-A59 in 24 μ l of 0.9% sterile saline or sham inoculated with 24 μ l of 0.9% sterile saline. 15mg/kg IPI-549 or 0.1 ml of vehicle was administered p.o. Body weight and survival were monitored daily. At 2-, 5-, and 8-days post-infection, 5 mice from each treatment group and 3 mice from the sham infection group were euthanized, then lungs were excised and rinsed in ice-cold PBS. 100mg of lung tissue was homogenized in cold DMEM with 10% FBS for measurement of viral load by plaque assays, 100mg was homogenized in Trizol for RNA extraction, and the remaining tissue was preserved in 5ml of 10% Zinc Formalin for 24-48h, paraffin embedded and used for histological analysis. Blood was collected in 1.5ml Eppendorf tubes, allowed to clot, and serum was collected for cytokine and chemokine analysis. MHV infection studies were performed 3 times.

MHV loads by plaque assay: To quantify MHV viral load in lung tissue, lung homogenates were rapidly frozen and thawed three times. After centrifugation at 770 x g at 4°C for 10 minutes, supernatants were collected and used to assay virus content using L929 fibroblasts monolayer on 6 well plates. 200 μ l of the lung homogenate was added to triplicate wells and plates were incubated at 37°C in a 5% CO₂ incubator for 1 hr, rocking every 10 mins. At the end of incubation, 2ml of 0.8% agarose was overlaid onto to each well. The plates were incubated for two days until the formation of virus plaques and the plaques of each well were manually counted.

MHV model RT-PCR: Total RNA was extracted from 100 mg tissue with TRIzol reagent (Invitrogen), and 1 μ g RNA that was pretreated with 1 U of RQ1 RNase-free DNase (ThermoFisher Scientific) to remove DNA contamination at 37 °C for 30 minutes, were used for reverse transcription with oligo-dT primer (Bio-Rad). Quantitative PCR reactions were then performed using primers to detect the MHV-A59 N gene (MHV N gene Forward CAGATCCTTGATGATGGCGTAGT Reverse AGAGTGTCCATCCCGACTTTCTC) using the gene for ribosomal protein L32 as a normalization control. PCR products (123 bp) were also resolved by electrophoresis in 2% agarose gels and visualized on the iBright FL1000 System machine (Invitrogen). Total RNA was extracted using Trizol (Invitrogen) from approximately 100mg of lung tissues). Relative expression of each gene was normalized to those of the housekeeping gene *Gapdh*. Quantitect primer sets used were: *Il1b* Mm_Il1b_2_SG, *Tnfa* Mm_Tnf_1_SG, *Il6* Mm_Il6_1_SG, *Cxcl10* Mm_Cxcl10_1_SG, *Il10* Mm_Il10_1_SG, *Il12* Mm_Il12b_1_SG, *Ifng* Mm>Ifng_1_SG, *Ifna* Mm>Ifna2_1_SG, *Ifnb* Mm>Ifnb1_1_SG, *Gbp5*

Mm_Gbp5_1_SG, *Gbp3* Mm_Gbp3_1_SG, *Stat1* Mm_Stat1_1_SG, *Cd8* Mm_Cd8a_1_SG, *Cd4* Mm_Cd4_1_SG, *Ccl2* Mm_Ccl2_1_SG, *Gzmb* Mm_Gzmb_1_SG, and *Gapdh* Mm_Gapdh_3_SG (Qiagen).

MHV Cytokine analysis: Cytokine concentrations in 25µl murine serum and BALF were determined using ProcartaPlex mouse cytokine panels (EPXR260-26088-901, EPX110-20820-901 and PPX-11-MXCE49Z) according to manufacturer's directions on a Luminex Magpix instrument (ThermoFisher Scientific). Murine cytokine enzyme-linked immunosorbent assays (ELISAs) were performed using uncoated ELISA kits (Invitrogen/Thermo Fisher Scientific): TNF- α (RRID:AB_2575076 #88-7324-22), IL-6 (RRID:AB_2574986 #88-7064-22), and IL-1 (RRID:AB_2574942 #88-7013-22), all according to manufacturer's directions.

MRSA and *E. coli* K1 strain RS218 infection models

Bacterial Strains: Methicillin-resistant *Staphylococcus aureus* strain USA300/TCH1516 (MRSA) (ATCC BAA-1717) and *E. coli* K1 strain RS218 were used in the study. MRSA was propagated in Todd Hewitt broth (THB) and *E. coli* grown in Luria-Bertani broth (LB), shaking at 37°C to mid-log phase. Bacteria were collected by centrifugation at 4000 RPM for 10 min, washed once with PBS, and resuspended in PBS (mouse infections) or RPMI-1640 (macrophage killing assays).

MRSA animals. Animal studies were conducted under protocols approved by the UC San Diego Institutional Animal Care and Use Committee (IACUC). For systemic infection, 8- to 12-week-old wild type (WT) and *Pik3cg*^{-/-} (p110 γ knockout, KO) mice on the C57Bl/6 background were injected with 2x10⁸ colony forming units (CFU) MRSA or 1x10⁷ CFU *E. coli* intraperitoneally (i.p). Survival of infected mice was monitored every 8 h for 6 days. For CFU enumeration experiments, mice were infected with 2.7 x10⁸ CFU MRSA i.p. and euthanized 24 h after infection, Liver, kidney, and spleen were harvested and dilution plated on THB agar plates. Serum was also collected at this timepoint for measurement of cytokines IL-6 and IL-1 β using ELISA kits M6000B and MLB00C (R&D Systems).

L929 conditioning media. To prepare L929 conditioned media, confluent L929 cells were detached, collected, and passaged 1:10. Cells were then cultured for 7 to 8 days until the media was exhausted. The conditioned media, which contains macrophage growth factor M-CSF, was filtered (0.22 µm) and stored at -20 °C until use.

Murine bone marrow derived macrophages (BMDM) and bacterial killing assay. BMDM were generated by flushing bone marrow cells from femurs and tibia of wild type (WT) and *Pik3cg*^{-/-} C57Bl/6 mice and resuspending the collected cells in RPMI-1640 supplemented with 20% L929 conditioned media. On day 7 of culture, cells were washed, detached with 0.025% trypsin-EDTA, and were seeded on 96-well plates for 48 h before used for bacterial killing assays. Bacteria were added to cultured macrophages in 96-well plates at a multiplicity of infection (MOI) of 0.1 (10,000 CFU bacteria per 100,000 macrophages). After centrifugation at 1200 rpm for 5 min to initiate contact between macrophages and bacteria, the plates were incubated in 37°C, 5% CO₂ for 1 h. Macrophages were then lysed by 0.1% Triton-X and the lysed samples serially diluted and spot-plated onto THB agar plates for CFU enumeration.

Animal models of inflammation

Peritoneal inflammation: WT and *Pik3cg*^{-/-} mice were i.p. injected with 100 µl of a 3% thioglycolate (Sigma) solution. Peritoneal cells and fluids were collected 96 hours later from the peritoneal cavity into 10 ml of PBS. Macrophage enrichment was performed by plating cells in RPMI-1640 with 10% FBS and 1% penicillin/streptomycin for 2 h at 37 °C and 5% CO₂. After 2 h, non-adherent cells were removed with three PBS washes, adherent cells were released from plates with trypsin-EDTA and washed and resuspended in 5% BSA in PBS. 1x10⁶ cells per condition were incubated with 1:1000 Aqua Live Dead fixable stain (L34957 ThermoFisher),

and then with 1:500 Fc-blocking reagent (553141 BD Biosciences) for 10 minutes on ice followed by incubation with fluorescently labeled antibodies on ice for 0 minutes. Cells were stained with 2.5 µg/ml anti-CD45 (30-F11, RRID:AB_1210805), 5.0µg/ml anti-CD11b (M1/70, RRID:AB_469901), and 5.0 µg/ml anti-F4/80 (BM8, RRID:AB_469653) (ThermoFisher) for 1h, washed with PBS and fixed in stabilizing fixative (3380360 Becton Dickinson) 5 minutes and analyzed on a FACS ARIA II flow cytometer (Becton Dickinson). All data analysis was performed using the flow cytometry analysis program FlowJo (Becton Dickinson).

ARDS Animal models: Inflammatory acute respiratory distress syndrome (ARDS) was modeled in animals by systemic or local administration of lipopolysaccharide (LPS) or poly-inosine:cytosine (polyI:C) (56). To model acute inflammation, n=5-10 WT or *Pik3cg*^{-/-} mice were inoculated by i.p. injection with a single dose of 10 mg/kg LPS (L4391, Sigma-Aldrich, Inc.) or 12 mg/kg polyI:C (PCL-40-03, Invivogen, Inc.). In studies evaluating the effect of PI3K γ inhibitor IPI-549, mice were pre-treated once daily for 2 days with 100µl of Vehicle or IPI-549 (15mg/kg) by oral gavage prior to LPS or polyI:C inoculation. Animals were euthanized 24h later. All studies were performed three or more times with n= 5-10 mice per group. To model chronic inflammation, WT or *Pik3cg*^{-/-} mice were inoculated with doses of 3 mg/kg LPS or 12 mg/kg polyI:C by intraperitoneal injection on three consecutive days. Some WT animals were pre-treated with 100µl of Vehicle or IPI-549 (15mg/kg) by oral gavage (n=5-10) for 1-2 days prior to LPS or poly I:C inoculation and once daily after inoculation for 3 days. Animals were euthanized 24hr after the last treatments. All studies were performed three or more times. In some animals, 5 mg/kg Poly I:C or LPS in 20 µl was administered once daily for three days by intranasal inoculation and animals were treated as described above. All studies were performed three or more times with n= 5-10/group.

ARDS Histopathology: To collect lung tissues from mice for histopathology, mice were euthanized, and lungs were immediately inflated by intratracheal administration of up to 1ml 10% zinc formalin, followed by immersion in 10% zinc formalin for 24-48h. Lungs were paraffin-embedded and sectioned at the UCSD Moores Cancer Center histology shared resource. Glass slides containing 5µm thick tissue sections were deparaffinized and stained with hematoxylin and eosin or Mason's Trichrome by the Moores Cancer Center histology shared resource. Alternatively, slides were deparaffinized, rehydrated, treated with Diva Decloaker (Biocare Medical) antigen retrieval solution followed by endogenous peroxidase blocking, and then incubated with 5% normal horse serum for 1 hour. Slides were then incubated with 1:250 anti-F4/80 (RRID:AB_467558 14-4801-82, ThermoFisher Scientific) or 1:200 anti-MPO (RRID:AB_2864724 ab208670, Abcam) at 4°C overnight. Following primary antibody incubation, slides were washed in TBST, and incubated with goat anti-rat or horse anti-goat HRP-conjugated polymer according to manufacturer's instructions (MP-7444-15 ImmPRESS HRP Goat Anti-Rat IgG, Mouse adsorbed Polymer Detection Kit, Peroxidase or MP-7405 ImmPRESS HRP Horse Anti-Goat IgG Polymer Detection Kit, Peroxidase, Vector Laboratories) for 30 minutes at room temperature, washed in TBST, incubated in 3,3'-diaminobenzidine (DAB) substrate for up to 5 minutes, water washed for 5 minutes and counterstained for 1 minute with hematoxylin. Slides were mounted with Cytoseal permanent mounting medium (Richard-Allan Scientific Cat #8310-4). Images were taken on a Nikon microscope (Eclipse TE2000-U) using Metamorph image capture and analysis software (Version 6.3r5, Molecular Devices). Biomarker quantification was performed using QPath open-source digital image analysis software.

ARDS Cytokine analysis: To collect serum for cytokine analysis, blood was collected from the submandibular vein in living animals or from the ocular vein immediately after euthanasia of mice. Blood was allowed to clot for 30-60min at room temperature, then was centrifuged at 2000 x g for 10 minutes at 4°C. Serum was collected and stored at -80°C until use. Cytokine analysis was performed as described above for MHV cytokine analysis.

ARDS RNA analysis: To collect lung tissue for RNA analysis, animals were perfused with 5–10 ml of PBS to remove blood prior to excision of intact lungs. RNA was extracted from lungs using Trizol (15596026 Thermo Fisher). RT-PCR performed as described above for MHV RT-PCR.

ARDS CD11b⁺ cell isolation: Murine lung tissues were minced in a petri dish on ice and then enzymatically dissociated in Hanks Balanced Salt Solution with Ca²⁺ and Mg²⁺ containing 0.5 mg/ml Collagenase IV (Sigma), 0.1 mg/ml Hyaluronidase V (Sigma), 0.6 U/ml Dispase II (Roche), 0.005 MU/ml DNase I (Sigma) and 0.2 mg/ml soybean trypsin inhibitor (Worthington Biochemical) at 37°C for 15 min. Red blood cells were lysed with red blood cell lysis solution (Sigma), and the resulting suspension was filtered through a 70 µm cell strainer to produce a single cell suspension. Cells were centrifuged, at 300×g for 10 minutes, washed 2x in 1x PBS with 2mM EDTA and 0.5% BSA and resuspended in 90 µL of 1x PBS with 2mM EDTA and 0.5% BSA per 10⁷ total cells. CD11b⁺ cells were isolated by anti-CD11b magnetic bead pull down (130-049-601, Miltenyi Biotec) as follows: 10 µl of anti-CD11b MicroBeads was added per 10⁷ total cells, mixed well and incubated for 15 minutes in ice. Cells were then washed with 1–2 ml of 1x PBS with 2mM EDTA and 0.5% BSA per 10⁷ cells and centrifuged at 300×g for 10 minutes. The pellet was then resuspended at a concentration of 10⁸ cells in 500 µl of 1x PBS with 2mM EDTA and 0.5% BSA, applied to an LS column (Miltenyi Biotec, Cat #130-042-401) on a QuadroMACs magnetic separator (Miltenyi Biotec, Cat#130-091-051). The flow through containing CD11b⁻ cells was collected for RNA extraction, and CD11b⁺ cells were eluted using a wash buffer into a separate collection tube for RNA extraction. RNA was isolated from purified cells and RT-PCR performed as described above for MHV model RT-PCR.

ARDS vascular leak assay: To measure vascular leak in mouse models of acute respiratory distress syndrome, LPS or Poly I:C treated mice were injected by tail vein injection with 30mg/kg Evan's blue dye (100µl of 1% w/v in 0.9% saline) and one hour later, mice were euthanized. Lungs, heart, and kidneys were excised, weighed and dehydrated overnight at 65°C. Evan's Blue dye was extracted from dried tissue by incubation with formamide (221198, Sigma Aldrich) at a ratio of 10µl/mg dry weight overnight. Extracted dye was quantified versus a standard curve by measuring absorbance at 620nm.

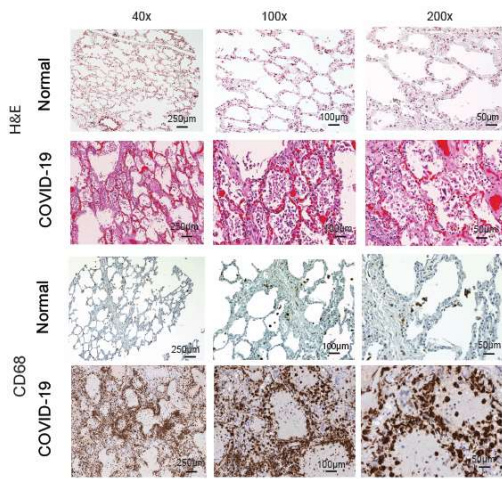
ARDS bronchoalveolar lavage: To collect cells and fluid from the bronchoalveolar spaces of mouse lungs, mice were euthanized. 1 ml of PBS-EDTA was injected into the lungs by intratracheal cannulation and then aspirated into a 15 ml conical tube. Two additional lavages were performed; cells from all three lavages were pooled, centrifuged for 5 min at 300×g at 4°C, resuspended in 1ml and centrifuged again using a Cytospin centrifuge (ThermoFisher) for morphological analysis by Wright Giemsa staining and counting.

Miles Assay In Vivo Vascular Leakage Assay

8-9 weeks old athymic nude mice (Jackson Laboratories) were treated with 100 µl vehicle or IPI-549 (15 mg/kg) by intraperitoneal injection. Two hours later, mice were intraperitoneally administered 40 µg pyrilamine maleate solution (P5514-25G, Sigma Aldrich) per gram of body weight. Mice were then administered 100 µl Evans Blue (1% w/v in 0.9% saline) by tail vein injection. Thirty minutes later, mice were injected intradermally with 50 µl of 1µg/µl of VEGF-A (450-32, PeproTech). Twenty minutes later mice were euthanized, and Evans Blue was extracted overnight from dried tissue by incubation with formamide (221198, Sigma Aldrich) at a ratio of 10 µl/mg dry weight. Extracted dye was quantified versus a standard curve by measuring absorbance at 620nm.

Western blotting to detect PI3K γ : Immortalized murine macrophages were transfected with ribonucleoprotein (RNP) complexes consisting of a one of two guide RNAs targeting the second exon of the *Pik3cg* gene (sgRNA 1: GCTGGAAGAACTATGAAC and sgRNA 2: GGAGA ACTATGAACAAC) and Cas9 nuclease (spCas9 2NLS Nuclease) from Synthego. Each population was Sanger sequenced to confirm gene knockdown. RIPA protein lysates from WT, transfected, and mock transfected macrophages were electrophoresed on a 4-12% gradient gel, transferred to PVDF membrane for sequential incubation in rabbit anti-PI3Kinase gamma (D55D5) or rabbit anti-GAPDH (14C10) at 1:1000 followed by incubation in anti-rabbit IgG, HRP-linked antibody and chemiluminescent substrate.

A



B

Lung tissue image cytometry cell classification

Lineage	Identification	Functional state	Marker
Broncholar epithelium	CD45 ⁻ KRT5 ⁺	Proliferation	Ki67
Type II alveolar cells	CD45 ⁻ KRT5 ⁻ SPB ⁺	Cytotoxicity	Granzyme B
Epithelium (other)	CD45 ⁻ KRT5 ⁺ SPB ⁻ PanCK ⁺	T cell memory	EOMES
"Other" nucleated cells	CD45 ⁻ KRT5 ⁻ SPB ⁻ PanCK ⁻	Immune regulatory	PD-1, PD-L1
Total CD4 ⁺ T lymphocytes	CD45 ⁺ CD3 ⁺ CD8 ⁻		
Regulatory T cells (Treg)	CD45 ⁺ CD3 ⁺ CD8 ⁻ Foxp3 ⁺		
Th1 helper T cells	CD45 ⁺ CD3 ⁺ CD8 ⁻ Foxp3 ⁻ Tbet ⁺		
Th other	CD45 ⁺ CD3 ⁺ CD8 ⁻ Foxp3 ⁻ Tbet ⁻		
CD8 ⁺ T lymphocytes	CD45 ⁺ CD3 ⁺ CD8 ⁺		
CD20 ⁺ B cells	CD45 ⁺ CD3 ⁻ CD20 ⁺		
Neutrophils and eosinophils	CD45 ⁺ CD3 ⁻ CD20 ⁻ CD66b ⁺		
Macrophages	CD45 ⁺ CD3 ⁻ CD20 ⁻ CD66b ⁻ CD68 ⁺ CCR2 ⁻ CD163 ⁺		
Monocytes	CD45 ⁺ CD3 ⁻ CD20 ⁻ CD66b ⁻ CD68 ⁺ CCR2 ⁺ CD163 ⁻		
Immature DC	CD45 ⁺ CD3 ⁻ CD20 ⁻ CD66b ⁻ CD68 ⁺ HLA class II ⁺ CD11c ⁻ DC-LAMP ⁻		
Mature DC	CD45 ⁺ CD3 ⁻ CD20 ⁻ CD66b ⁻ CD68 ⁺ HLA class II ⁺ CD11c ⁺ DC-LAMP ⁺		
"Other" myeloid cells	CD45 ⁺ CD3 ⁻ CD20 ⁻ CD66b ⁻ CD68 ⁺ HLA class II ⁺ CD11b ⁻		
"Other" immune cells	CD45 ⁺ CD3 ⁻ CD20 ⁻ CD66b ⁻ CD68 ⁺ HLA class II ⁻ CD11b ⁻		

C

BAL image cytometry cell classification

Lineage	Identification	Functional state	Marker
Total CD3 ⁺ T lymphocytes	CD45 ⁺ CD3 ⁺	Immune regulatory	PD-1, PD-L1
Neutrophils and eosinophils	CD45 ⁺ CD3 ⁻ CD66b ⁺		
Macrophages	CD45 ⁺ CD3 ⁻ CD66b ⁻ CD68 ⁺ CCR2 ⁻ CD163 ⁺		
Monocytes	CD45 ⁺ CD3 ⁻ CD66b ⁻ CD68 ⁺ CCR2 ⁺ CD163 ⁻		
Total DCs	CD45 ⁺ CD3 ⁻ CD66b ⁻ CD68 ⁺ HLA class II ⁺ CD11c ⁻		
"Other" myeloid cells	CD45 ⁺ CD3 ⁻ CD66b ⁻ CD68 ⁺ HLA class II ⁺ CD11b ⁻		
"Other" immune cells	CD45 ⁺ CD3 ⁻ CD66b ⁻ CD68 ⁺ HLA class II ⁻ CD11b ⁻		

D

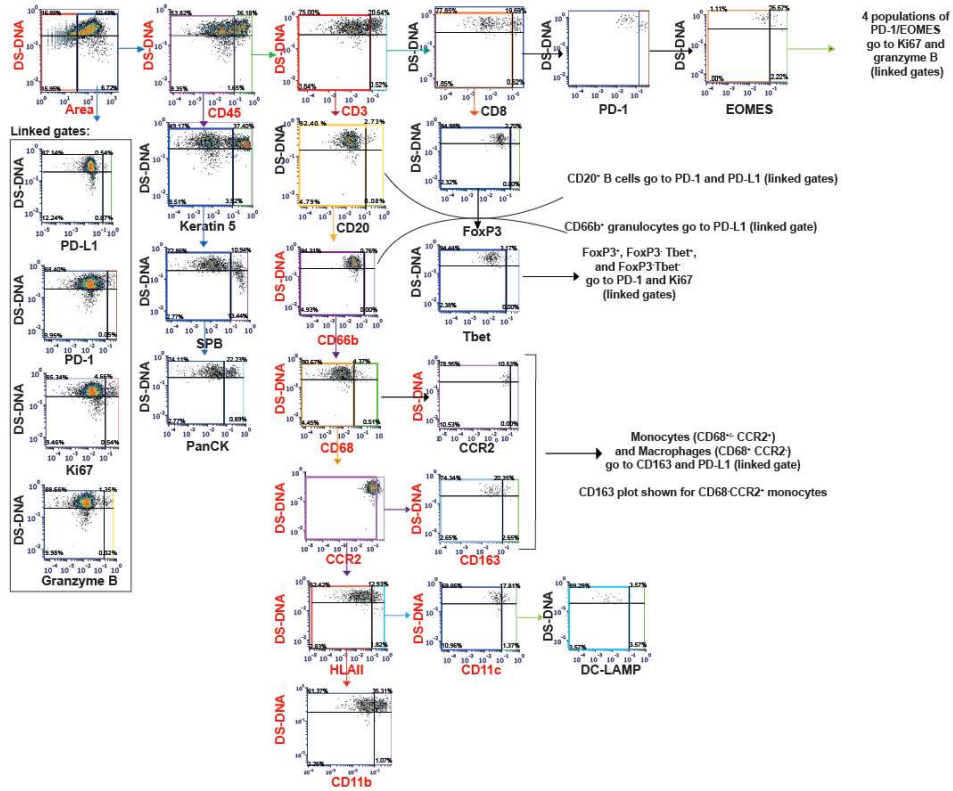


Figure S1: Immunohistochemistry and flow cytometry gating for BAL and lung specimens from COVID-19-infected and uninfected patients. (A) Serial images of H&E and anti-CD68 stained fields at 40, 100 and 200X in lung tissue from uninfected (normal) and COVID-19 patients. Scale bars indicate 250, 100 or 50 μm . (B) Cell type classification by hierarchical gating in lung specimens. (C) Cell type classification by hierarchical gating in BAL specimens. (D) Image cytometry gating schema; colored arrows indicate movement of a like colored parent population into a subsequent plot for further gating. Linked gates are gated on all total cells but applied within the gating schema on various cell populations (where indicated). DS-DNA quantification was included for reference. Gate axes highlighted with red text were utilized to gate BAL samples, which were stained with only a subset of antibodies focused on myeloid cell types.

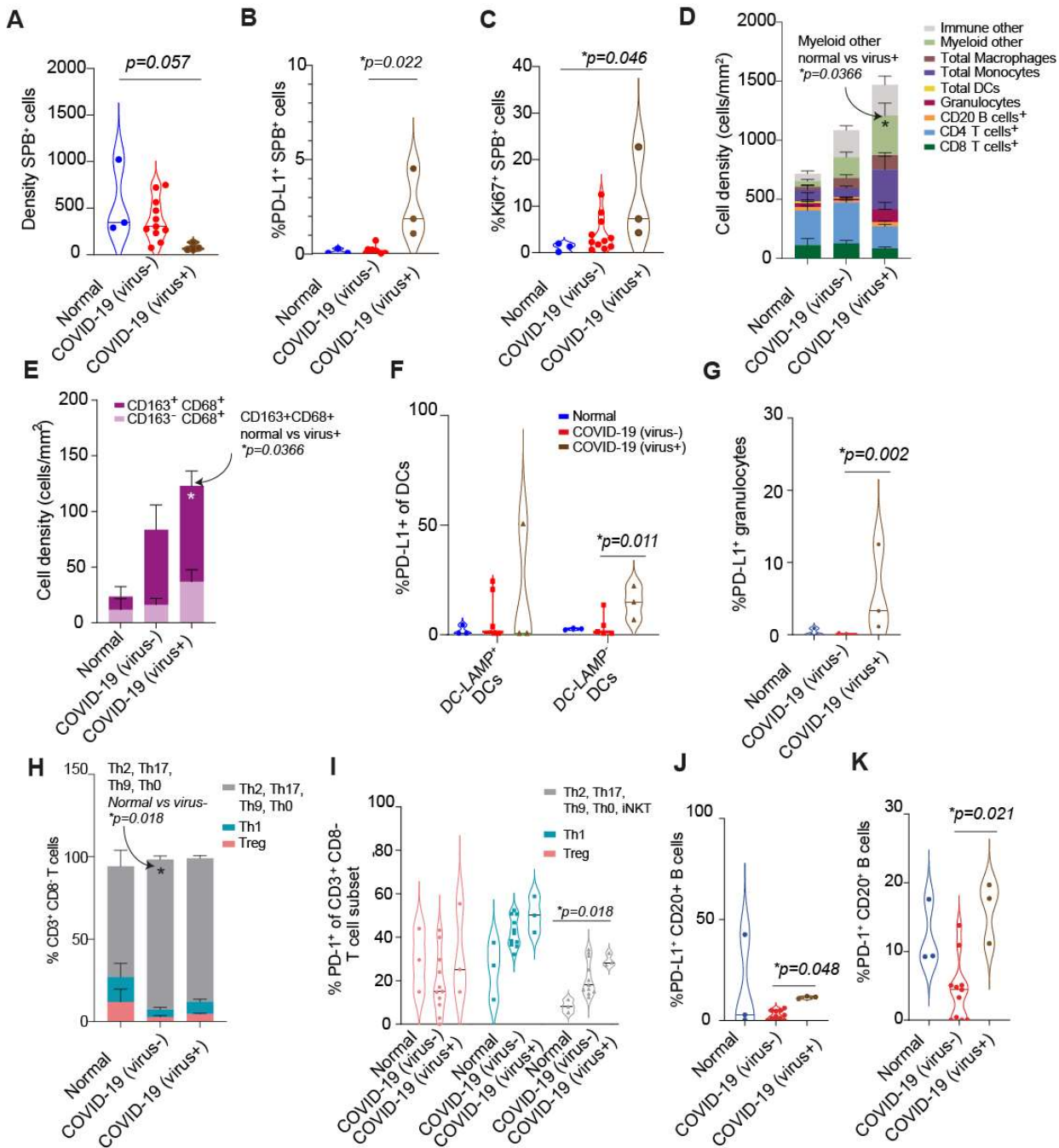


Figure S2: Characteristics of cell populations in lung specimens from virus-positive and virus-negative COVID-19 and normal patients. (A) Density of surfactant protein B positive (SPB⁺) cells in virus+ lungs as compared to normal. (B) Percent of PD-L1⁺SPB⁺ cells in lung tissue from normal, virus+ and virus- COVID-19 patients. (C) Percent of Ki67⁺SPB⁺ cells in lung tissue from normal, virus+ and virus- COVID-19 patients. (D) Average immune composition in virus- and virus+ lung tissue. (E) Average abundance of CD163[±] macrophages in virus+ and virus- tissues. (F) PD-L1 expression on immature and mature DCs comparing virus+ compared to virus-groups. (G) PD-L1 expression on granulocytes in virus+ and virus- patients. (H) Percent Th2, Th17, Th9, and Th0 cells within CD3⁺CD8⁻ subsets. (I) Percent of PD-1⁺CD3⁺CD8⁻ T cell subsets. (J) Percent PD-L1⁺ CD20⁺ B cells and (K) PD-1⁺ CD20⁺ B cells in virus+ and virus- tissues. For violin plots, dashed lines indicate mean and interquartile range; for stacked bar graphs, bars indicate mean ± SEM. Statistical testing was performed with Mann Whitney non-parametric T tests.

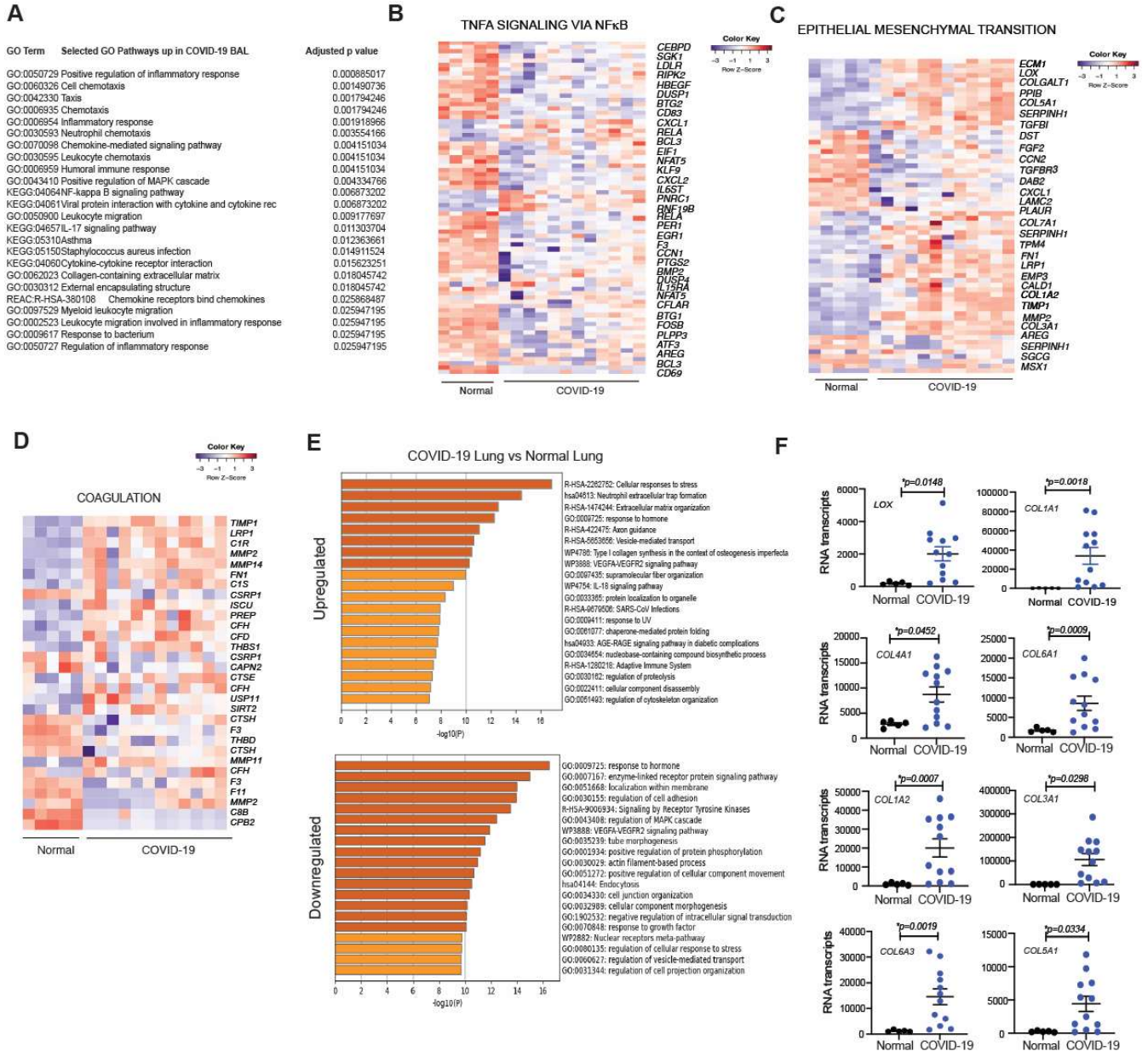


Figure S3: RNA sequencing analysis of COVID-19 lung versus normal lung. (A) Differentially upregulated GO pathways in BAL of recently hospitalized COVID-19 vs normal patients (B to D) Heatmaps depicting differentially expressed genes in COVID-19 versus normal patient tissue corresponding to GSEA Hallmark pathways: TNFA signaling through NFκB (B), epithelial to mesenchymal transition (C) and coagulation (D). (E) Differentially expressed GO pathways in COVID-19 vs normal lungs. (F) Graphs of *LOX* and collagen isoform mRNA expression (read counts) in lungs from COVID-19 versus normal patients. Statistical testing was performed by limma-vroom analysis.

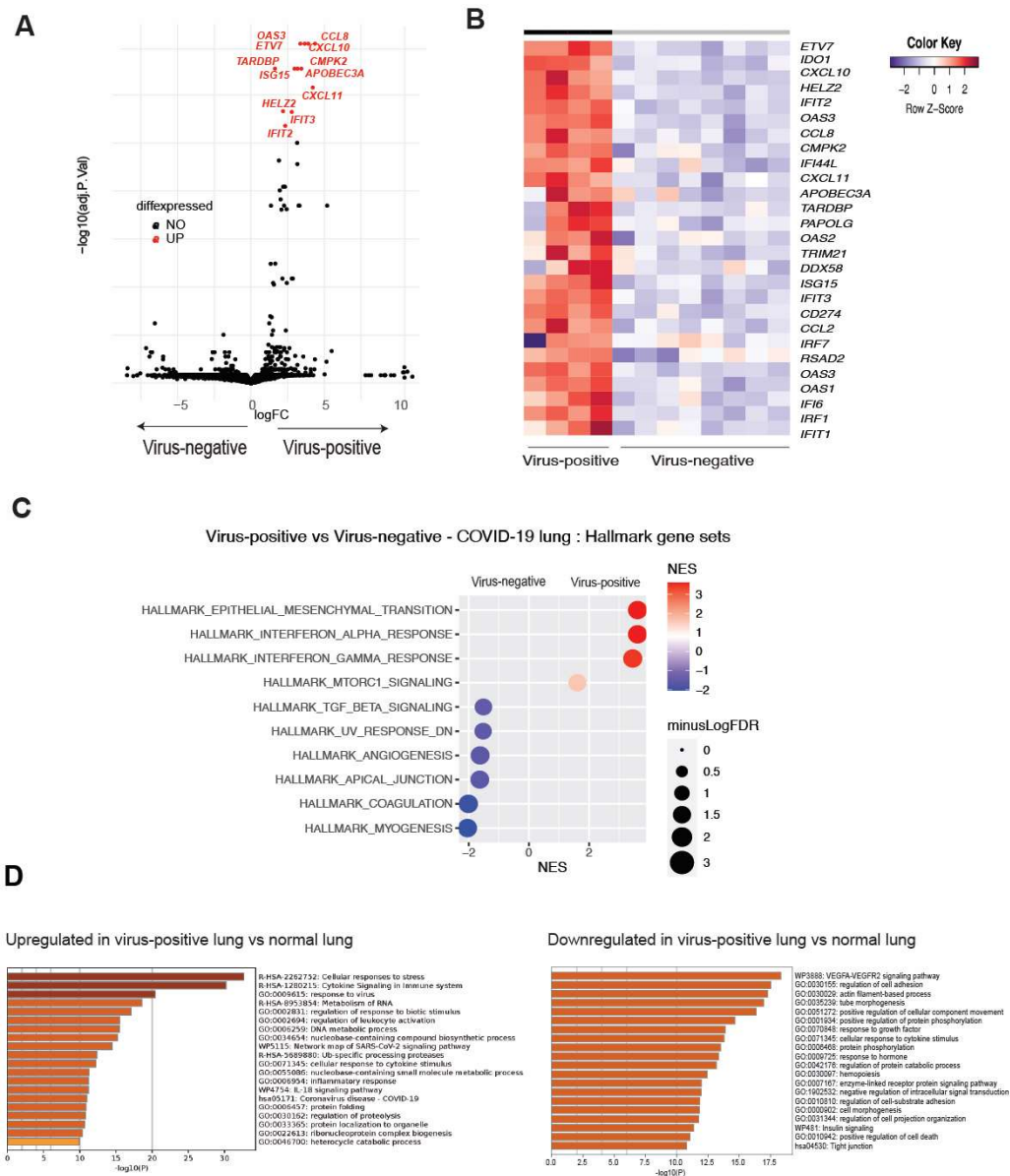


Figure S4: RNA sequencing analysis of virus-positive versus virus-negative COVID-19 lung. (A) Volcano plot of differentially expressed genes expressed in virus-positive vs virus-negative COVID-19 patient lung tissue. (B) Heatmap of differentially expressed genes in lung tissue of COVID-19 patients who were virus-positive versus virus-negative at the time of death. (C) Top GSEA Hallmark pathways that are up- or down-regulated in virus-positive COVID-19 patient lung tissue characterized by GSEA normalized expression score (NES) and False Discovery Rate (FDR). (D) GO pathways significantly upregulated or downregulated in COVID-19 virus positive lung versus normal lung. Statistical testing was performed by limma-vroom analysis.

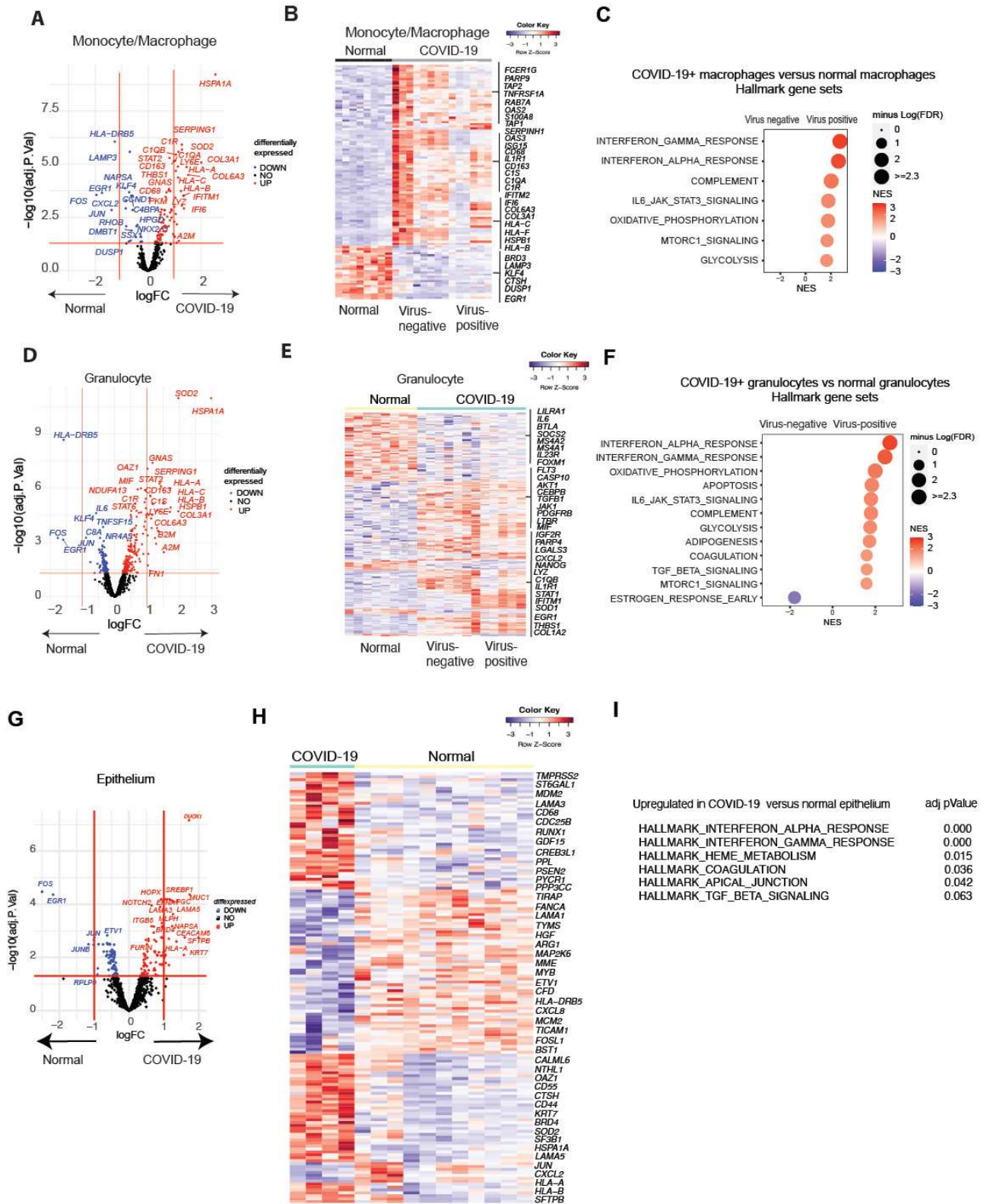


Figure S5: Spatial transcriptomics analysis of COVID-19 lungs. (A to H) Volcano plots (A, D, G) and heat maps (B, F, H) of differential gene expression within macrophages (A and B), granulocytes (D and E), and epithelium (G and H) from 4-8 regions of tissue identified by spatial transcriptomics using immune oncology and COVID-19 RNA probes in anti-CD68, anti-myeloperoxidase, and anti-pan-cytokeratin immunostained normal (n=1) and COVID-19 (n=2) patient lung tissues. (C, F, I) Tables of GSEA Hallmark pathways that are up- or down-regulated in macrophages (C), granulocytes (F), and epithelium (I) from COVID-19 versus normal lung tissue. Statistical testing was performed by limma-vroom analysis.

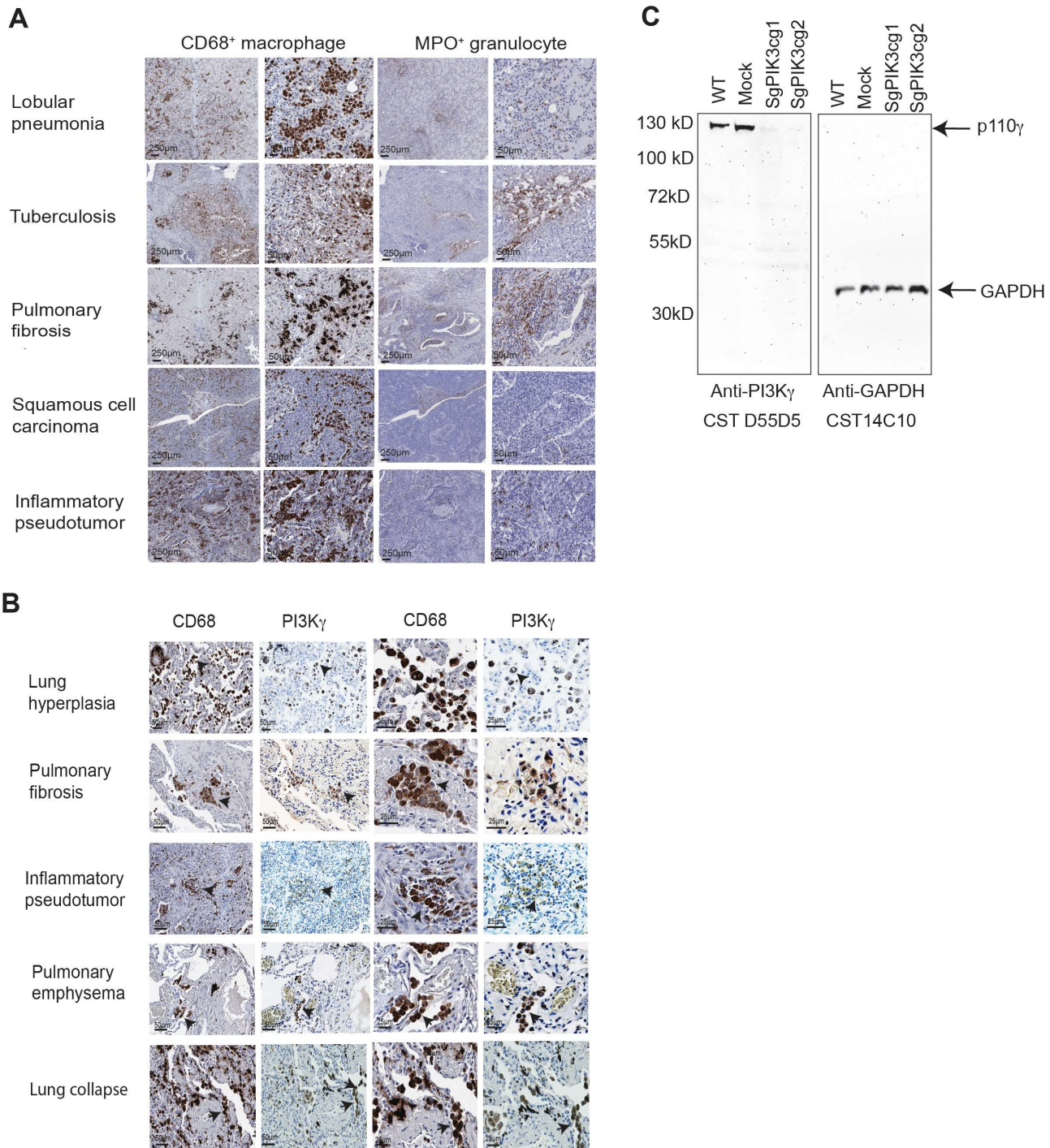


Figure S6: Lung inflammation is characterized by PI3K γ expression. (A) Serial images of anti-CD68 and anti-MPO stained lung tissues from patients with inflammatory lung diseases, including lobular pneumonia, tuberculosis, pulmonary fibrosis, squamous cell carcinoma and inflammatory pseudotumor. Scale bars indicate 250 μ m or 50 μ m. (B) Serial images of anti-CD68 and anti-PI3K γ stained lung tissues from patients with inflammatory lung diseases, including lung hyperplasia, pulmonary fibrosis, inflammatory pseudotumor, pulmonary emphysema, and lung collapse. Scale bars indicate 50 μ m. (C) Western blot detecting PI3K γ protein using antibody D55D5 and detecting GAPDH using antibody CST14C10 in lysates from WT, Mock transfected, and *Pik3cg* sgRNA transfected murine macrophages.

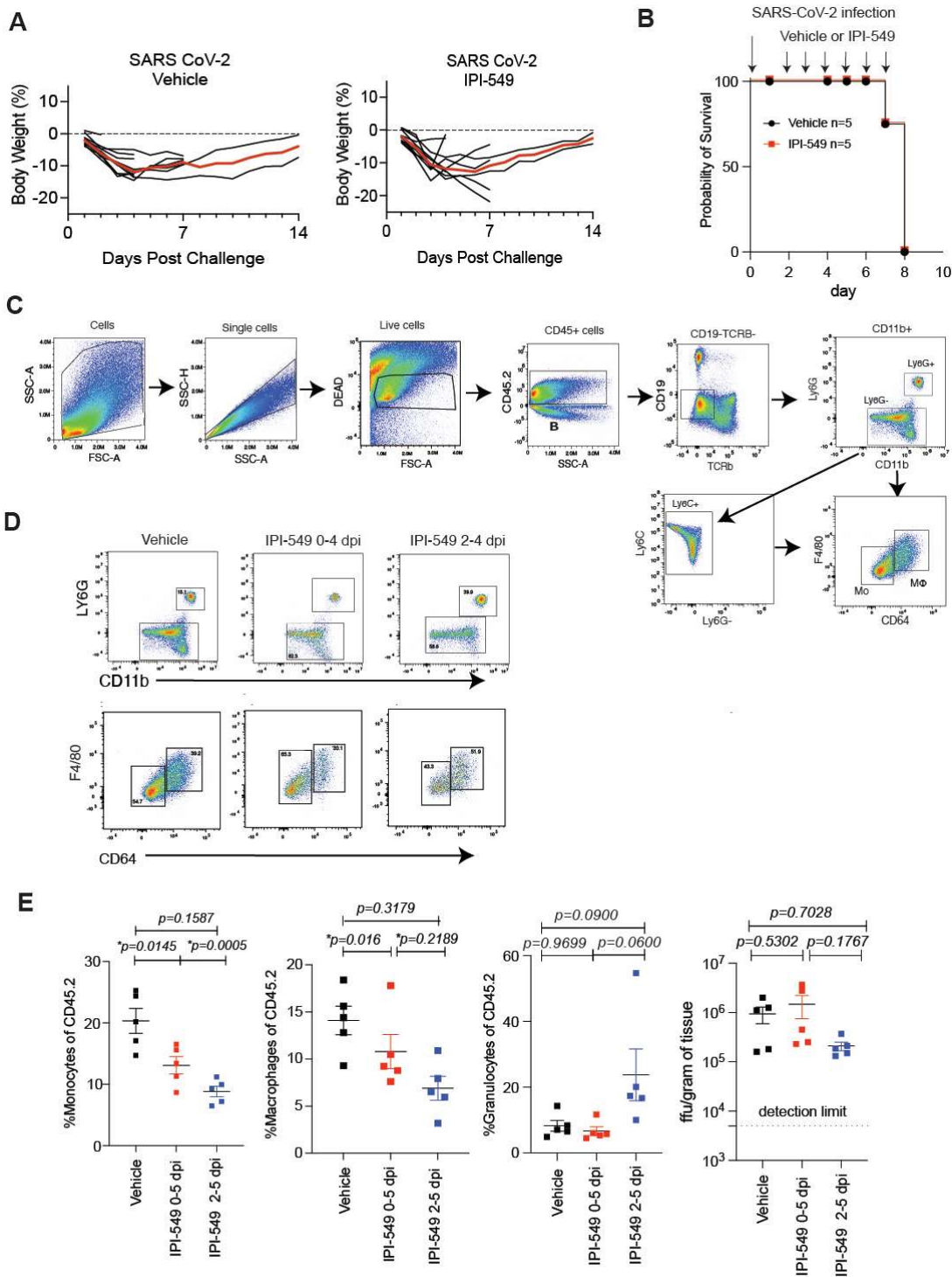


Figure S7: PI3K γ inhibition suppresses lung inflammation. (A) Graphs of Individual (black line) and mean (red line) percent body weight changes over time in SARS-CoV-2 infected hamsters that were treated with vehicle or IPI-549. (B) Graphs of survival of hACE2 transgenic mice infected with SARS-CoV-2 and treated with vehicle or IPI-549 from 2 dpi. (C) Flow cytometry gating scheme for analysis of immune cell infiltrates in SARS-CoV-2 infected lungs from mice treated with vehicle or IPI549 from d0-4 or d2-4. (D) Representative flow cytometry plots of Ly6G⁺ granulocytes (CD11b⁺Ly6G⁺) and Ly6G⁻Ly6C⁺ monocytes and macrophages from SARS-CoV-2 infected lungs from hACE2-TG mice treated with vehicle or IPI549 from d0-4 or d2-4. (E) Graphs of mean \pm SEM percent monocytes, granulocytes and macrophages per CD45% cells, and viral load (ffu/gram tissue) in mice from (C) (n=5). Significance in (E) was determined by one-way ANOVA with Tukey's post hoc test.

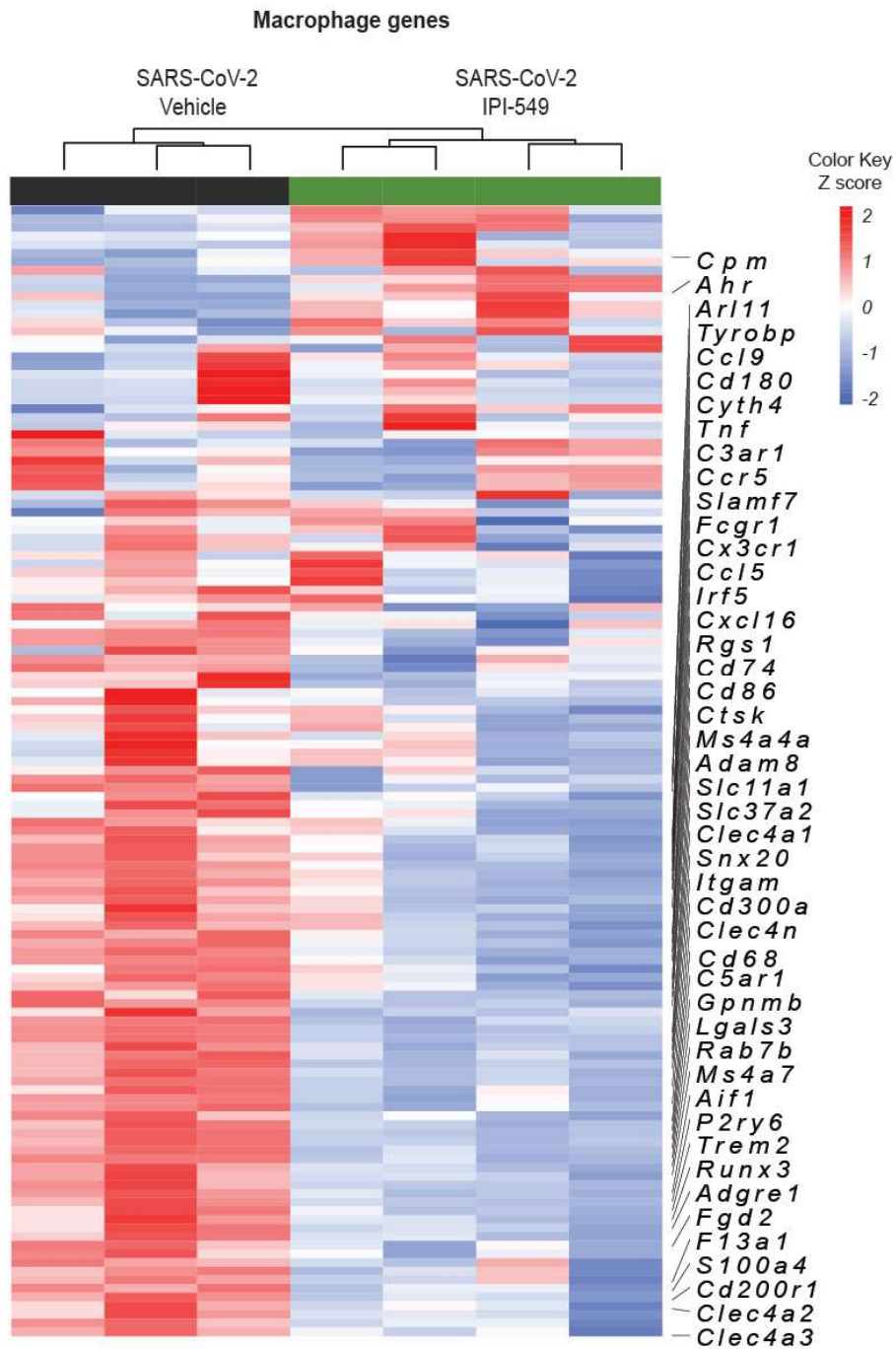


Figure S8: Heatmap of macrophage gene expression in vehicle- and IPI-549-treated, SARS-CoV-2 infected mouse lungs. Heatmap of canonical macrophage genes differentially expressed in SARS-CoV-2 infected vehicle treated vs IPI-549 treated mouse lung. Statistical testing was performed by limma-vroom analysis.

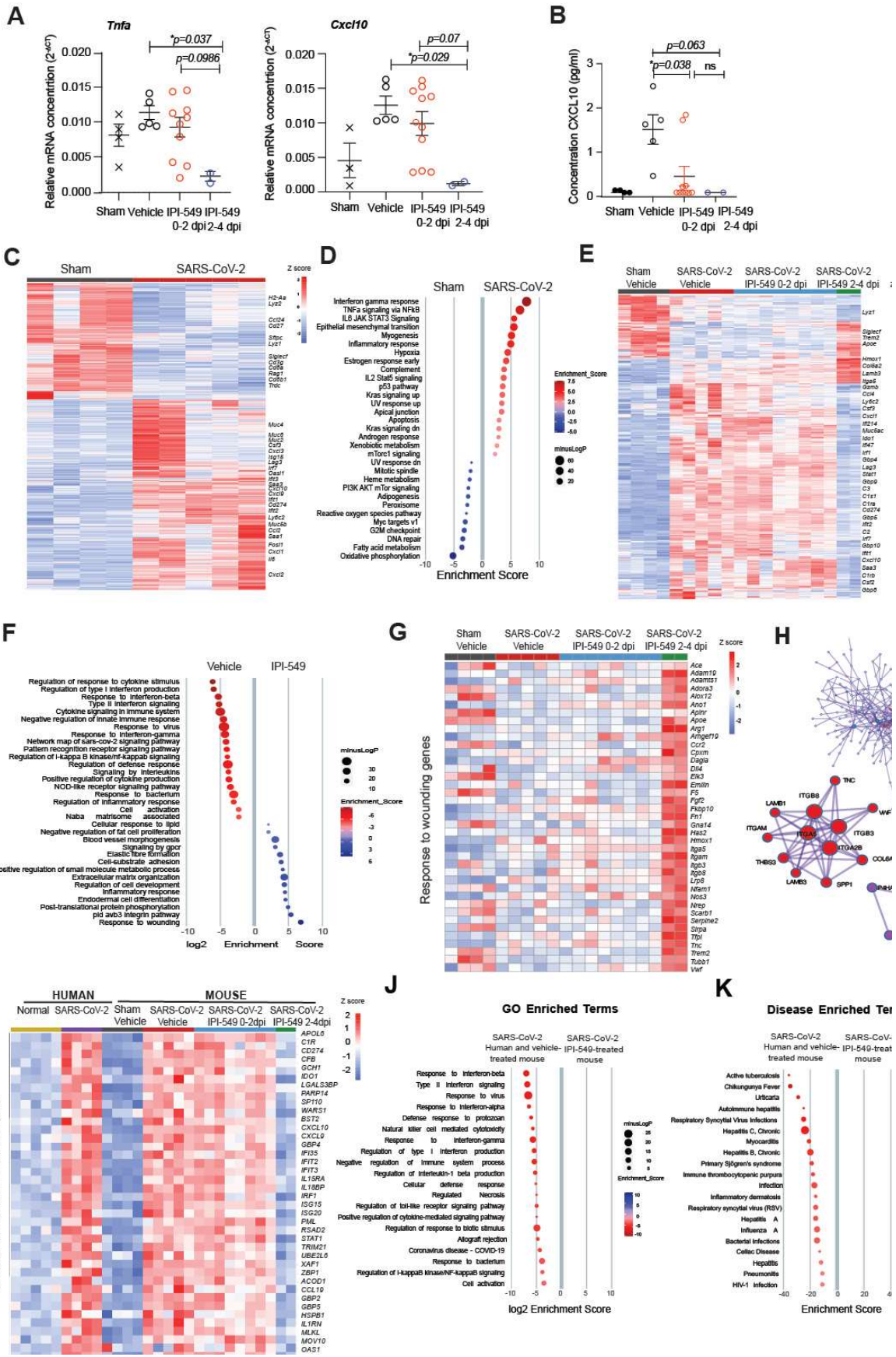


Figure S9: Transcriptomics reveal that PI3K γ inhibition suppresses inflammation and promotes lung tissue repair during maSARS-CoV-2 infection. (A) Graph of mean \pm SEM mRNA expression ($2^{-\Delta\text{CT}}$) of *Tnfa* and *Cxcl10* mRNA in lung tissue from animals from maSARS-CoV-2 infected animals treated with IPI-549 or vehicle. (B) Graph of mean concentration \pm SEM CXCL10 in sera of animals from A. (C) Heatmap of significantly differentially expressed genes in Sham (control) and SARS-CoV-2 infected mouse lung. Select gene names are shown. (D) Plot of gene enrichment signatures up and down-regulated in SARS-CoV-2 infected mouse lung. (E) Heatmap of significantly differentially expressed genes in Sham (Vehicle) and SARS-CoV-2 infected mouse lung treated with vehicle or with IPI-549 from 0-2 dpi (cohort 1) or 2-4 dpi (cohort 3). (F) Plot of gene enrichment signatures that are up or down or regulated by IPI-549 treatment versus vehicle in SARS-CoV-2 infected mouse lung. (G) Heatmap of Gene Ontology tissue repair pathway genes that are upregulated in SARS-CoV-2 infected mouse lungs treated with IPI-549. (H) Cytoscape gene interaction network analysis of upregulated wound healing genes from A. (I) Heatmap of significantly differentially expressed genes upregulated in IPI-549 treated lungs versus SARS-CoV-2 infected human and mouse lung tissues. (J) Plot of gene enrichment signatures common to mouse and human SARS-CoV-2 infected lungs down-regulated in IPI-549 treated lungs. (K) Plot of Disease Gene Net signatures downregulated in IPI-549-treated lungs. Statistical testing was performed by limma-vroom analysis.

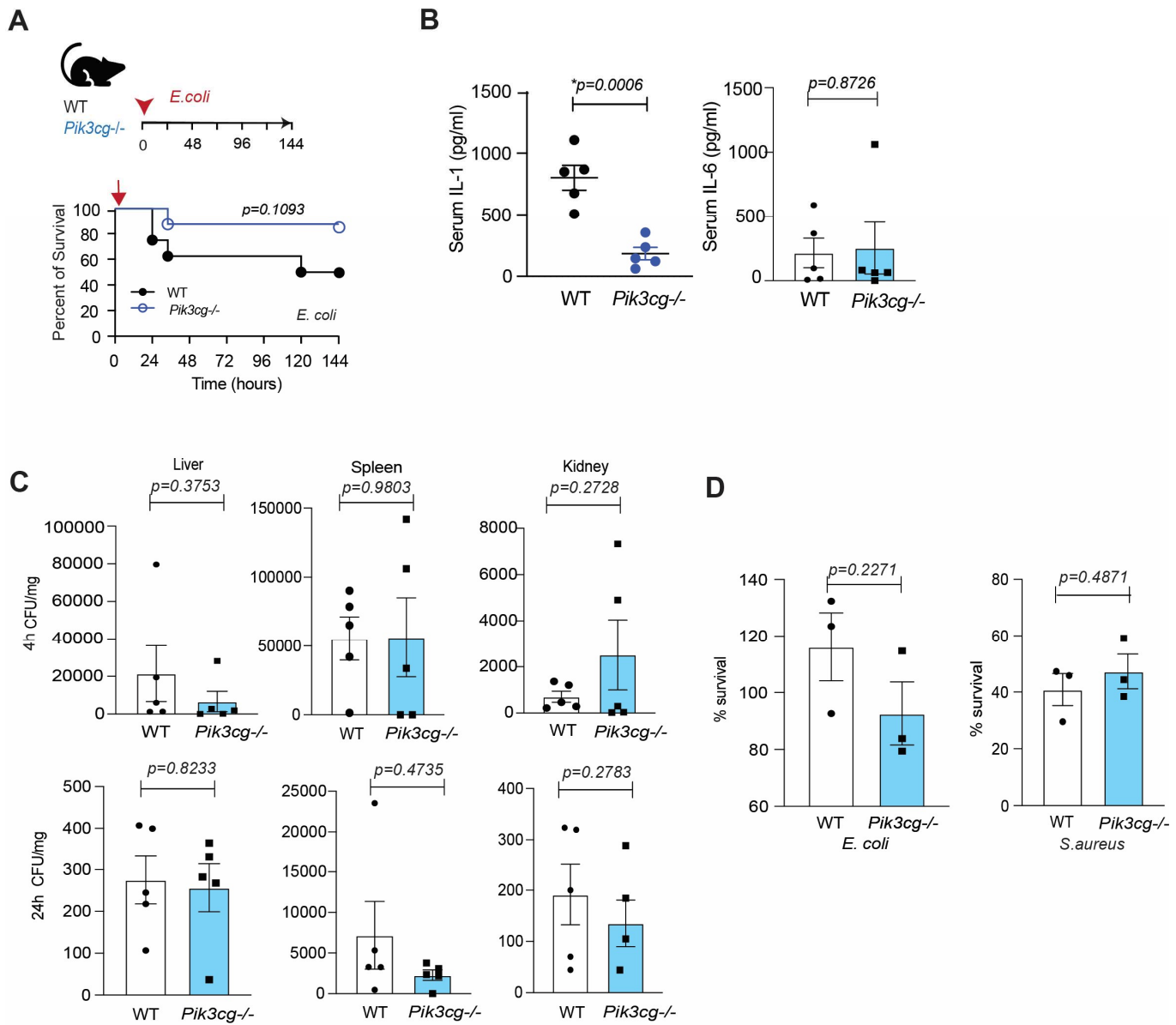


Figure S10: PI3K γ function in animal models of bacterial infection. (A) Kaplan-Meier plots of survival over 144 h of WT and *Pik3cg*^{-/-} mice (n=8) inoculated with multi-drug resistant *Escherichia coli*. Significance determined by Log-rank Mantel-Cox test. (B) Graph of concentration of IL-1 β (n=5) and IL-6 (n=5) in serum from MRSA infected WT and *Pik3cg*^{-/-} mice. (C) Graph of survival of bacteria in vivo in WT and *Pik3cg*^{-/-} mice at 4h and 24h in liver, spleen and kidney determined by ex vivo colony forming assay. (D) Graph of survival of bacteria in culture with WT and *Pik3cg*^{-/-} bone marrow derived macrophages as a measure of phagocytosis by macrophages (n=3). Statistical significance was determined by t test for (B to D).

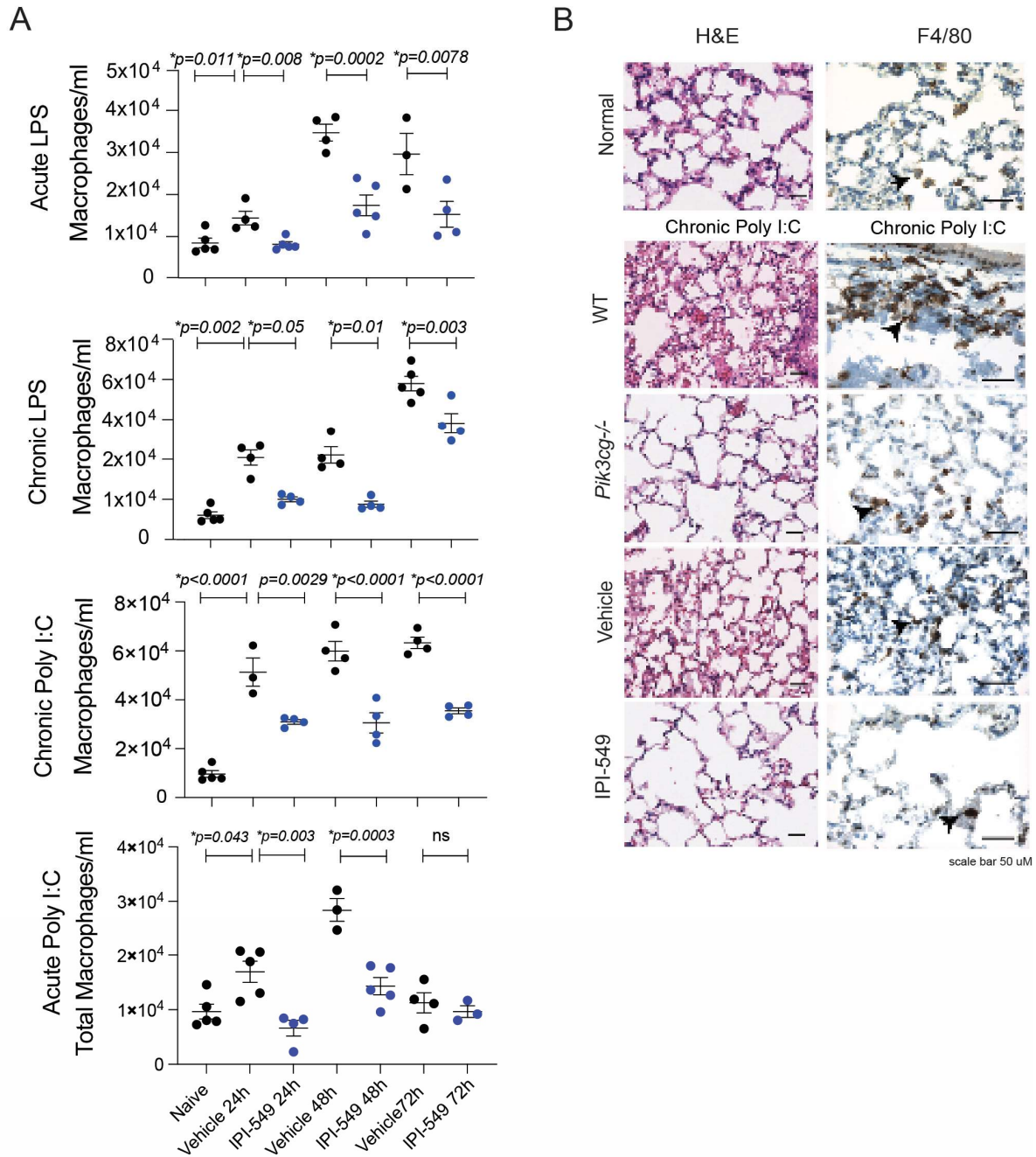


Figure S11: PI3K γ function in animal models of ARDS. (A) Graph of quantification of macrophage density in BAL from acute LPS, chronic LPS, and poly I:C stimulated animals treated with vehicle or IPI-549 (n=5) measured at 24, 48 or 72h post stimulation. Statistical significance determined by one-way ANOVA with Tukey's post-hoc test. (B) Representative images of H&E and anti-F4/80-stained lung tissue from naïve mice and acute LPS and chronic poly I:C treated mice. Scale bar indicates 50 μ m. Arrowheads indicate F4/80⁺ macrophages.

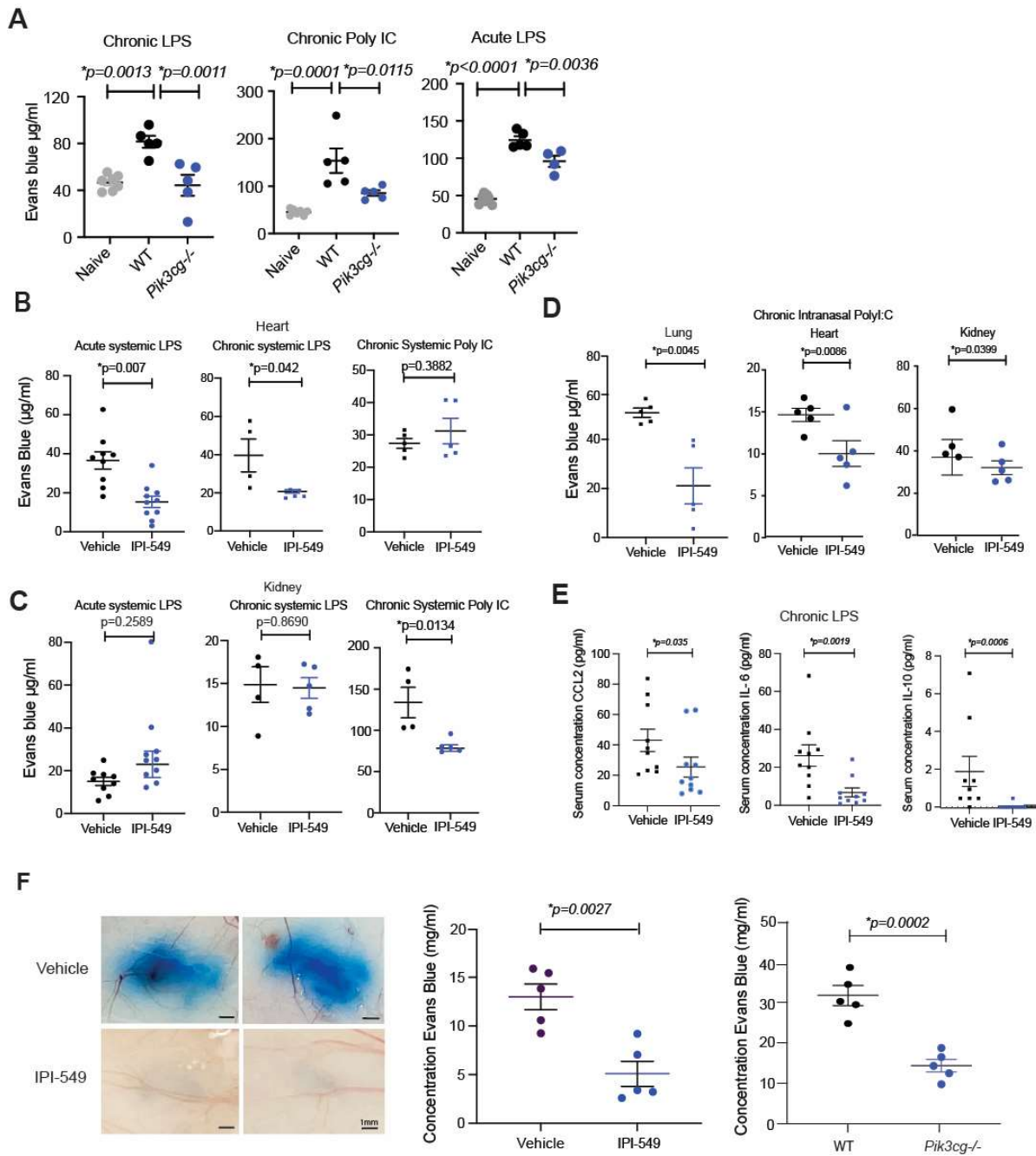


Figure S12: PI3K γ inhibition suppresses vascular leak in models of inflammation. (A) Graph of quantification of vascular leak (mean \pm SEM) in naïve ($n=7$) mice and in acute LPS, chronic LPS or chronic Poly I:C stimulated WT ($n=5$) versus *Pik3cg*^{-/-} ($n=5$) mice. Statistical significance was determined by one-way ANOVA with Tukey's post-hoc test. (B and C) Graph of quantification of vascular leak in heart (B) and kidney (C) of mice exposed to acute systemic LPS, chronic systemic LPS, or chronic systemic Poly I:C stimulated and treated with vehicle ($n=5$) or IPI-549 ($n=5$). Significance testing determined by Student's t-test. (D) Graph of quantification of vascular leak in heart, kidney, and lungs of animals treated chronically with intranasal Poly I:C administration and either vehicle ($n=5$) or IPI-549 ($n=5$). Statistical significance determined by t test. (E) Graph of quantification of CCL2, IL-6, and IL-10 in serum from WT versus *Pik3cg*^{-/-} and vehicle versus IPI-549-treated mice chronically stimulated with LPS ($n=5$). Statistical significance determined by Mann Whitney test. (F) Representative images and graph of quantification of VEGF-A mediated vascular leak (mean \pm SEM) in WT ($n=5$) versus *Pik3cg*^{-/-} ($n=5$) and in vehicle- ($n=5$) versus IPI-549-treated mice ($n=5$). Statistical significance determined by t test.

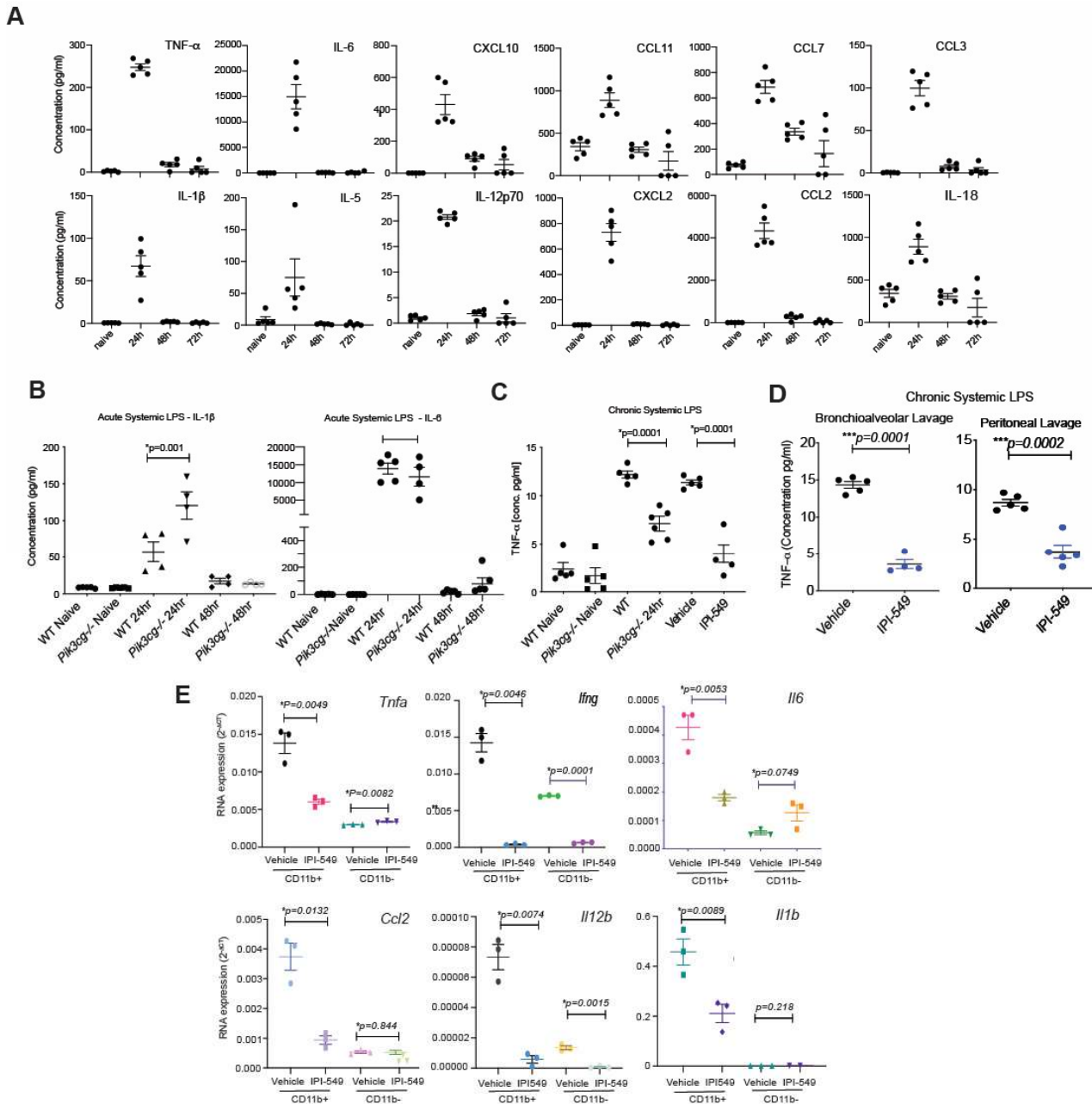


Figure S13: Effect of PI3K γ inhibition on circulating cytokines in models of ARDS. (A) Graph of concentration of cytokines and chemokines in serum from naïve mice and acute systemic LPS-stimulated WT mice at 0h (Naïve), 24h, 48h and 72h post-stimulation (mean \pm SEM, n=5). (B) Graph of concentration of IL-6 and IL-1 β in serum from naïve mice and acute systemic LPS-stimulated WT or PI3K γ ^{-/-} mice at 0h (Naïve), 24h and 48h post-stimulation (mean \pm SEM, n=5). Statistical significance was determined by t-test. (C) Graph of concentration of TNF- α in serum from naïve mice, from chronic LPS-stimulated WT or PI3K γ ^{-/-} mice, and from chronic LPS-stimulated vehicle or IPI-549-treated mice (mean \pm SEM, n=5). Statistical significance was determined by t-test. (D) Graph of concentration of TNF- α in BALF and peritoneal lavage fluid (PLF) from naïve mice, from acute LPS-stimulated WT or PI3K γ ^{-/-} mice, and from acute LPS-stimulated vehicle or IPI-549-treated mice (mean \pm SEM, n=5). Statistical significance was determined by t-test. (E) Graph of mean \pm SEM mRNA expression ($2^{-\Delta CT}$) of cytokines in CD11b⁺ and CD11b⁻ cells isolated from lungs of chronic LPS stimulated animals treated with vehicle or IPI-549 (n=3). Statistical significance was determined by t-test.

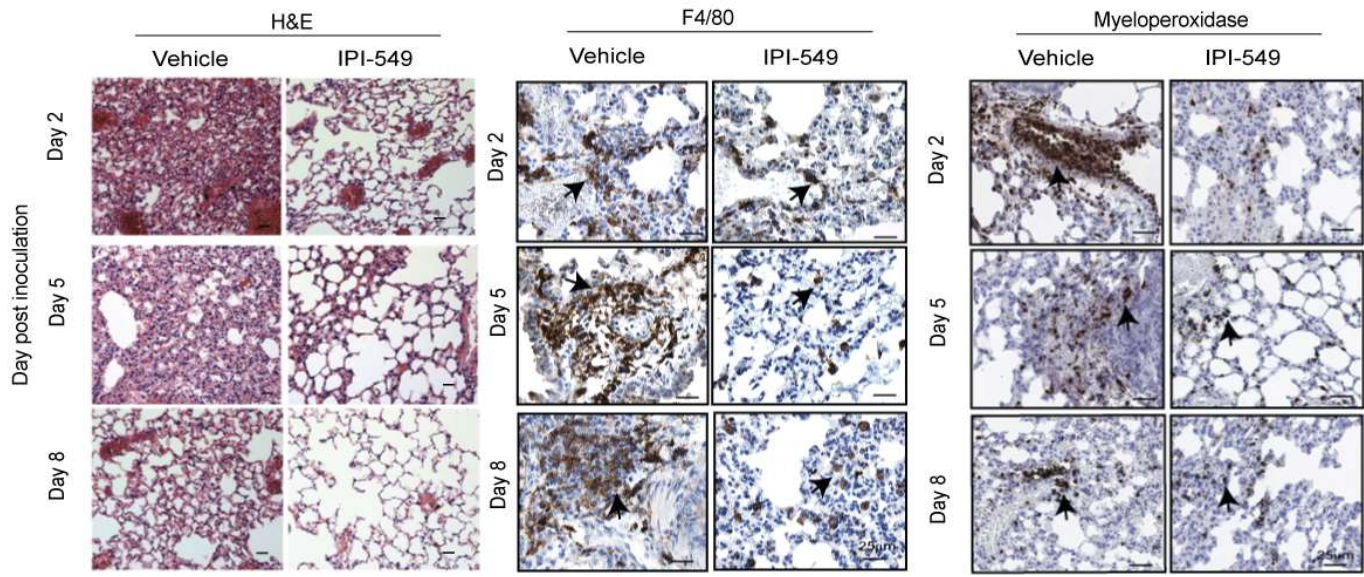


Figure S14: PI3K γ inhibition reduces inflammation from MHV infection. Representative images of H&E, anti-F4/80⁺ and anti-Myeloperoxidase (MPO)-stained lung tissues from MHV infected mice 0-, 5-, or 8-days post-inoculation. Arrowheads indicate F4/80⁺ macrophages and MPO⁺ granulocytes.

Table S1: Patient characteristics. Age, gender, co-morbidity details, and virus positivity when available, of patients with COVID-19 from whom BAL tissue was collected.

COVID-19 BAL	Age (years)	Gender	Days from admit to death	Days from admit to BAL	Acute inflammation	Co-morbidity	Cytological diagnosis	Clinical history	COVID +19 BAL
C1	53	M	40	28	no	Hypertension	Fungi; Candida	Sepsis; ECMO; ventilation	
C2	55	M	48	27	yes	Hypertension	Acute inflammation; Fungi	Respiratory failure; ECMO; ventilation	
C3	53	M	Discharged	35	yes	Asthma, Hypertension	Acute inflammation; Fungi	COVID 19; ARDS	
C4	47	M	27	18	yes	Diabetes	Acute inflammation, MRSA	Septic shock	
C5	50	F	Discharged	21	yes	None	Acute inflammation; Fungi		
C6	67	M	12	8	yes	Heart failure, Diabetes	Acute inflammation; Fungi; Candida		Yes
C7	49	M	51	18	yes	None	Acute inflammation	Hypertension; Diabetes	
C8	48	M	Discharged	7	yes	Diabetes, Coronary Artery Disease	Acute inflammation	Hypertension, heart failure; COVID 19; pneumonia	Yes

Table S2: Patient characteristics. Age, gender, co-morbidity details, and virus positivity when available, of normal uninfected patients from whom BAL tissue was collected.

Normal BAL	Age (years)	Gender	Days from admit to death	Days from admit to BAL	Acute inflammation
NB1	81	F	n/a	n/a	no
NB2	48	M	n/a	n/a	no
NB3	77	M	n/a	n/a	no
NB4	65	F	n/a	n/a	no
NB5	56	M	n/a	n/a	no

Table S3: Patient characteristics. Age, gender, co-morbidity details, and virus positivity when available, of COVID-19 patients from whom lung tissue was collected.

COVID-19 Lung	AGE	GENDER	TIME TO DEATH	COVID status	HEALTH HISTORY	ETHNICITY
C1	88	F	unknown		Pneumonia; ARDS; Respiratory Failure	
C4	90	F	3 days	Virus-positive (RNA seq)	Alzheimer's/ Parkinson's; oxygen; vancomycin	Japanese
C2	67	M	unknown		Pleural effusion, Pulmonary edema, diffuse alveolar damage	
C13 (UL) C14 (LL)	44	F	6 days	Virus-positive (RNA seq)	Obesity; COVID-19 pneumonia; ARDS, Intubated; ECMO 5 days ; acute kidney infection, renal failure	
C7	65	M	35 days		Hypertension, COPD and multiple myeloma on Revlimid; COVID-19, ARDS; Intubated 23 days; renal failure, septic shock, organ failure	
C8	88	F	17 days		Hypertension, deep vein thrombosis; Intubated 15 days; Pneumonia; ARDS; Remdesivir 2 days	Hispanic
C6	65	M	35 days		Metastatic multiple myeloma, asthma	Caucasian
C3	57	M	28 days		Diabetes, hypertension; renal failure; ECMO; Respiratory failure, renal failure	Hispanic
C11 (UL),C12 (LL)	80	F	7 days	Virus-positive (RNA seq)	Multiple myeloma; COVID-19 pneumonia; Oxygen comfort care	
C5	65	M	28 days		Diabetes, asthma; ventilation; septic shock, multi-organ failure	Hispanic
C9	unknown	unknown	unknown		unknown	
C10	unknown	unknown	unknown		unknown	

Table S4: Patient characteristics. Age, gender, ethnicity, health status, and virus positivity when available, of normal patients from whom lung tissue was collected.

NORMAL LUNG	AGE	GENDER	TIME TO DEATH	COVID status	HEALTH STATUS	ETHNICITY
N1	73	F	n/a	n/a	Adjacent normal to adenocarcinoma, micropapillary predominant	unknown
N2	59	F	n/a	n/a	Adjacent normal to adenocarcinoma	unknown
N3	70	M	n/a	n/a	unknown	unknown
N4	72	F	n/a	n/a	Adjacent normal to Invasive adenocarcinoma, acinar predominant	unknown
N5	46	F	n/a	n/a	Adjacent normal to adenocarcinoma, enteric type	unknown

